Final Report

HYDRODYNAMIC MODELING OF MISSISQUOI BAY IN LAKE CHAMPLAIN

Submitted to:

Vermont Geological Survey
Vermont Agency of Natural Resources
103 South Main St., Center Building
Waterbury, VT 05671

Submitted by:

Daniel Mendelsohn
Craig Swanson
Tatsusaburo Isaji
Applied Science Associates, Inc.
70 Dean Knauss Drive
Narragansett, RI 02882

ASA Project 95-136
March 27, 1997

TABLE OF CONTENTS

Page

LIST OF FIGURES

LIST OF TABLES

EXECUTIVE SUMMARY

Missisquoi Bay is a small embayment located in the northeast quadrant of Lake Champlain with three major tributaries, the Missisquoi, Pike and Rock Rivers. The Swanton-Alburg Route 78 bridge is located at the southern end (mouth) of the bay and consists of two causeway sections extending from each shore and a bridge section between. Residents have noted that the bay has deteriorated over time and believe that the causeways at the Route 78 bridge have restricted flushing sufficiently to cause the observed changes. Potential causes also include increased nutrient and sediment loading from the rivers and runoff attributable to changes in land use.

The Vermont Agency of Natural Resources (ANR) contracted with Applied Science Associates, Inc. (ASA) for a modeling study of Missisquoi Bay. The sutdy consisted of four components; modeling hydrodynamics, flushing, suspended sediment transport and phosphorus. The study used a three-dimensional, boundary-fitted, general curvilinear coordinate system, hydrodynamics and mass transport model system to perform the simulations. The objective of this study was to use the integrated hydrodynamic and transport model system to investigate whether removal of the causeway, either all or in part, would have any predictable effects on the currents, sediment distribution or phosphorus concentrations in Missisquoi Bay or the Northeast Arm of the lake. This study was therefore designed as a comparative analysis; the case with the causeway vs. the case without the causeway.

The model was first used to simulate the hydrodynamic conditions (currents) in the bay and to investigate circulation patterns and effects for cases with and without the causeway. Sediment transport and phosphorus model components were then used to study transport, deposition and flushing attributes of the basin for similar conditions with and without the causeway.

A matrix of 33 test cases was run to evaluate the response of Missisquoi Bay to environmental forces (Table E.1). These cases included variations of environmental conditions (winds and river flow) and bridge geometry. The matrix of simulations and analysis of the results were aimed at determining how these forces affect flushing, sediment transport and deposition and phosphorus concentrations in the bay with the

causeway as it is now and to predict and compare those results with a similar set simulating the conditions should the causeway be removed.

Results

The following conclusions summarize the results of the four model applications taken together and generalize some of the more important findings.

- Model findings imply that the causeway does not hydraulically restrict the water flow between Missisquoi Bay and the Northeast Arm. Water does not 'pile up' behind the causeway for any of the cases tested. The causeway then merely represents an obstacle that the water must go around.
- For the majority of the cases, with a few exceptions, there is a persistent but small improvement in the flushing and sedimentation for cases with the causeway completely removed over the cases with the present causeway configuration.
- Differences between the cases with the present causeway configuration and cases with the causeway completely removed, when they do occur, are generally confined to the region in the vicinity of the causeway, bounded for the most part by North Hero Island in the south and Chapman Bay to the north.
- Differences in the velocities are generally not sufficient to result in additional sediment resuspension. In general velocities in the region of the causeway would be decreased from the resulting increase in cross-sectional area if the causeway were removed.
- Differences between the with and without causeway cases are substantially smaller than differences caused by variations in the environmental forces.
- Flushing and sedimentation differences caused by variations in the river flow rates are the most sensitive to the cross-sectional area at the causeway. As river flow decreases, the flushing time increases and the difference between with and without causeway cases increases, increasing flushing time for the present causeway configuration.
- Decreases in concentration of constituent within the bay were matched by increases in concentration (although generally more distributed) in the Northeast Arm.
- Decreases in sedimentation within the bay were matched by increases of sedimentation in the Northeast Arm.
- The model needs field verifications and would benefit from long term, time variable simulation with real winds and real river flow data.

Table E.1 Missisquoi Bay model simulation matrix

B = Base case definition
South-southwest wind
@ 10 mph
Mean lake level (95.8')
High river flow
Railroad trestle present

Case description
B1 - Base case with present causeway configuration
B2 - Base case with the causeway completely removed
1 - Wind direction variation test (west) with causeway
2 - Wind direction variation test (west) without causeway
3 - Wind speed variation test (20 mph) with causeway
4 - Wind speed variation test (20 mph) without causeway
5 - Wind speed variation test (30 mph) with causeway
6 - Wind speed variation test (30 mph) without causeway
7 - Low wind speed test (5 mph) without causeway
8 - Lake level variation test (high lake level) without causeway
9 - River flow variation test (low flow) without causeway
10 - Railroad trestle variation (no trestle) with causeway
11 - Railroad trestle variation (no trestle) without causeway
12 - Real wind forcing (variable winds - typical spring conditions) with causeway
13 - Real wind forcing (variable winds - typical spring conditions) without causeway
14 - Causeway removal configuration test (center removed)
15 - Causeway removal configuration test (25% from each shore removed)
16 - Wind direction variation test (north) with causeway
17 - Wind direction variation test (north) without causeway
18 - Wind direction variation test (north east) with causeway
19 - Wind direction variation test (north east) without causeway
20 - Wind direction variation test (east) with causeway
21 - Wind direction variation test (east) without causeway
22 - Wind direction variation test (south east) with causeway
23 - Wind direction variation test (south east) without causeway
24 - Wind direction variation test (south west) with causeway
25 - Wind direction variation test (south west) without causeway
26 - Wind direction variation test (north west) with causeway
27 - Wind direction variation test (north west) without causeway
28 - Wind direction variation test (no wind) with causeway
29 - Wind direction variation test (no wind) without causeway
30 - (7A) Low wind speed test (5 mph) with causeway
31 - (9A) River flow variation test (low flow) with causeway
32 - Diffusion only test, no river flow, no wind flow, with causeway
33 - Diffusion only test, no river flow, no wind flow, without causeway

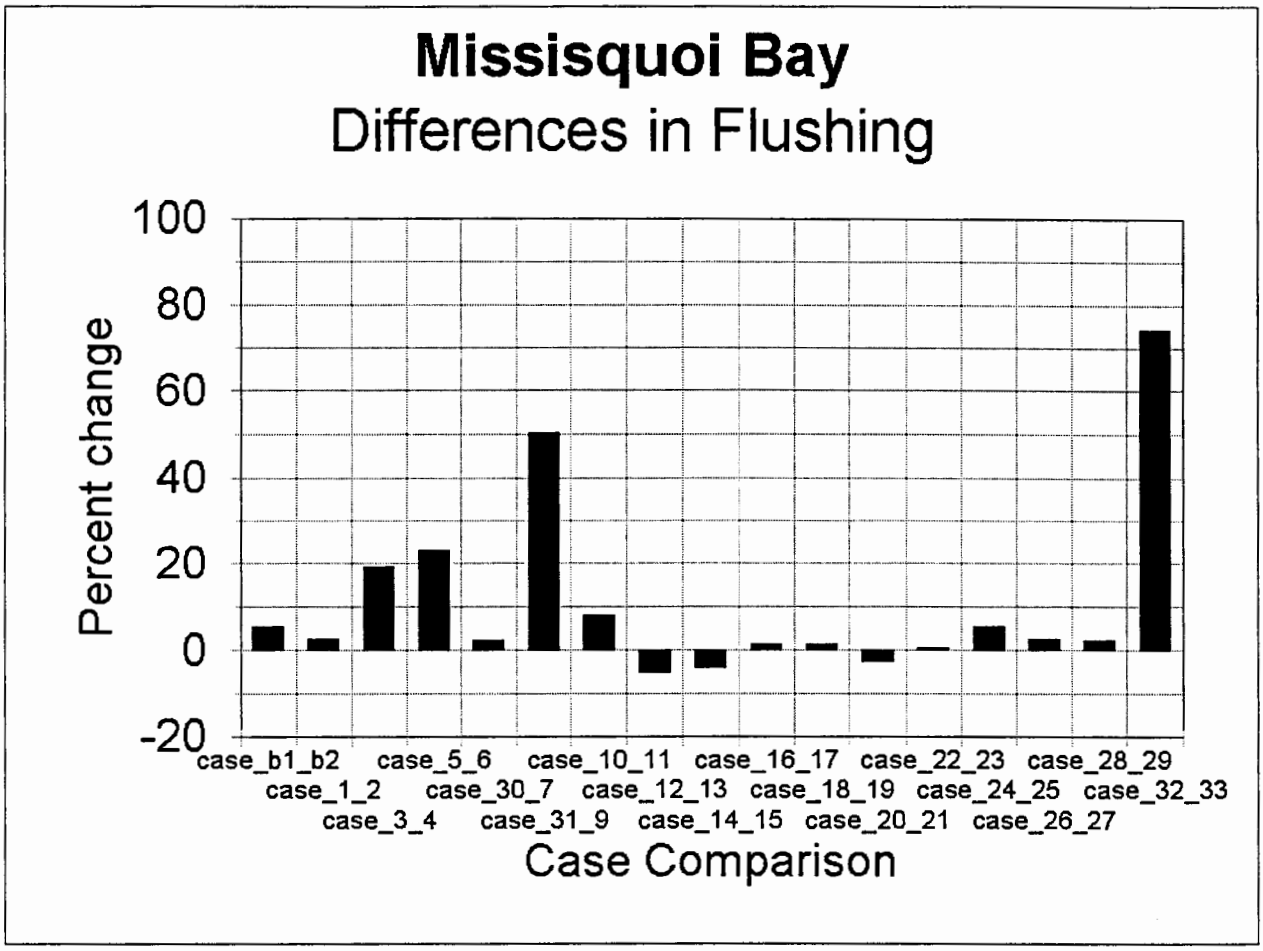

Figure E.1 **Differences in flushing between cases with and without the causeway. Refer to Table E.1 for case descriptions.**

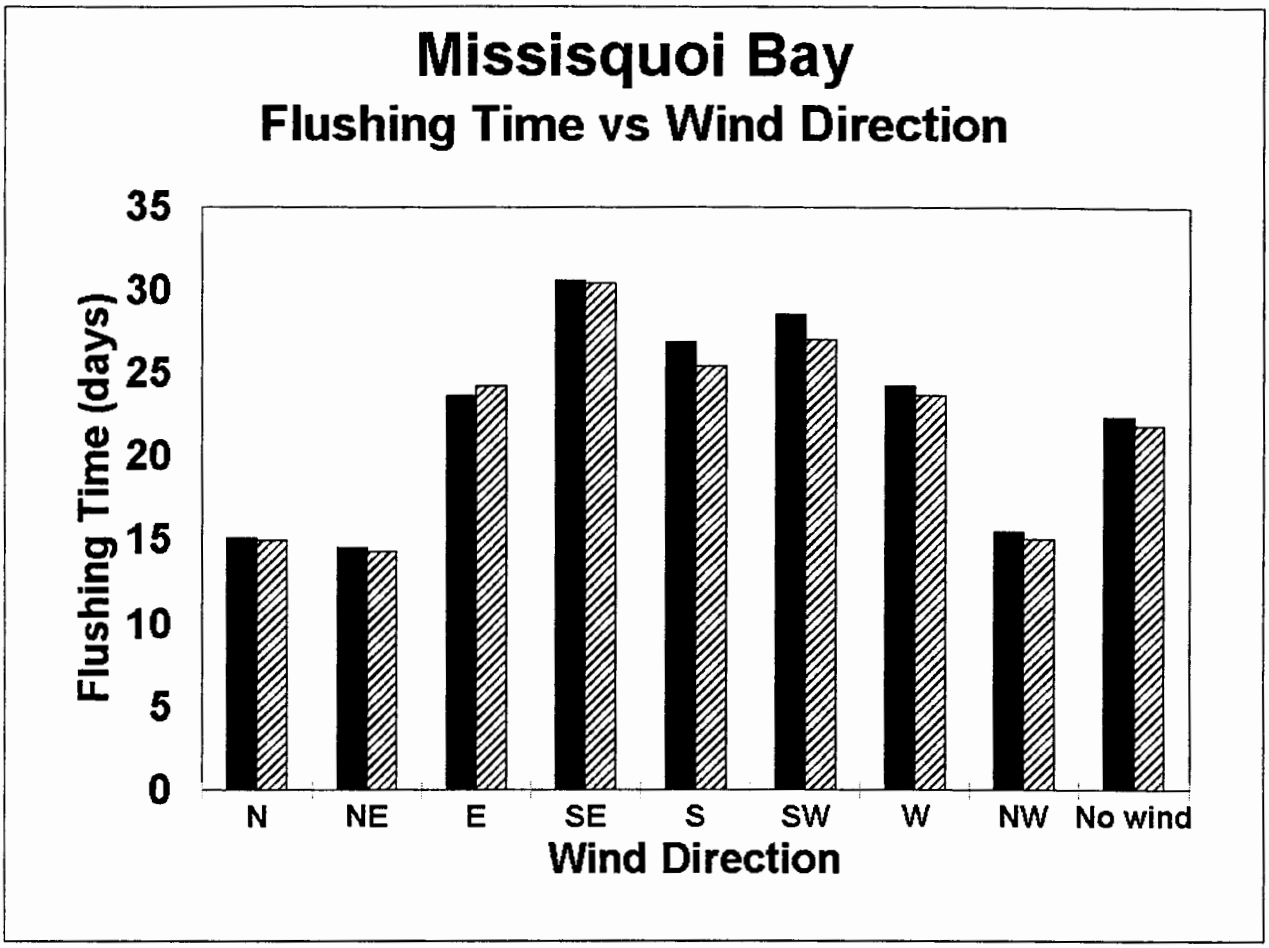

Figure E.2 **Flushing time versus wind direction for cases with and without the causeway. For each pair of cases the solid bar on the left represents the case with the causeway and the hatched bar the case without the causeway .**

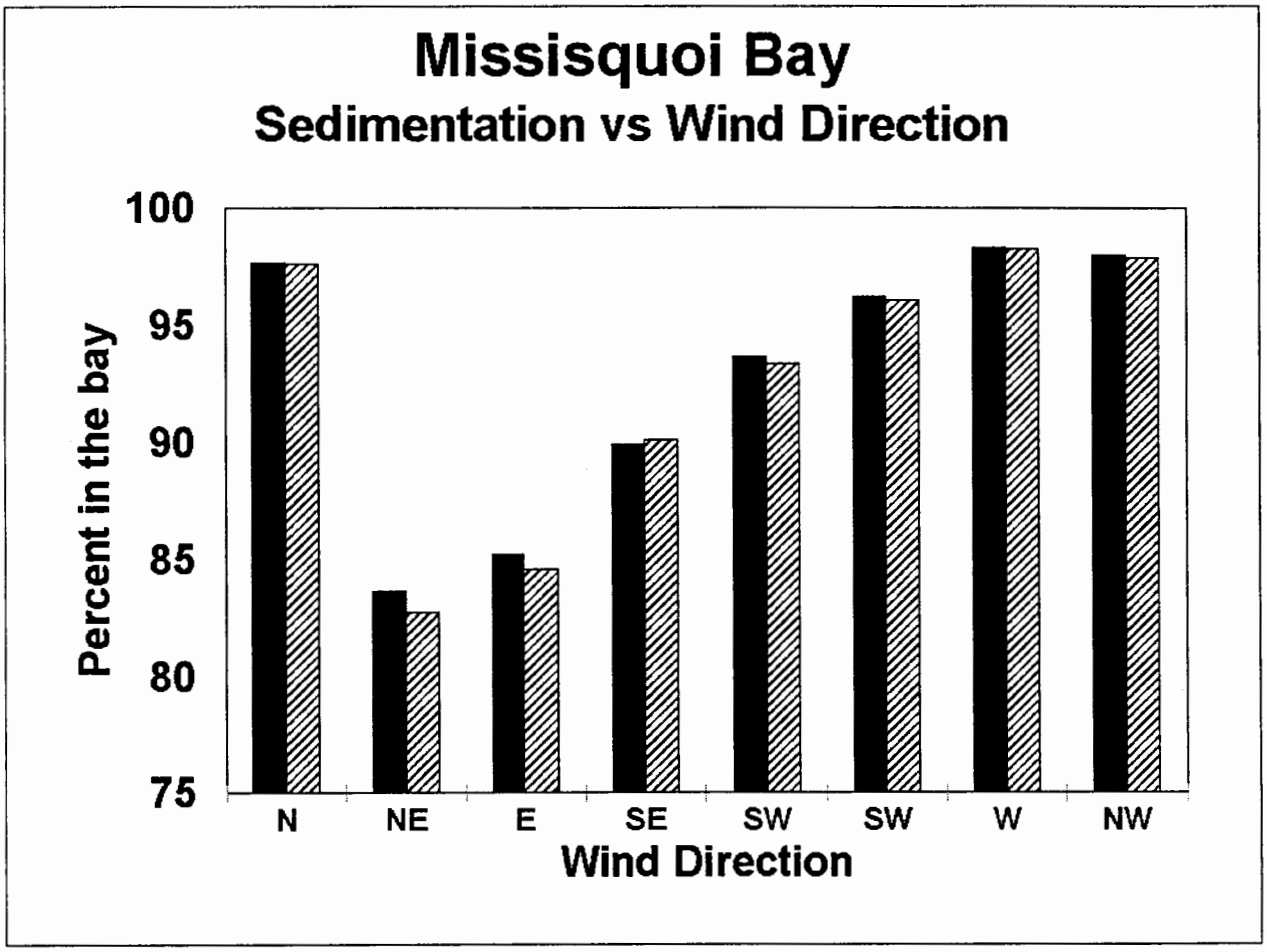

Figure E.3 **Percentage sedimentation within Missisquoi Bay versus wind direction for cases with and without the causeway. For each pair of cases the solid bar on the left represents the case with the causeway and the hatched bar the case without the causeway .**

1. INTRODUCTION

1.1 Background

Missisquoi Bay is a small embayment located in the northeast quadrant of Lake Champlain. It encompasses an area of approximately 77.5 km^2) and has a maximum depth of approximately 4 m (14 ft) (Myers and Gruendling, 1970). Major tributaries to the bay are the Missisquoi, Pike and Rock Rivers. The Swanton-Alburg Route 78 bridge is located at the southern end (mouth) of the bay and consists of two causeway sections approximately 530 m (1750 ft) long extending from each shore and a bridge section 170 m (560 ft) long (Figure 1.1).

Citizens have observed changes in the bay since the bridge was built in 1937. The bay bottom is remembered to consist primarily of sand with vegetation clumps with a series of sandy beaches throughout the bay. Areas in the bay were also remembered as a fish (walleye) spawning habitat, with clean cobble areas in shallow water.

Today the bottom sediments tend to be silt and organic material. Many areas have been identified to be filled in with vegetation as well. This has adversely effected fish habitat as well as recreational uses of the bay.

Residents have noted that the bay has deteriorated over time and believe that the causeways at the Route 78 bridge have restricted flushing sufficiently to cause the observed changes. Another potential cause is increased nutrient and sediment loading from the rivers and runoff. With present observed levels of phosphorus in the bay it is entirely possible that eutrophic conditions are causing the increase in organic materials on the bottom. Changes in land use can increase sediment loads in the tributaries.

Unfortunately there is a dearth of data relative to the condition of Missisquoi Bay before the construction of the bridge. Thus there is no conclusive way to prove or disprove the potential adverse effects of the causeway on the bay. One potential alternative, however, to determine impacts is to simulate the conditions with and without the bridge through the use of a computer model.

The Vermont Agency of Natural Resources (ANR) has contracted with Applied Science Associates, Inc. (ASA) for a modeling study of Missisquoi Bay. The modeling is intended to simulate the hydrodynamic conditions (currents) in the bay and to

study_a.bmp

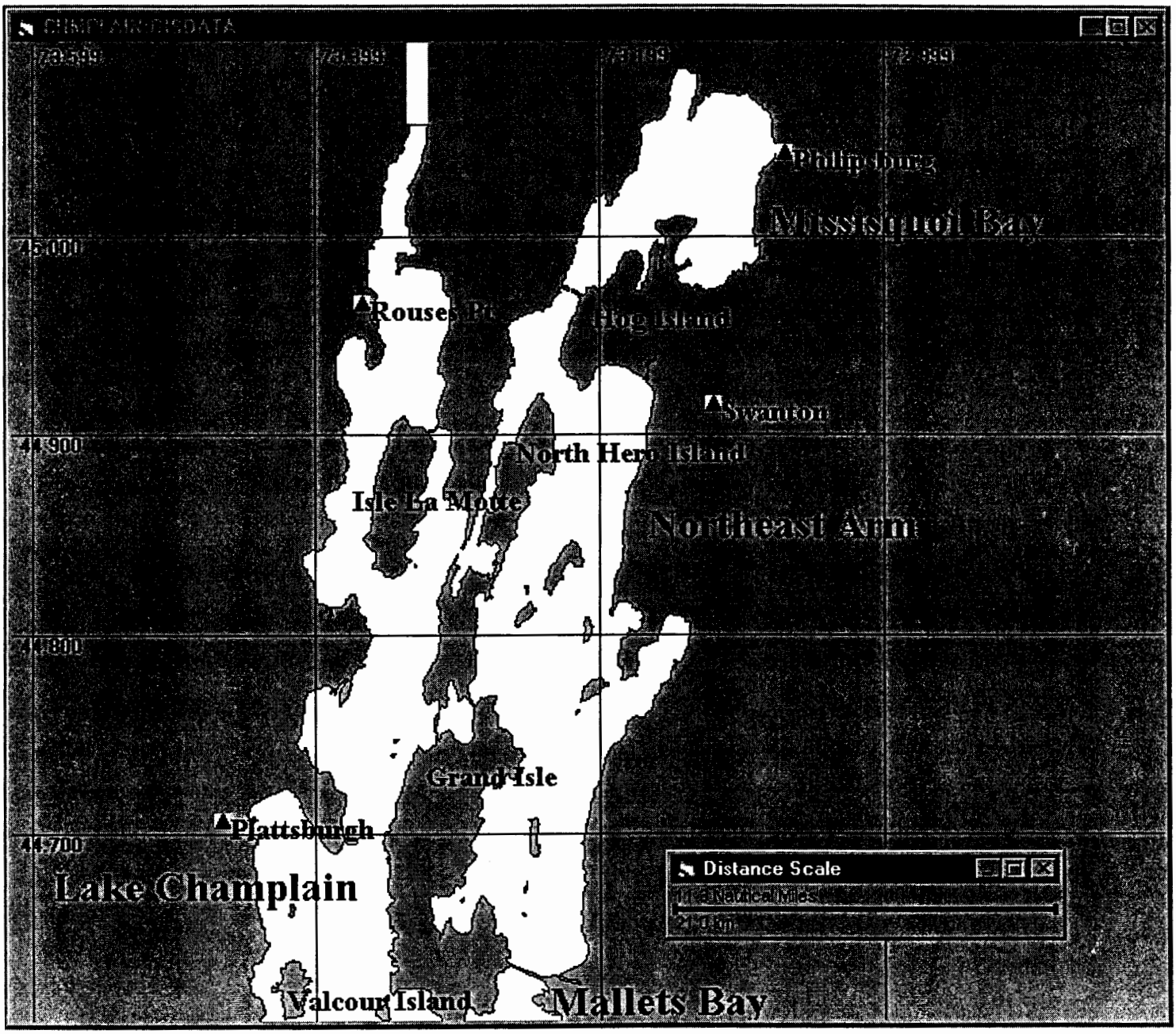

Figure 1.1 Missisquoi Bay study area.

investigate circulation patterns and effects for cases with and without the causeway. Sediment transport and phosphorus model components are also included in the study.

1.2 Study Objective

The objective of this study is to use the integrated hydrodynamic and transport model system to consider and answer the following questions:

1) Will removal of the causeway, either all or in part, have any predictable effects on the currents, sediment distribution or phosphorus concentrations in Missisquoi Bay or the Northeast Arm of the lake.

2) If any effects from causeway removal are predicted, how significant are they and how far do the effects extend into the bay and the Northeast Arm.

This study has therefore been designed as a comparative analysis; the case with the causeway vs. the case without the causeway. The set of simulations that have been developed were designed to evaluate the conditions under which any differences, between cases with and without the causeway, in the circulation patterns, flushing of the bay, sediment transport or water column phosphorus concentration in the bay might occur. Some explanation for that difference is then sought.

The following sections document this computer modeling approach. Section 2 provides a review of the available environmental data for the area. Section 3 describes the models used in the analysis and the technical approach while Section 4 details the application to Missisquoi Bay. Section 5 discusses the matrix of model runs performed, Section 6 presents results and Section 7 gives conclusions.

2. REVIEW OF ENVIRONMENTAL DATA

2.1 Weather Data

Wind data was received from Marcel Laganiere at the Direction de l'hydraulique, Ministere de l'Environnement, Sainte-Foy, Quebec, for the Philipsburg station [7026040 (R-6)]. The statistics table for the wind data is included as Appendix A. The data covers the years 1976 - 1995, with two observations per day. The wind speed distribution for the entire time series (during the period April through November) was determined and is shown in Figure 2.1. The most frequent speed was 10 mph (4.5 m/s)

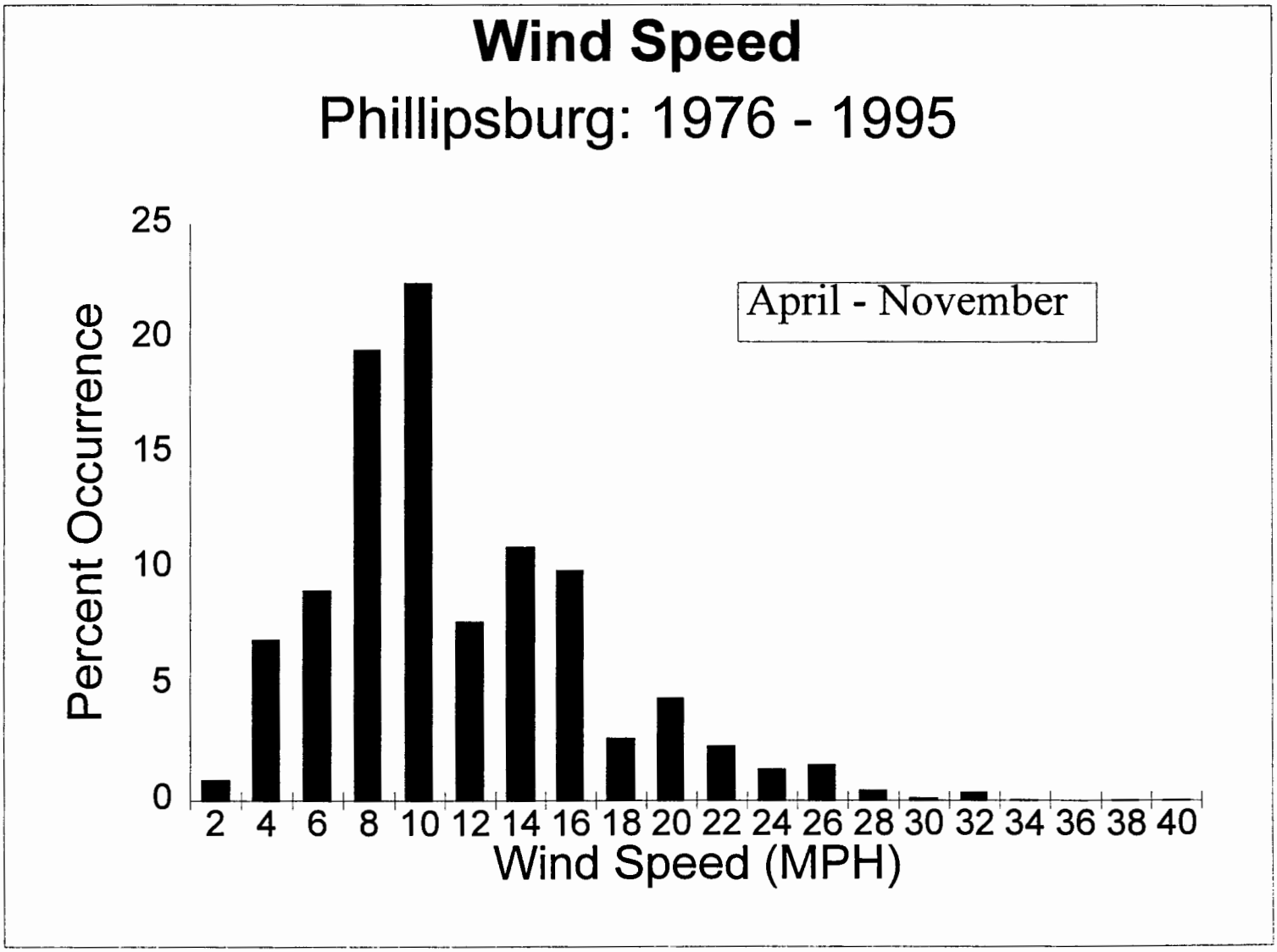

Figure 2.1 Wind speed distribution (% occurrence) for the Philipsburg station during the years 1976-1995.

at 23%, followed closely by 8 mph (3.6 m/s) at 19%. A band between 4 - 16 mph (1.8 - 7.2 m/s) accounts for between 5 and 10% of the total wind record in each 2 mph (0.9 m/s) speed bin, (a total of 7 bins).

The data was arbitrarily broken up into four segments (1976-1979, 1980-1984, 1985-1989, and 1990-1995 to see the variability of directional occurrence with time. Each of the segments and the entire time series was analyzed (Table 2.1 and Figure 2.2) for the months of April through November. Over the 20 year period 1976 - 1995 the average predominant direction is from the south (occurring 20.5 % of the time) with a secondary predominant direction from the west (occurring 14.0% of the time). When examining the four segments, however, the results are less clear. For 1976-1979 southwest winds predominated (25.2 % of the time) followed by west winds (23.4 % of the time), for 1980-1984 south winds predominated (19.0 % of the time) followed by west winds (15.3 % of the time), for 1985-1989 south winds predominated (25.6 % of the time) followed by north winds (11.1 % of the time) and for 1990-1995 south winds again predominated (18.8 % of the time) followed by west (11.5 % of the time). This variability for the segments makes it difficult to statistically determine the predominant directions. The primary predominant direction was taken as south southwest. West was chosen as the secondary predominant direction.

2.2 River Flow Data

River flow data was obtained from a variety of sources, both in Canada and the United States. A summary of mean flows into Missisquoi Bay was reported by Smeltzer (1994) in his analysis of water quality using a box model approach. He reported mean annual flows from the 1991 hydrologic base year of 1307 X 10^6 m^3/yr (46.15 X 10^9 ft^3/yr) for the Missisquoi River, 296 X 10^6 m^3/yr (1.045 X 10^9 ft^3/yr) for the Pike River and 69 X 10^6 m^3/yr (2.436 X 10^9 ft^3/yr) for the Rock River. Ungaged areas were estimated to provide another 36 X 10^6 m^3/yr (1.271 X 10^9 ft^3/yr) giving a total river flow entering the bay of 1708 X 10^6 m^3/yr (60.31 X 10^9 ft^3/yr).

To develop a better sense of the variability of the river flow entering Missisquoi Bay, the actual daily flow records were obtained from gaging stations on the rivers for the period from March 1990 through April 1992. The daily flow rate for Missisquoi

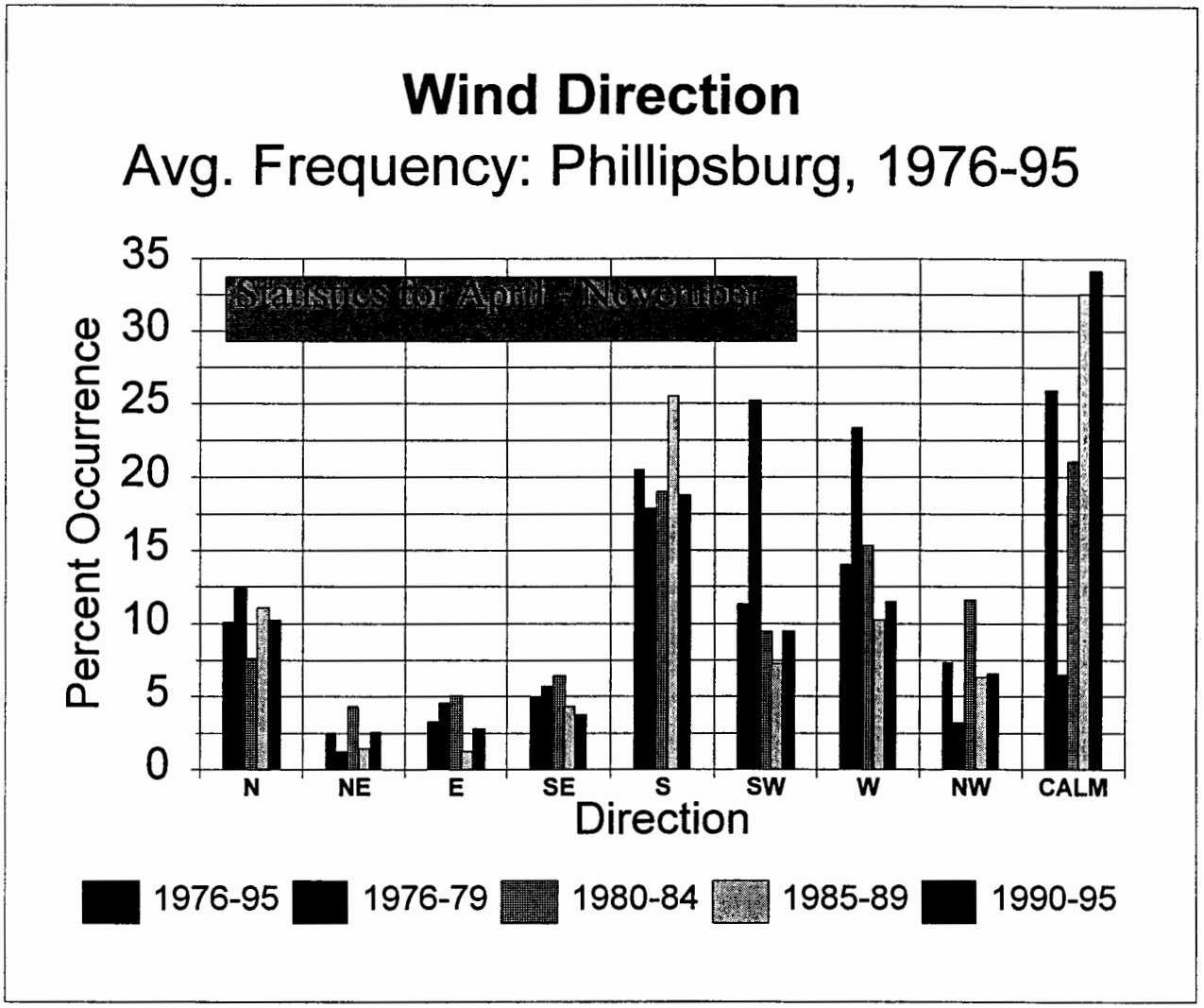

Figure 2.2 Wind direction distribution (% occurrence) for the Philipsburg station during the years 1976-1995.

TABLE 2.1 Wind Percent Occurrence by Direction: Phillipsburg, 1976 - 1995 : (Apr - Nov.)

	DIRECTION									
DATE	N	NE	E	SE	S	SW	W	NW	CALM	# obs
1976-79	12.4	1.2	4.6	5.7	17.9	25.2	23.4	3.2	6.5	1404
1980-84	7.6	4.3	5.1	6.4	19.0	9.5	15.3	11.6	21.1	2440
1985-89	11.1	1.4	1.2	4.3	25.6	7.3	10.2	6.3	32.6	2440
1990-95	10.3	2.6	2.8	3.8	18.8	9.5	11.5	6.6	34.2	2806
1976-95	10.1	2.5	3.3	4.9	20.5	11.3	14.0	7.3	26.0	9090

River (station 04294000) is shown in Figure 2.3. Also shown is a bold solid line indicating the mean river flow of 1810 ft^3/s (51.3 m^3/s). To obtain the mean high flow all values above the mean were averaged to give 4110 ft^3/s (116 m^3/s). This procedure was followed to account for the fact that the model will be run for an extended period (greater than one month) under steady conditions. Since high flows usually last for a much shorter period, this procedure produced a reasonable estimate. A similar procedure was followed to obtain a mean low flow of 787 ft^3/s (22.3 m^3/s). Both mean high flow and mean low flow are shown in Figure 2.3 by dashed lines.

This analysis was repeated for the Rock River (station 04294300) and is shown in Figure 2.4. The mean river flow was 87.5 ft^3/s (2.48 m^3/s), the mean high flow was 311 ft^3/s (8.81 m^3/s) and the mean low flow was 12 ft^3/s (0.34 m^3/s).

The analysis was again repeated for the Pike River (station 030420) and is shown in Figure 2.5. The mean river flow was 364 ft^3/s (10.3 m^3/s), the mean high flow was 909 ft^3/s (25.7 m^3/s) and the mean low flow was 131 ft^3/s (3.71 m^3/s). Table 2.2 summarizes the mean flow calculations.

Table 2.2 Mean River Flow Into Missisquoi Bay, 1990-1992

River	Mean Low Flow (m^3/s)	Mean Flow (m^3/s)	Mean High Flow (m^3/s)
Missisquoi	22.29	51.28	116.39
Rock	0.34	2.48	8.81
Pike	3.70	10.30	25.75

2.3 Missisquoi Bay Sediment

Based solely on the distribution of sand and clay sized particles (Hunt, 1971), the majority of lake bottom sediment enters Missisquoi Bay from three rivers - the Missisquoi River; the Pike River; and the Rock River. The Missisquoi River is inferred to be the largest sediment source based on the delta formation at the south end of the bay, and the large flow rate relative to the other two rivers.

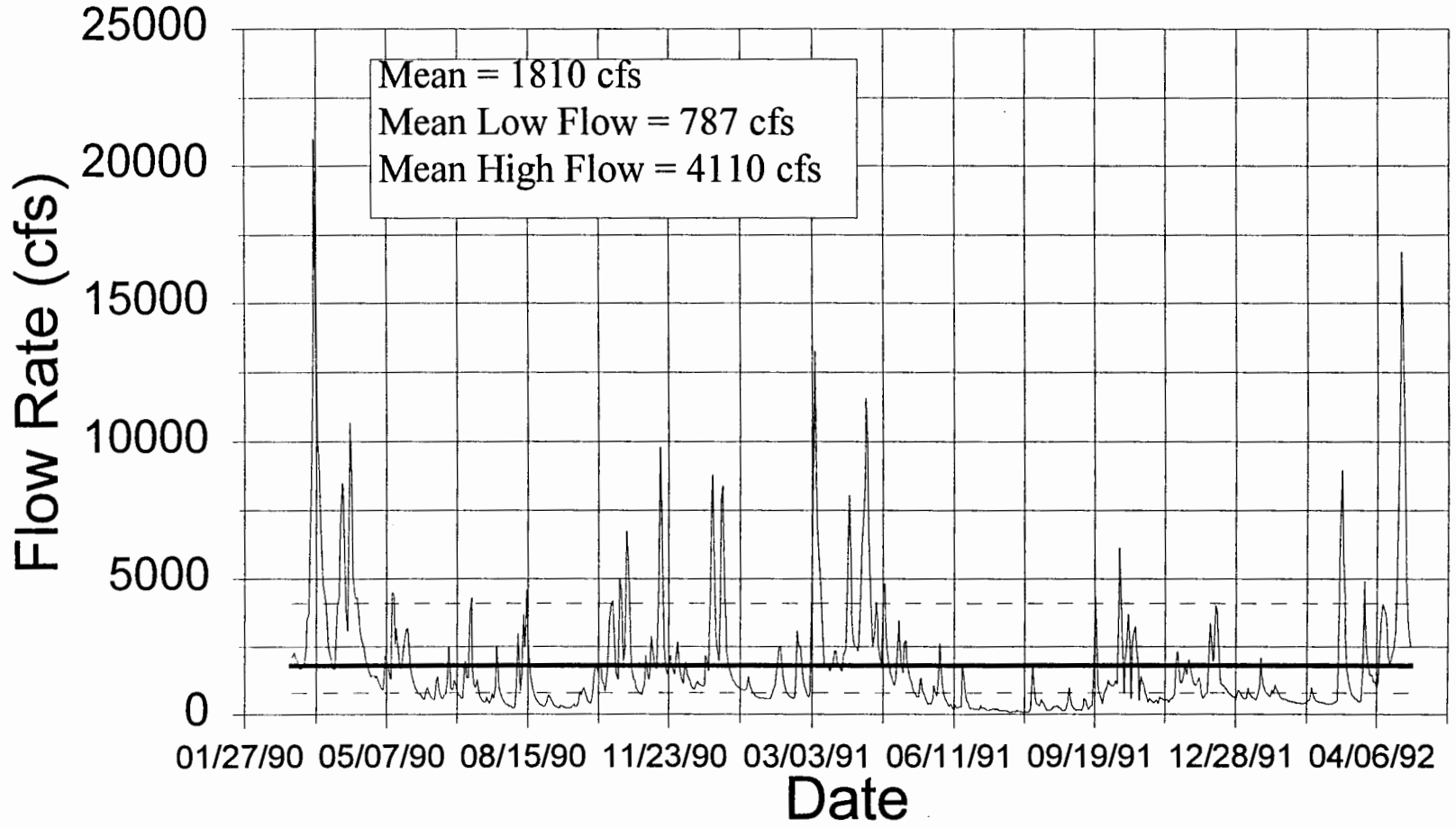

Figure 2.3 Flow rate for the Missisquoi River for the period March 1990 through April 1992.

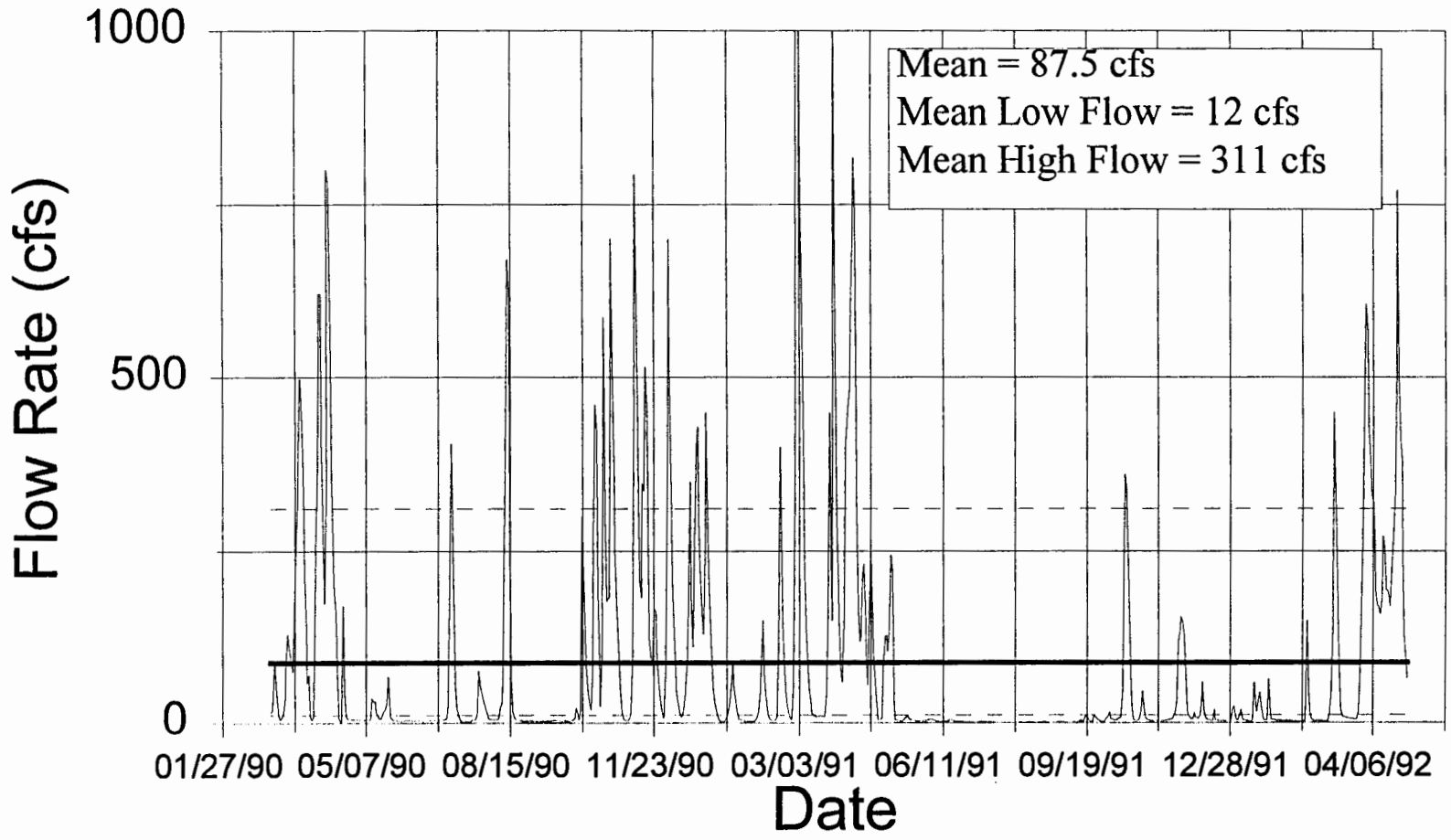

Figure 2.4 Flow rate for the Rock River for the period March 1990 through April 1992.

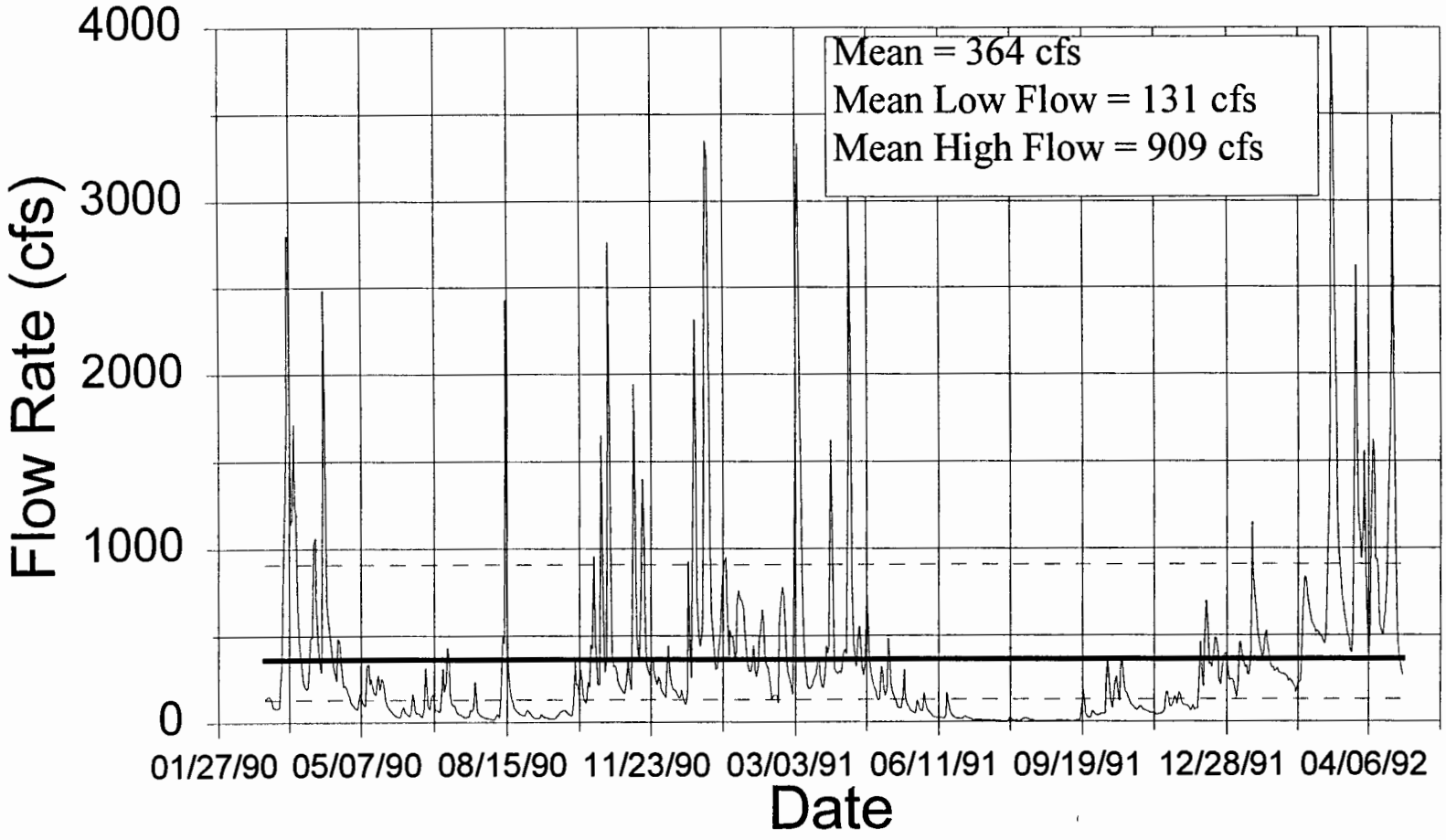

Figure 2.5 Flow rate for the Pike River for the period March 1990 through April 1992.

The general sediment distribution pattern is displayed in Figures 2.6 and 2.7. Figure 2.6 shows sand as a percentage of total bottom sediment. Sand is transported as bed load and deposited in deltas at the mouths of each of the rivers entering Missisquoi Bay. High sand percentages off Jameson Point, McFee Point, Province Point, and McGregor Point are evidence of long shore transport from north to south within the lake. A possible scenario for sediment transport within the lake calls for sand sized particles to be transported along shore from the delta source to adjacent sections of coast and nearshore lake bottom.

Figure 2.7 shows clay as a percentage of total bottom sediment. High clay percentages occur in the central basin of Missisquoi Bay, and in a small basin north of the causeway. Nearshore areas are predominately sand with clay percentages in the range of 10 to 30%. The pelagic muds deposited in the lake basins are likely to have been deposited by density flows from the contributing rivers.

Monitoring data of suspended sediment concentrations in the three tributaries to the bay was compiled by the VTDEC and NYSDEC (VTDEC & NYSDEC, 1994) for the 2 year period between November 1992 and December 1994. Figures 2.8 and 2.9 show the Total Suspended Sediment (TSS) concentration vs date for the Missisquoi and Pike rivers respectively. Table 2.3 summarizes the minimum, maximum and mean concentration statistics for the data. The suspended sediment concentration data does not, however, divulge any information on the particle size distribution of the sediments.

Table 2.3 Total Suspended Solids Concentration Statistics between 1992 and 1994.

River	Min (mg/L)	Mean (mg/L)	Max (mg/L)
Missisquoi	1.9	30.62	122.0
Pike	1.0	24.75	74.3

3. MODEL DESCRIPTION

For the Missisquoi Bay hydrodynamics study we used a PC-based modeling system, WQMAP (Mendelsohn et al, 1995; Swanson and Mendelsohn, 1994;

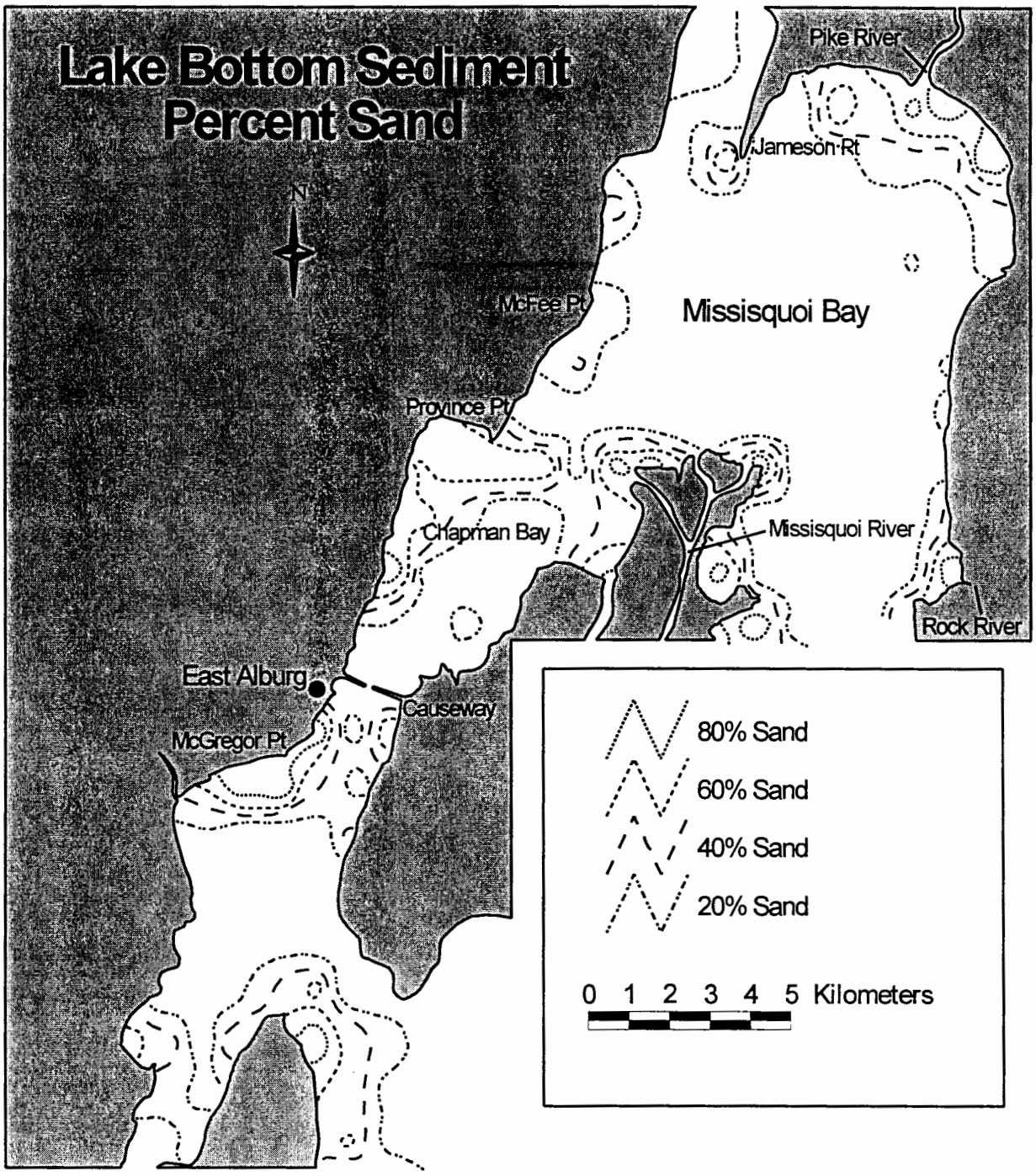

Figure 2.6 Map showing the percentage of sand in bottom sediment for Missisquoi Bay. The contour interval is 20%. Source: Hunt, 1971.

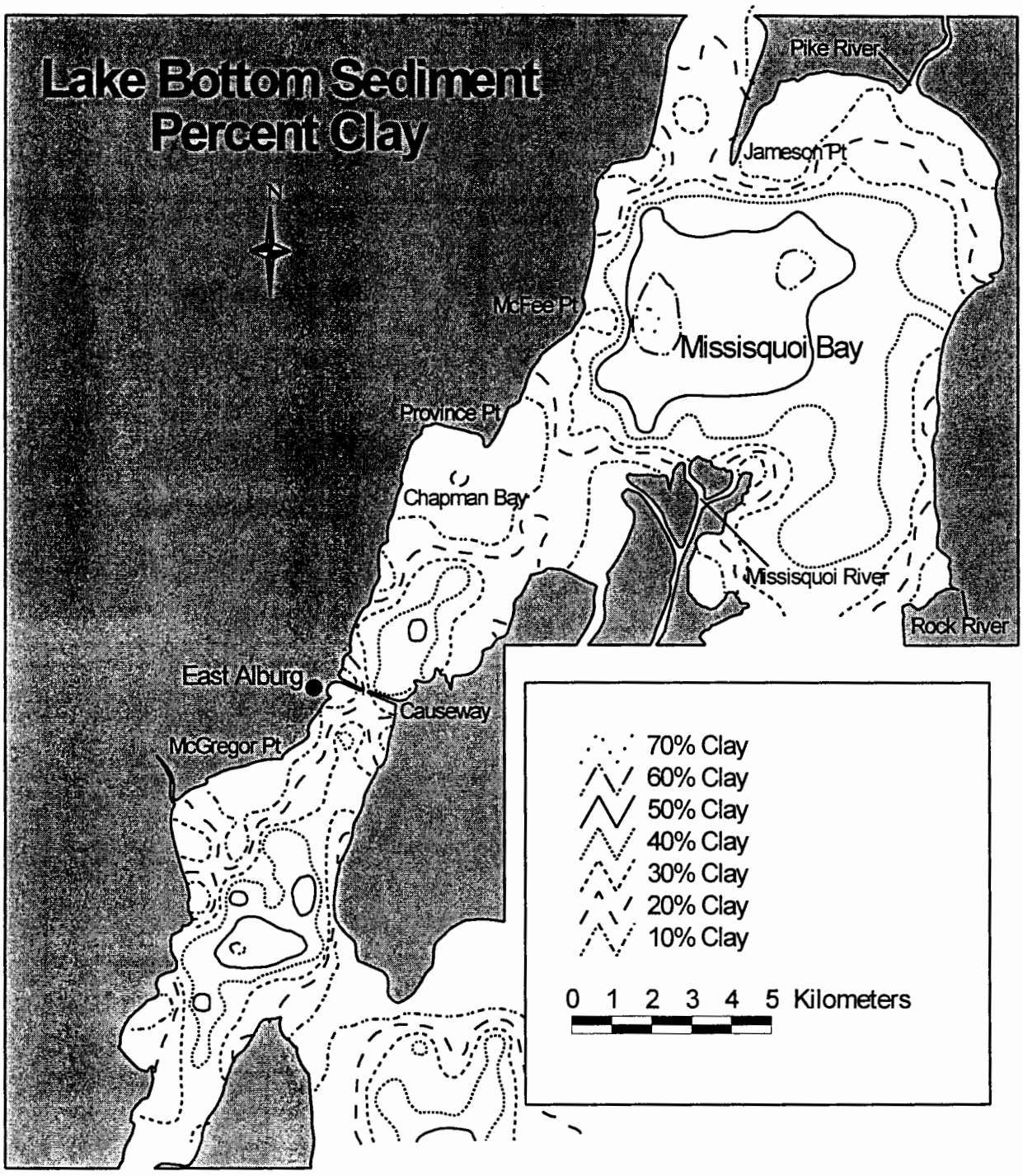

Figure 2.7 Map showing the percentage of clay sized particles in bottom sediment for Missisquoi Bay. The contour interval is 10%. Source: Hunt, 1971.

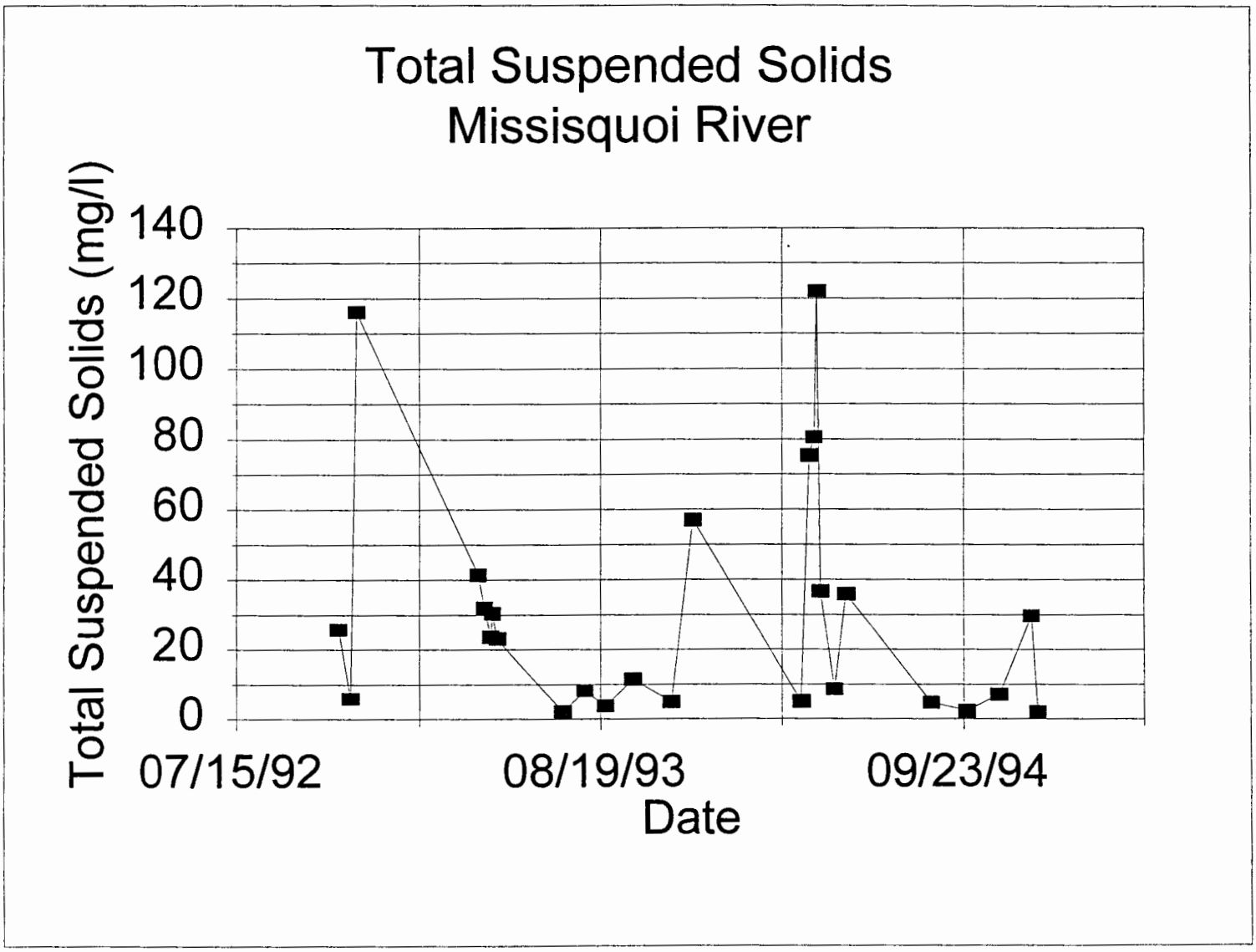

Figure 2.8 Total suspended solids concentration in the Missisquoi River, 1992-1994 (VTDEC, 1994).

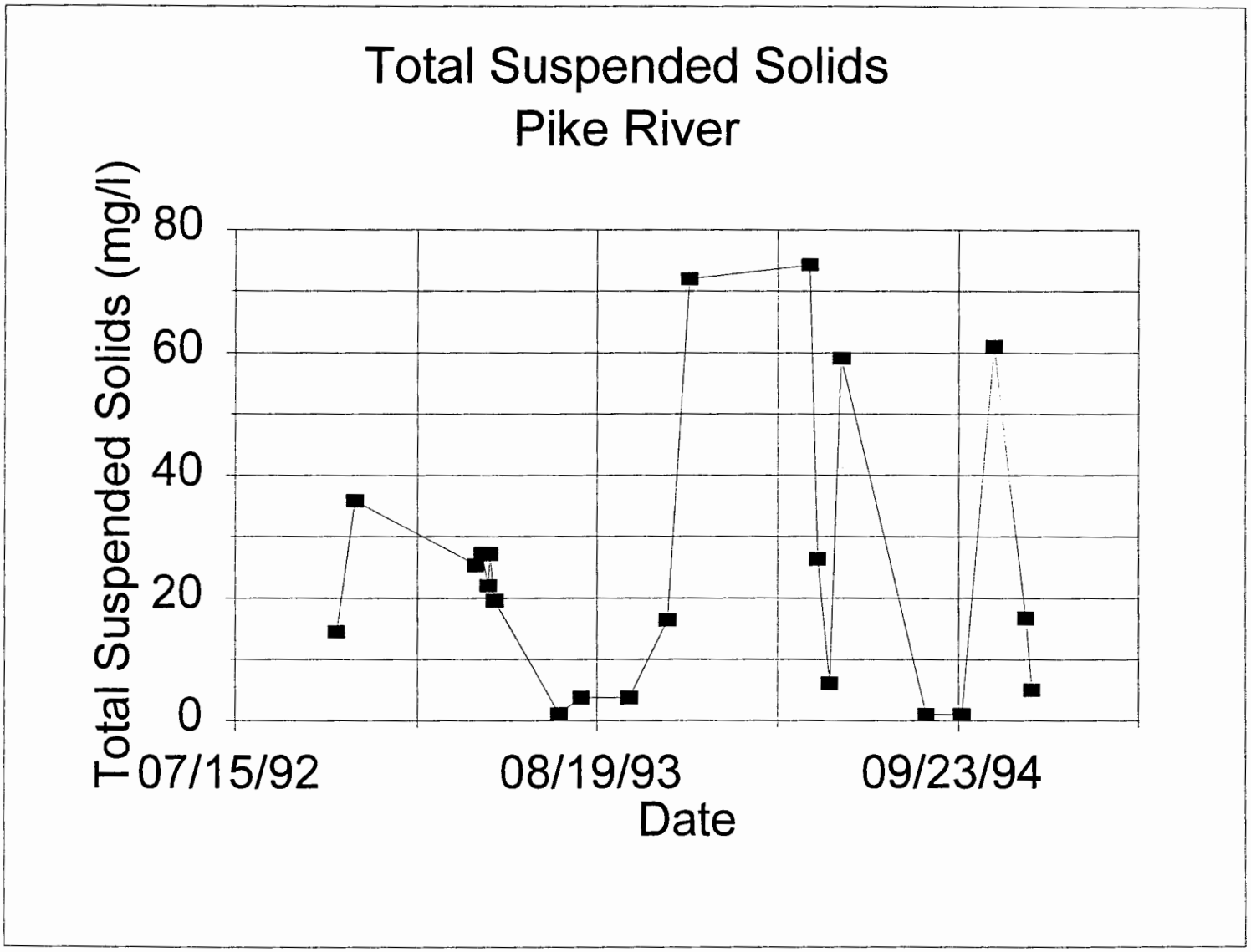

Figure 2.9 Total suspended solids concentration in the Pike River, 1992-1994 (VTDEC, 1994).

Mendelsohn and Swanson, 1992), which integrates geographic information (land use, watershed attributes, point sources), environmental data (water quality parameters, stream flows, bathymetry) and process models (hydrodynamic, pollutant transport, sediment transport, wave).

For the Missisquoi project we used the three-dimensional boundary fitted hydrodynamic model linked with the three-dimensional single constituent mass transport model variously configured to simulate the flushing of a conservative substance, sediment transport and a simplified phosphorus reaction.

3.1 Hydrodynamic Model

The numerical model selected for use in this study is a boundary fitted model which matches the model coordinates with the shoreline boundaries of the water body. This approach is consistent with the highly variable geometry of Missisquoi Bay. Development of this model has proceeded over the last decade (Spaulding, 1984; Swanson, 1986; Swanson et al., 1989; Muin, 1993; and Muin and Spaulding, 1996).

The boundary fitted method uses a set of coupled quasi-linear elliptic transformation equations to map an arbitrary horizontal multi-connected region from physical space to a rectangular mesh structure in the transformed horizontal plane (Spaulding, 1984). The three dimensional conservation of mass and momentum equations, with approximations suitable for lakes, rivers, and estuaries (Swanson, 1986; Muin, 1993) that form the basis of the model, are then solved in this transformed space. In addition an algebraic transformation is used in the vertical to map the free surface and bottom onto coordinate surfaces (Gordon, 1982). The resulting equations are solved using an efficient semi-implicit finite difference algorithm for the exterior mode (two dimensional vertically averaged) and by an explicit finite difference leveled algorithm for the vertical structure of the interior mode (three dimensional) (Madala and Piascsek, 1977; Swanson, 1986).

A detailed description of the model with associated test cases is included as a manuscript in Appendix B. A brief description of the model follows.

The basic equations are written in spherical coordinates to allow for accurate representation of large model areas. The conservation equations for water mass, momentum (in three dimensions) and constituent mass (e.g. chloride) form the basis of

the model. It is assumed that the flow is incompressible, that the fluid is in hydrostatic balance, the horizontal friction is not significant and the Boussinesq approximation applies.

The boundary conditions are as follows. At land the normal component of velocity is zero. At open boundaries the free surface elevation must be specified and temperature and salinity specified on inflow. On outflow temperature and salinity is advected out of the model domain. A wind stress is applied at the surface. A bottom stress or a no slip condition can be applied at the bottom.

To allow the same relative resolution of the vertical structure throughout the model domain, a vertical coordinate transformation is employed. This technique maps the free surface and bottom topography onto coordinate surfaces analogous to the boundary fitted approach in the horizontal.

There are a number of options for specification of vertical eddy viscosity, A_v, (for momentum) and vertical eddy diffusivity, D_v, (for constituent mass). The simplest formulation is that both are constant, A_{vo} and D_{vo}, throughout the water column. They can also be functions of the local Richardson number which, in turn, is a function of the vertical density gradient and vertical gradient of horizontal velocity. A more complex formulation adds the dependence on mixing length and turbulent energy. Details can be found in Appendix B and Muin (1993).

The set of governing equations with dependent and independent variables transformed from spherical to curvilinear coordinates, in concert with the boundary conditions, is solved by a semi-implicit, split mode finite difference procedure (Madala and Piascek, 1977; Swanson, 1986). The equations of motion are vertically integrated and, through simple algebraic manipulation, are recast in terms of a single Helmholtz equation in surface elevation. This equation is solved using a sparse matrix solution technique to predict the spatial distribution of surface elevation for each grid.

The vertically averaged velocity is then determined explicitly using the momentum equation. This step constitutes the external or vertically averaged mode. Deviations of the velocity field from this vertically averaged value are then calculated, using a tridiagonal matrix technique. The deviations are added to the vertically averaged values to obtain the vertical profile of velocity at each grid cell thereby generating the complete current patterns. This constitutes the internal mode. The

methodology allows time steps based on the advective, rather than the gravity, wave speed as in conventional explicit finite difference methods, and therefore results in a computationally efficient solution procedure (Swanson, 1986; Swanson et al., 1989; Muin, 1993).

3.2 Constituent Transport Model

The constituent transport model solves the conservation of mass equation on the same boundary fitted grid used for the hydrodynamic model (Muin, 1993; Mendelsohn and Swanson, 1992). The constituent transport model uses the current data calculated by the hydrodynamic model to simulate the transport of the material being modeled (e.g. chloride, sediments, phosphorus) and predict where it will go and its concentration in the water. This precludes the necessity for aggregation or interpolation of currents thereby avoiding unnecessary diffusive or numerical smoothing effects often associated with such postprocessing.

The model includes a various configurations of loss terms to allow the simulation of wide variety of different materials. The loss rate terms include linear and non-linear decay, settling and bulk loss. Single and multiple, constant and time varying loads can be applied. Constituents can include pathogens, excess temperature, metals, nutrients, organics, sediments and conservative tracers such as dye. More advanced model options include the use of a set of constituent equations linked by a suitable reaction matrix which uses the EPA WASP eutrophication model kinetics.

4. MODEL APPLICATION TO MISSISSQUOI BAY

The WQMAP system was applied to Missisquoi Bay and adjacent waters in the Northeast Arm. This application first entailed the generation of a basemap of the area. The base map was digitized from NOAA chart #14781, (Riviere Richlieu to South Hero Island) of the area. Then a grid of quadrilaterals was created using gridding tools in WQMAP overlaying Missisquoi Bay and the Northwest Arm as shown in Figure 4.1. This grid was optimized to closely track the shoreline and provide sufficient resolution to describe the variability in the bay. Particular attention was paid to the area around the highway causeway. Figure 4.2 shows a detail of the causeway gridding and the nearby

grid1.bmp

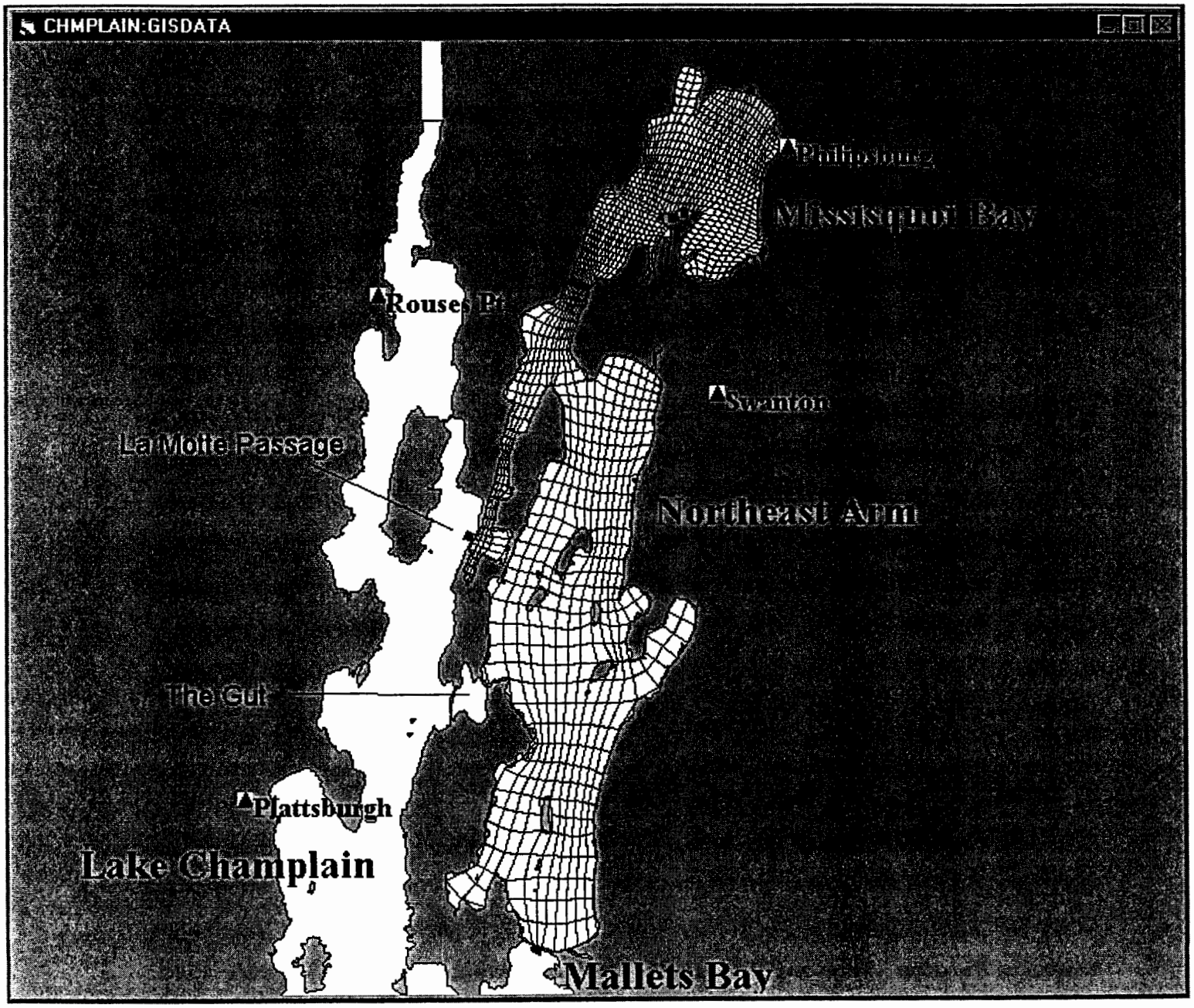

Figure 4.1 Model grid for Missisquoi Bay.

grid2.bmp

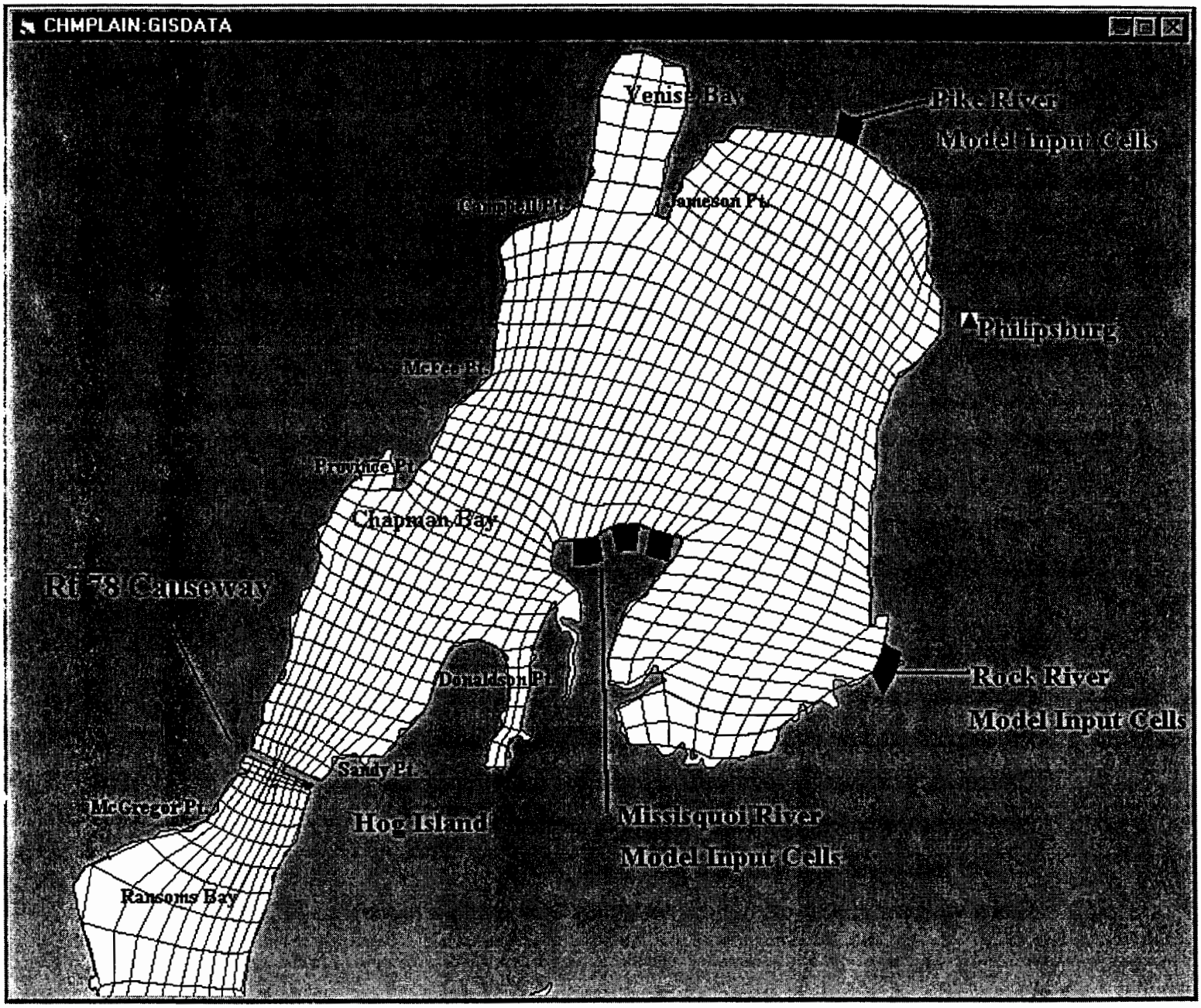

Figure 4.2 Model grid for the area around the Route 78 causeway.

railroad trestle to the south with the present causeway configuration. The grid dimensions are 34x84 total cells in the east and north directions respectively. A total of 1415 computational (water) cells were used to model the area. Five levels were used in the vertical direction to simulate the vertical current velocity structure.

At the southern extreme, the grid has an open boundary condition to simulate the small opening to Mallets Bay from the Northeast Arm. In addition, there are two other openings, one at Carry Bay to the La Motte Passage and the other at the Gut between North and South Hero Islands, to the main lake. In Missisquoi Bay the model grid has river boundary cells to represent the three rivers entering the bay; the Missisquoi which has three separate branches, the Rock and the Pike.

Bathymetry data was also taken from NOAA Chart 14781. The data was digitized and input to WQMAP which was used to generate depths for each grid cell by an automatic interpolation routine based on distance weighting.

At total of 7 different grids (variations on the grid described above), were used for the model simulations in the matrix of cases (Section 5 below), to incorporate the various causeway and railroad trestle configurations. The depths were assumed to be at the mean stage for all but one of the grids which used high lake level depths. A description of the variations in each of the 7 grids follows:

1. Present causeway configuration.
2. Causeway completely removed.
3. Present causeway configuration, without the railroad trestle.
4. Causeway completely removed, without the railroad trestle.
5. 50% of the causeway removed from the center.
6. 25% of the causeway removed from each shore.
7. Causeway completely removed, with high lake level bathymetry.

4.1 Hydrodynamic Model

For the steady wind cases (all but the real wind simulations), the hydrodynamic model runs were set up to run for a period of four days with a time step of 30 min. A ramp time of 24 hrs was used to bring the model smoothly to full influence of the forcing conditions and minimize spurious model responses. The wind input to the model is applied as a spatially invariant wind field at a constant wind speed and direction (differing by case) for all but the real wind cases. This means that the water surface at each location on the model grid experiences an identical wind stress (i.e. no cyclones or "puffs" are modeled). The wind field is likewise spatially invariant for the real wind cases but the speed and direction are allowed to change with time. River flow input to the bay is also constant over the period of the simulation.

As the wind and river flow forces are applied to the bay (including the Northeast Arm) the model calculates the change in the current patterns and the surface elevation over time. Five layers were used in the vertical direction to represent the vertical structure of the currents, (e.g. the currents at the surface may be going one way while the bottom currents go in the opposite direction). Once the currents and surface elevation attained a steady state, (for all but the real wind cases) the currents on all five layers and the surface elevation were stored for use in the flushing, sediment and phosphorus models. For the real wind simulations the currents and surface elevations were stored at two hour intervals for the entire forty day period.

4.2 Flushing Model

For the flushing application, the constituent transport model was configured to simulate the advection and diffusion of a conservative constituent (i.e. no decay, no settling, no reaction) to determine the flushing time under different environmental forcing conditions and bridge geometries. For the remainder of this report we will refer to the single constituent transport model as the flushing model when employed in the flushing calculations.

The flushing model was initialized with a concentration of the conservative constituent of 1 mg/L everywhere. The physical equivalent of this initial condition can be envisioned as the concentration of some extremely fine particulate matter in the water as a result of bottom material resuspension after the passage of a large storm

event. The simulation is then used predict the time required to clear the bay of the suspended material without settling any of it to the bottom. To accomplish this the model was run for a period of 40 days to track the length of time required for the concentrations to drop toward zero. The material concentration in the river input for these simulations was zero, so no new material was added to the bay after initialization. Analyzing the volume weighted time rate of change of concentration in the bay then provides an estimate of the flushing time for Missisquoi Bay.

4.3 Sediment Transport Model

For the sediment transport simulations the constituent transport model was configured with a settling term, at various rates, to simulate the settling out and sediment deposition of various sized particles. The distribution of sediments on the lake bottom suggest that suspended sediments in the tributaries that make it into the lake range from fine sand and silt to clay (section 2.3). It is apparent that even the very fine sand (particle diameter on the order of 62.5μm to 100μm) settles out very quickly near the mouth of the river. To study the effect that the causeway might have on suspended material emanating from the river we chose therefore to concentrate on particles of the size of very fine silt or clay. These particles have diameters in the range of 1μm to 10μm. The various particle sizes are simulated in the model by adjusting the bulk constituent settling velocity. One particle size is modeled at a time. Stokes' Law, for terminal gravitational settling of a sphere based on its diameter and density, was used to determine the settling rate for each particle size, (Davis, 1983). A median value for the material settling rate of 0.2 m/day (corresponding to clay) was chosen, with a range determined by halving and doubling that rate. It is clear from Figures 2.6 and 2.7 that clay forms a substantial fraction of the sedimentary material in the bay. The likely source of that material is the rivers. The figures also indicate that clay does not settle out near the mouth of the rivers but rather is transported farther into the bay (or out of the bay) were it may be deposited, as seen from the distribution.

For each sediment transport simulation the bay was initially assumed to be completely free of suspended sediments in the water column. It was also assumed that no sediments would be re-suspended for the simulations, (which the low predicted

current speeds justify in the absence of waves). The rivers therefore are the only source of sediment to the water column in the bay.

For each layer in a water grid cell, a certain mass of material is determined to settle (fall) into the layer below at a rate proportional to the settling velocity and material concentration. For the bottom layer the calculated mass settles out, into the sediments. TSS concentrations of 30 (mg/L) for the Missisquoi River, 30 (mg/L) for the Rock and 30 (mg/L) for the Pike were used. The total load to the bay was determined by multiplying the concentration times the flow rate for each of the rivers respectively.

4.4 Phosphorus Model

The phosphorus simulations were done using the single constituent transport model configured with a first order loss term (decay rate). Based on the values determined from the Long Term Monitoring Study Of Lake Champlain (VTDEC & NYSDEC, 1994) concentrations of phosphorus were initialized to an average of 35 µg/L in Missisquoi Bay and 14 µg/L in the Northeast Arm. River input concentrations were also derived from that study as follows: Phosphorus concentrations of 63.5 µg/L for the Missisquoi River, 401 µg/L for the Rock and 169 µg/L for the Pike were used. The total load to the bay was determined by multiplying the concentration times the flow rate for each of the rivers respectively.

5. MATRIX OF MODEL RUNS

A matrix of model runs was developed and executed to evaluate how the model predicted currents of Missisquoi Bay responded to various environmental forcing conditions (winds and river flow) and causeway geometries. The predicted circulation for each case was then used to drive the flushing and sediment transport models to evaluate the ultimate effect the variables had on the flushing time and sediment deposition in the bay. A summary description of each of the environmental parameters varied in the Case Matrix is shown in Table 5.1. The matrix of cases is given in Table 5.2.

The geometry of the causeway and the neighboring rail trestle are considered first. The highway causeway geometries included no causeways, partial causeways and full causeways (the present condition). The railroad trestle configuration was simply with and without the influence of the trestle pilings. The trestle pilings were assumed to decrease the effective flow area by approximately 10% on the west side of the Missisquoi Bay entrance and 20% on the east. It must be noted that these reductions are simple estimations based on observations of material forming the structure of the submerged portion of the trestle. The east side appeared to contain more submerged rip-rap than the west.

The predominant wind directions used were south southwest and west, based on the analysis of the Philipsburg weather station data presented in Section 2. Wind speeds included 5, 10, 20 and 30 mph (2.2, 4.5, 8.9 and 13.4 m/s). A real wind case (ie

a time varying wind field) was also developed which includes a typical spring storm with maximum winds of 52 mph (23.4 m/s). After preliminary investigations the wind

Table 5.1 Description of the environmental parameter values in the Case Matrix.

1. Causeway configuration

1.1) Present configuration
1.2) Center passage expanded (50% of causeway removed from each side)
1.3) 25% of causeway removed from each shore
1.4) Causeway removed completely

2. Wind direction

2.1) N wind
2.2) NE wind
2.3) E wind
2.4) SE wind
2.5) S wind, the predominant direction (SSW)
2.6) SW wind
2.7) W wind
2.8) NW wind, secondary predominant direction
2.9) No wind

3. Wind speed

3.1) 5 mph
3.2) 10 mph
3.3) 15 mph
3.4) 20 mph
3.5) 30 mph

4. Lake level

4.1) low lake level: 93 feet, referred to NGVD 1929
4.2) mean lake level: 95.8 feet, (mean stage 1900-1987)
4.3) high lake level: 100 feet

5. River flow

5.1) high flow at high lake level (spring runoff conditions)
5.2) low flow at mean lake level (normal summer conditions)
5.3) high flow at mean lake level (summer/fall storm condition)
5.4) no river flow

6. Railroad trestle configuration

6.1) with trestle present
6.2) without trestle

7. Real wind case

7.1) typical spring winds (including storm winds)
7.2) typical fall winds, (including storm winds)

FINAL MATRIX
03/20/96

MISSISQUOI BAY MODEL SIMULATION MATRIX

Variable Description			Simulation designation																																			
			B1	B2	1	2	3	4	5	6	7	8	9	10	11	12	13	14	15	16	17	18	19	20	21	22	23	24	25	26	27	28	29	30	31	32	33
Model Used	Hydrodynamic		X	X	X	X	X	X	X	X	X	X	X	X	X	X	X	X	X	X	X	X	X	X	X	X	X	X	X	X	X	X	X	X	X		
	Flushing		X	X	X	X	X	X	X	X	X	X	X	X	X	X	X	X	X	X	X	X	X	X	X	X	X	X	X	X	X	X	X	X	X	X	X
	Sediment Transport		X	X	X	X			X	X	X		X			X	X			X	X	X	X	X	X	X	X	X	X	X	X	X	X	X	X	X	X
	Phosphorus		X	X												X	X																				
Causeway Config:	Present configuratio	1.1	X		X		X		X							X				X		X		X		X		X		X		X		X	X	X	
	Center 50% remove	1.2																X																			
	25% each shore	1.3																																			
	Completely removed	1.4		X		X		X		X	X	X	X				X				X		X		X		X		X		X		X				X
Wind Direction:	North	2.1																		X	X																
	North East	2.2																				X	X														
	East	2.3																						X	X												
	South East	2.4																								X	X										
	South (SSW)	2.5	X	X			X	X	X	X	X	X	X	X	X																			X	X		
	South West	2.6																										X	X								
	West	2.7			X	X																															
	North West	2.8																												X	X						
	no wind	2.9																														X	X			X	X
Wind Speed:	5 mph	3.1									X																							X			
	10 mph	3.2	X	X	X	X						X	X	X	X					X	X	X	X	X	X	X	X	X	X	X	X				X		
	15 mph	3.3																																			
	20 mph	3.4																																			
	30 mph	3.5							X	X																											
Lake Level:	Low lake level (93')	4.1																																			
	Mean stage (95.8')	4.2	X	X	X	X	X	X	X	X	X	X	X	X	X					X	X	X	X	X	X	X	X	X	X	X	X	X	X	X	X	X	X
	High lake level (100')	4.3														X	X																				
River Flow:	High flow (spring)	5.1	X	X	X	X	X	X	X	X	X					X	X			X	X	X	X	X	X	X	X	X	X	X	X	X	X	X			
	Low flow (summer)	5.2										X																							X		
	High flow (sum/fall)	5.3																																			
	no river flow	5.4																																		X	X
Trestle config:	with trestle	6.1	X	X	X	X	X	X	X	X	X	X	X	X	X	X	X	X	X	X	X	X	X	X	X	X	X	X	X	X	X	X	X	X	X	X	X
	without trestle	6.2																																			
Real Wind Case:	Spring	7.1														X	X																				
	Fall	7.2																																			

Table 5.2 Matrix of model simulations.

MISSISQUOI BAY MODEL SIMULATION MATRIX CASE DESCRIPTION

B = Base case definition
South-southwest wind
@ 10 mph
Mean lake level (95.8')
High river flow
Railroad trestle present

Case description
B1 - Base case with present causeway configuration
B2 - Base case with the causeway completely removed
1 - Wind direction variation test (west) with causeway
2 - Wind direction variation test (west) without causeway
3 - Wind speed variation test (15 mph) with causeway
4 - Wind speed variation test (15 mph) without causeway
5 - Wind speed variation test (30 mph) with causeway
6 - Wind speed variation test (30 mph) without causeway
7 - Low wind speed test (5 mph) without causeway
8 - Lake level variation test (high lake level) without causeway
9 - River flow variation test (low flow) without causeway
10 - Railroad trestle variation test (trestle not present) with causeway
11 - Railroad trestle variation test (trestle not present) without causeway
12 - Real wind forcing (variable winds - typical spring conditions) with causeway
13 - Real wind forcing (variable winds - typical spring conditions) without causeway
14 - Causeway removal configuration test (center removed)
15 - Causeway removal configuration test (50% from each side removed)
16 - Wind direction variation test (north) with causeway
17 - Wind direction variation test (north) without causeway
18 - Wind direction variation test (north east) with causeway
19 - Wind direction variation test (north east) without causeway
20 - Wind direction variation test (east) with causeway
21 - Wind direction variation test (east) without causeway
22 - Wind direction variation test (south east) with causeway
23 - Wind direction variation test (south east) without causeway
24 - Wind direction variation test (south west) with causeway
25 - Wind direction variation test (south west) without causeway
26 - Wind direction variation test (north west) with causeway
27 - Wind direction variation test (north west) without causeway
28 - Wind direction variation test (no wind) with causeway
29 - Wind direction variation test (no wind) without causeway
30 - (7A) Low wind speed test (5 mph) with causeway
31 - (9A) River flow variation test (low flow) with causeway
32 - Diffusion only test, no river flow, no wind flow, with causeway
33 - Diffusion only test, no river flow, no wind flow, without causeway

directions for the remaining six points of the compass were included to evaluate the directional influence of the wind driven transport in the bay.

Lake level was also used as a dimension in the matrix. A mean stage of 95.8 ft (29.20 m) was used, as referred to the National Geodetic Vertical Datum of 1929 and calculated for the years between 1900 and 1987, inclusive. A high lake level of 100 ft (30.48 m) was also used.

A series of 33 simulations were run for the hydrodynamic and flushing model simulations, 28 cases for the sediment transport model and 2 cases for the phosphorus model, as shown by the designations in Table 5.2. The base case (B1) consisted of a mean (no storm) south southwest wind at 10 mph (4.5 m/s), mean lake level, high river flow, (5330 ft^3/s [150.9m^3/s] total inflow) with the highway causeway and railroad trestle present. The second base case (B2) was the same as B1 but with the highway causeway completely removed.

Simulations 1 and 2 were the same as B1 and B2, respectively, except that the steady wind came from the west, the secondary predominant direction. Simulations 3 and 4 were the same as B1 and B2, respectively, except that the wind was increased to 20 mph (8.9 m/s). Simulations 5 and 6 were the same as B1 and B2, respectively, except that the wind was increased to 30 mph (13.4 m/s). Simulation 7 was the same as B2 except that the wind was decreased to 5 mph (2.2 m/s).

Simulation 8 was the same as B2 except the lake level was high (100 ft [30.48 m]). Simulation 9 was the same as B2 except that the river flow was low (929 ft^3/s [26.3 m^3/s]).

Simulations 10 and 11 were the same as B1 and B2, respectively, except the railroad trestle was removed.

Simulations 12 and 13 were the same as B1 and B2, respectively, except real, time varying winds were used, including a typical spring storm, instead of the mean, steady-state south wind.

Simulation 14 was the same as B1 except the center 50% of the highway causeway was removed from the center. Simulation 15 was the same as B1 except 25% of the highway causeway at each shore was removed.

To fill out the 8 points of the compass, simulations 16 through 27 varied the direction of the wind to include N,NE,E,SE,SW and NW in pairs for cases with and without the causeway, respectively. All other variables were as in the base cases.

Cases 28 and 29 were run with no wind whatever (calm conditions, ie. the currents and therefore transport would be due entirely to the river flow).

Cases 30 and 31 were simulations run with the causeway present to match without causeway cases 7 and 9, the low wind and low river flow cases respectively.

Finally, cases 32 and 33 were run with the flushing and sediment transport models to simulate no currents in the bay at all (ie. no river input and no wind). This evaluates the purely diffusive exchange of material within the bay and with the Northeast Arm.

All 35 cases were run for both the hydrodynamics and the flushing simulations. Cases in the matrix that have been grayed out were found to contribute little additional information to the study after analysis of the results from the flushing study and were subsequently cut from the sediment transport model simulations.

6. MODEL RESULTS

The hydrodynamic and flushing models were first run for the first 17 cases in the simulation matrix summarized in the previous section. After preliminary analysis the remainder of the cases, 18-33 were added and the hydrodynamic and flushing models run for those cases as well. The sediment transport model was then run on 28 cases and the phosphorus model run on 2 cases as indicated. The results of the simulations and the analysis of those results follows in four sections, for the hydrodynamic, flushing, sediment transport and phosphorus models respectively.

6.1 Hydrodynamic Model

Results from the two base cases (B1 and B2) and several of the more interesting cases, that show more variability, will be presented below. These include the west wind cases, (the secondary predominant direction) with and without the causeway and the two variations on causeway removal, the 50% from the middle and 25% from each shore cases.

For comparison of the directional effect of the wind forcing on the circulation within the bay cases 16 and 20 for the wind coming from the north and from the east, respectively are included. The two cases are with the present causeway configuration. The companion cases 17 and 21, with the causeway completely removed, have been omitted as the circulation patterns generated in the bay are indistinguishable from the with causeway cases. Finally, the no wind forcing (calm conditions) case has been included for comparison.

A complete set of figures detailing the currents for each of the cases B1 through 31 can be found in Appendix C.

Case B1

The base case (B1) consisted of a mean (no storm) south southwest wind at 10 mph (4.5 m/s), mean lake level, high river flow with the highway causeway and railroad trestle present. Figure 6.1 shows the plan view of surface currents for Missisquoi Bay under case B1 conditions and Figure 6.2 shows the plan view of bottom currents. Some clear circulation patterns become apparent on inspection. In the shallow areas along both the east and west shores the surface currents are forced northward with the south-southwest wind. This is apparent in both the surface and bottom currents. In the deeper central part of the bay the currents in both the surface and bottom are affected by the recirculation flow heading towards the south-southeast. There is also a counter-clockwise circulation cell to the north of Hog Island (north of the entrance to the bay) and to the west of the Missisquoi River delta. This horizontal recirculation cell may be the mechanism by which sediments entering the bay from the Missisquoi River are carried towards the opening at the causeway.

Another interesting feature of the wind driven flow is the distinct southward flow seen at the causeway entrance. Figures 6.3 and 6.4 show a detail of the surface and bottom currents in the area around the causeway, respectively. Maximum current speeds on the order of 5 cm/s are seen in the bay and 10-15 cm/s through the causeway.

It should be noted here that the net flow out of Missisquoi Bay is due entirely to the river flow into the bay. The steady state wind circulation can contribute no net flow into or out of the bay. The wind driven circulation may contribute steady opposing flows

(ie into the bay on the edges, out of the bay in the center), but does not appear to do so in this case, (case B1).

s_s1.bmp

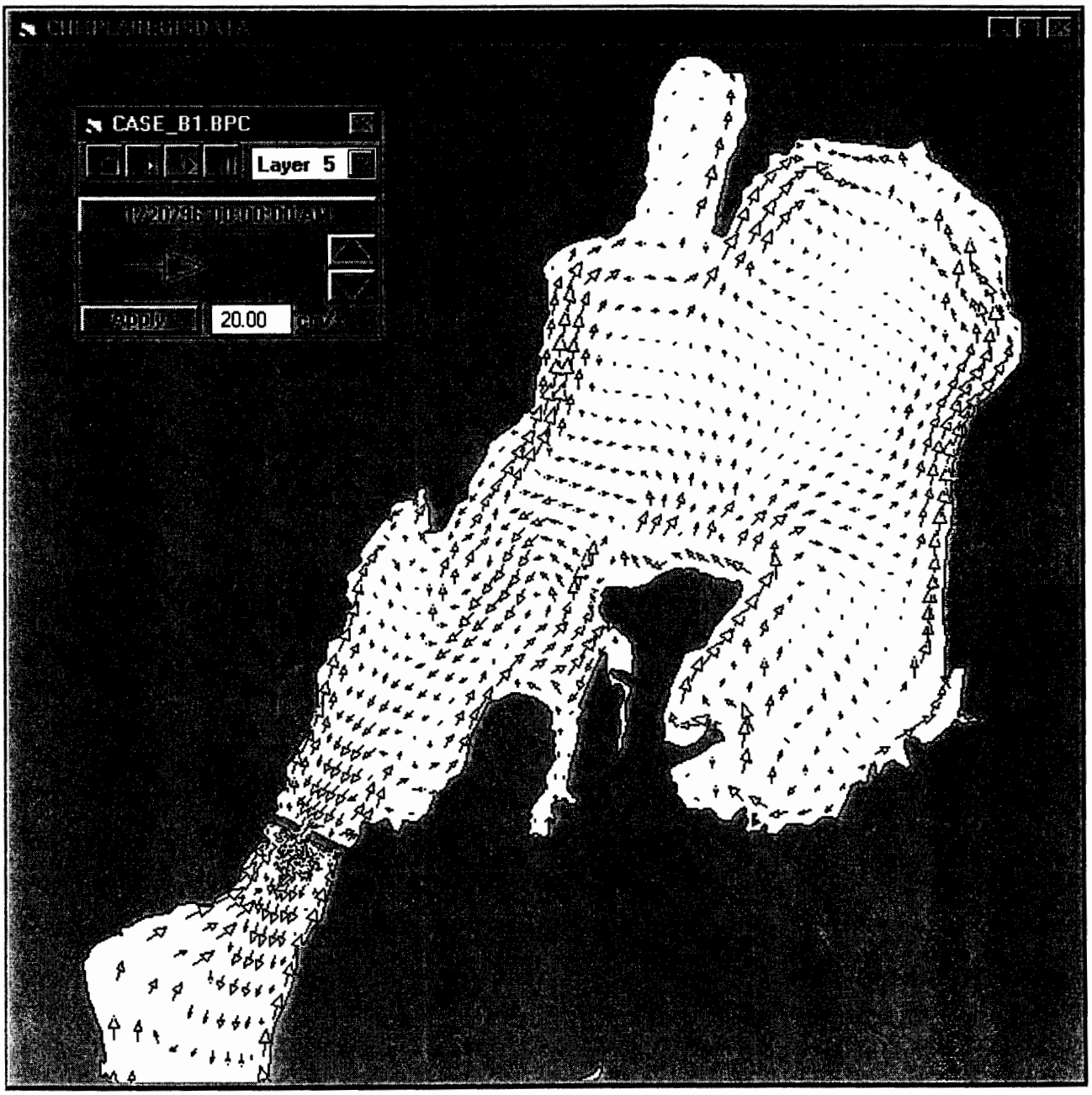

Figure 6.1 Plan view of surface currents for Case B1 (base case with present causeway configuration).

s_b1.bmp

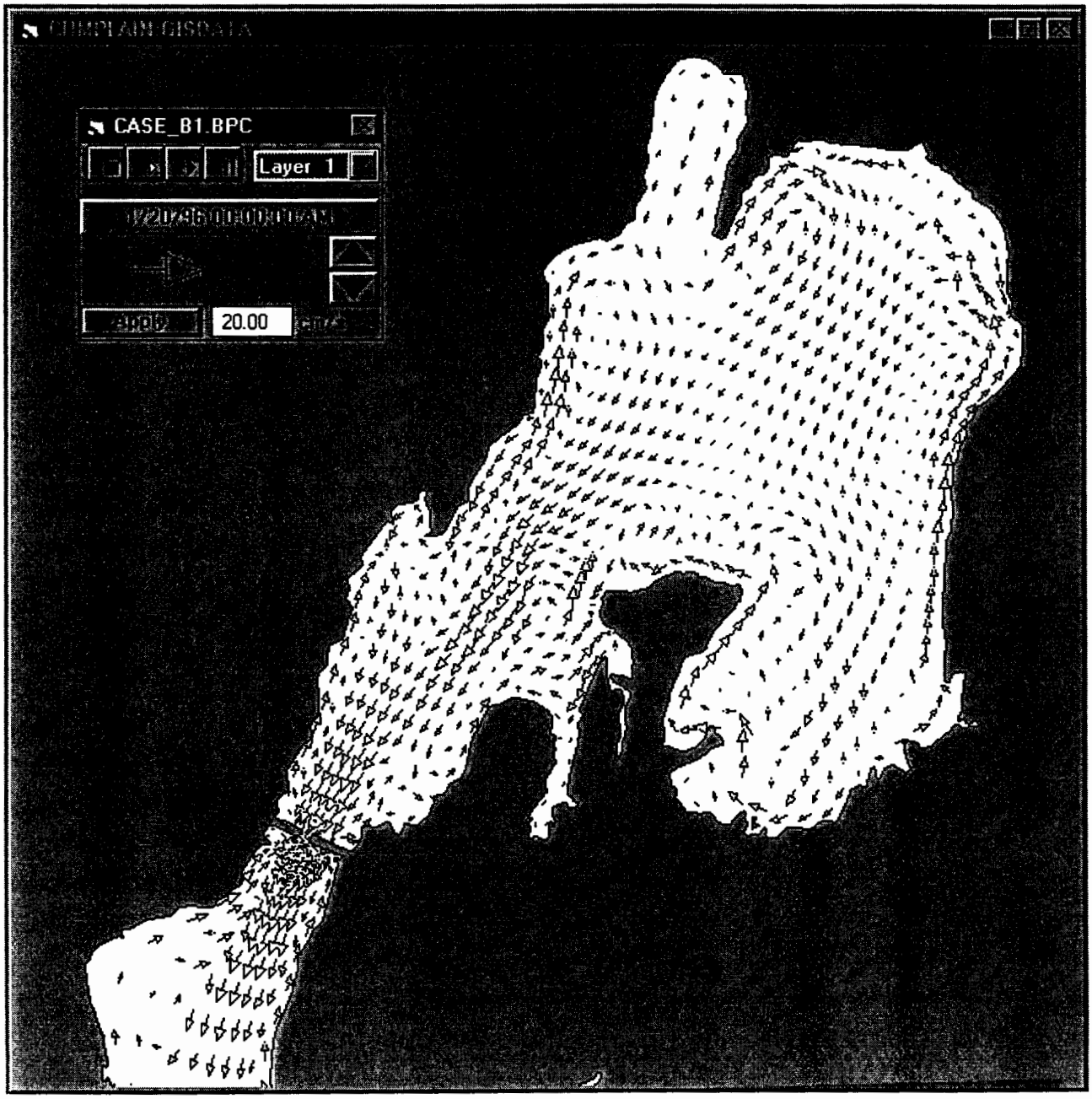

Figure 6.2 Plan view of bottom currents for Case B1 (base case with present causeway configuration).

s_s_b1.bmp

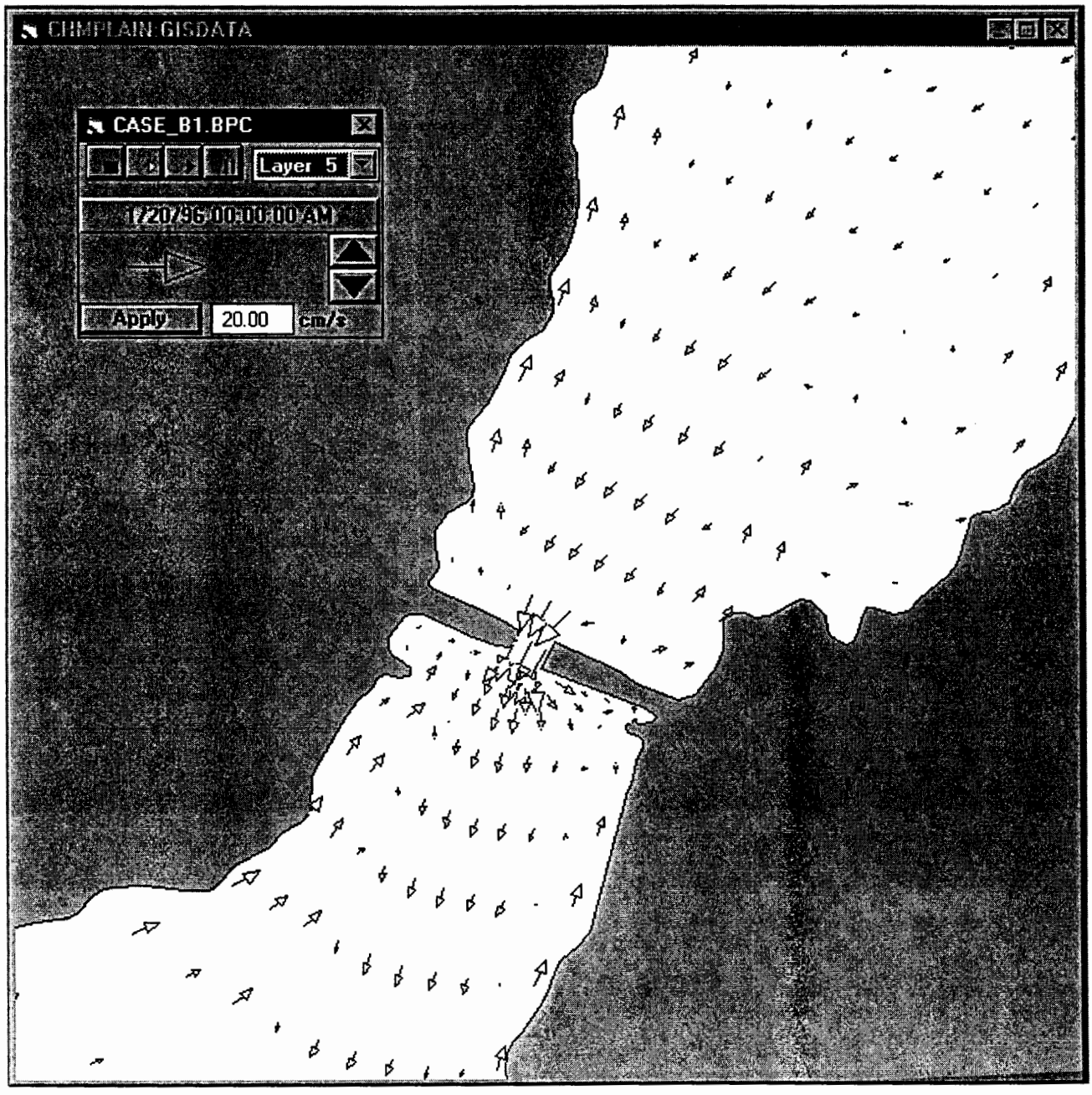

Figure 6.3 Detailed plan view of surface currents in the area near the causeway for Case B1 (base case with present causeway configuration).

s_b_b1.bmp

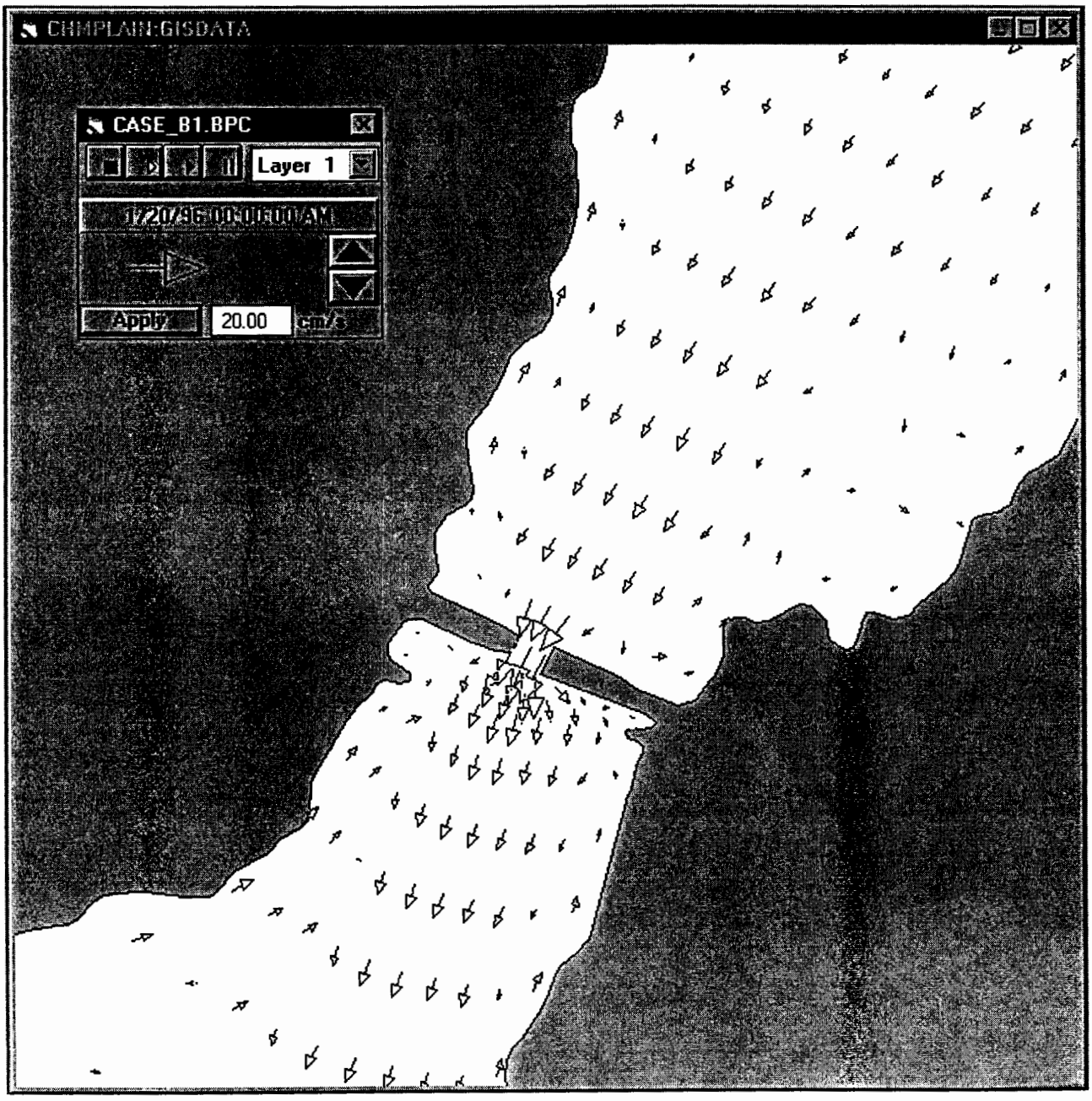

Figure 6.4 Detailed plan view of bottom currents in the area near the causeway for Case B1 (base case with present causeway configuration).

Case B2

The second base case (B2) consisted of a mean (no storm) south southwest wind at 10 mph (4.5 m/s), mean lake level, high river flow with the highway causeway completely removed but the railroad trestle present. Figure 6.5 shows the plan view of surface currents for Missisquoi Bay under these conditions. Figure 6.6 shows the plan view of the bottom currents. Upon comparison of the currents in these two figures and the currents for the 'with causeway' case (Figures 6.1 and 6.2), it is apparent that in the main part of the bay the patterns and magnitudes of the currents are nearly identical. It is not until closer inspection of the currents in the region of the causeway (Figures 6.7 and 6.8, for the surface and bottom currents, respectively) that any appreciable difference is to be noted. The model predicted surface currents show evidence of the wind driven flow in the shallow areas along each shore with the return flow in the deeper central channel portion. The bottom current pattern also displays this feature but with larger out flowing currents spread farther across the entrance. It should be noted however that in comparison with case B1, with the causeway present, the current speed here is overall reduced. The result of this relative decrease in current speed, over the larger cross-sectional area is that there is not net increase of flow through the entrance area. The maximum currents in the entrance area are on the order of 5 cm/s (compare to 10-15 cm/s with the causeway present).

Case 1

Case 1, the first variation in the case matrix, is identical in setup to case B1 except that the wind, which is at the same speed, is now from the west. The resulting current patterns for the surface and bottom are quite different than those predicted for the south-southwest wind cases, as can be seen in Figures 6.9 and 6.10, respectively. The along shore, shallow areas are now split, going to the north along the east side of the bay and south along the west. In the central portion the currents follow the wind for the most part at the surface and return, opposing the wind, at the bottom.

s_s2.bmp

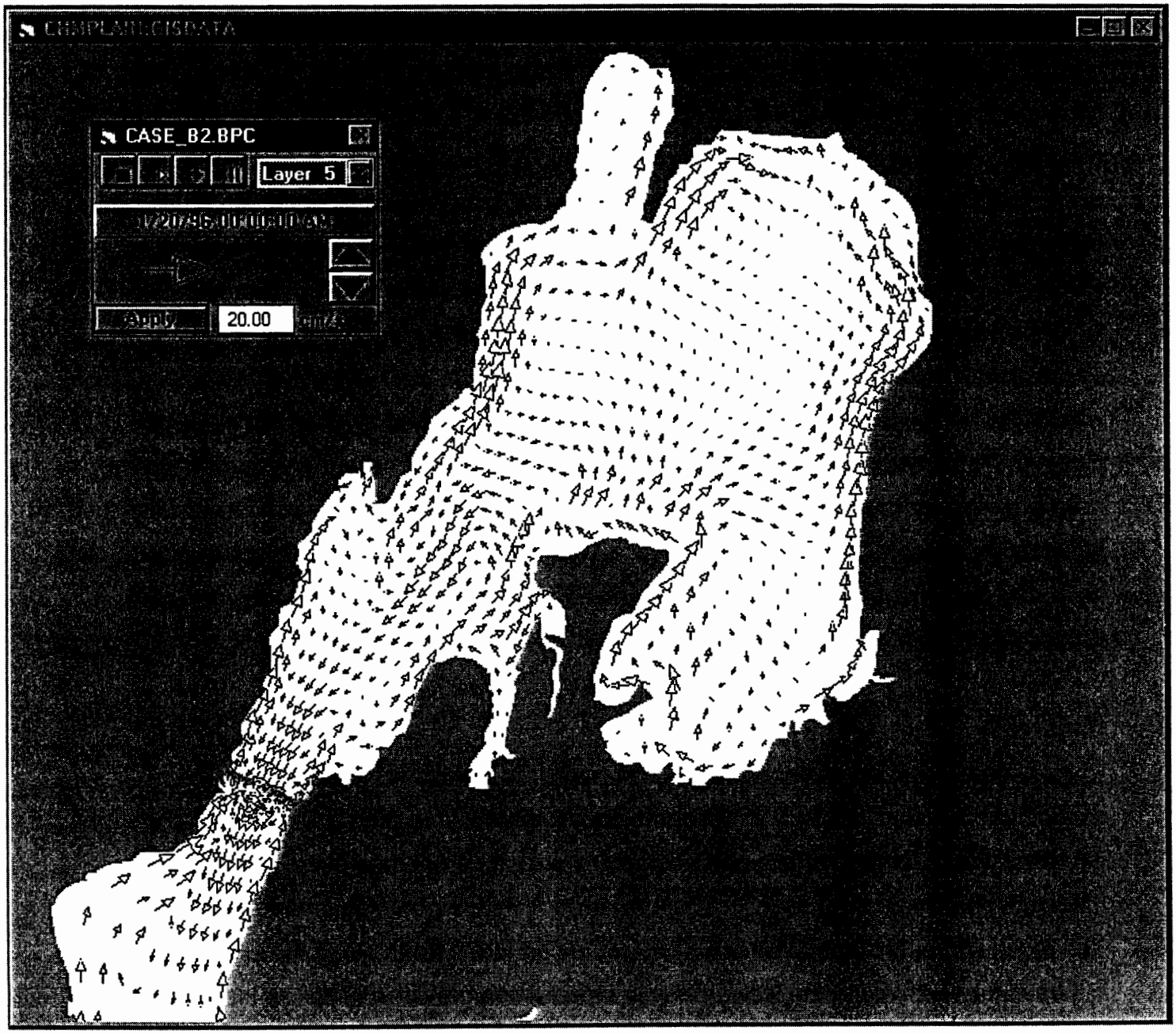

Figure 6.5 Plan view of surface currents for Case B2 (base case with the causeway completely removed).

s_b2.bmp

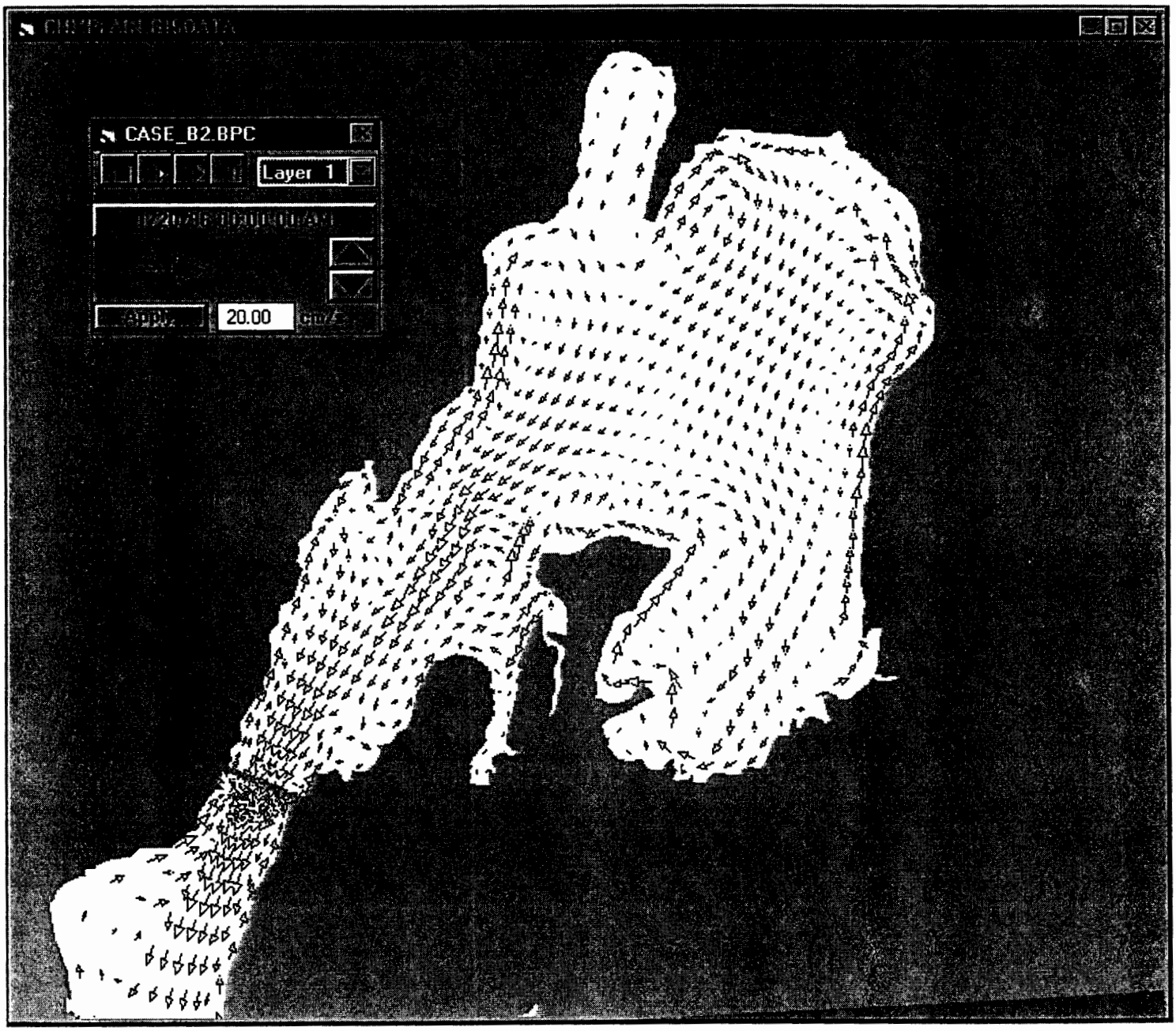

Figure 6.6 Plan view of bottom currents for Case B2 (base case with the causeway completely removed).

s_s_b2.bmp

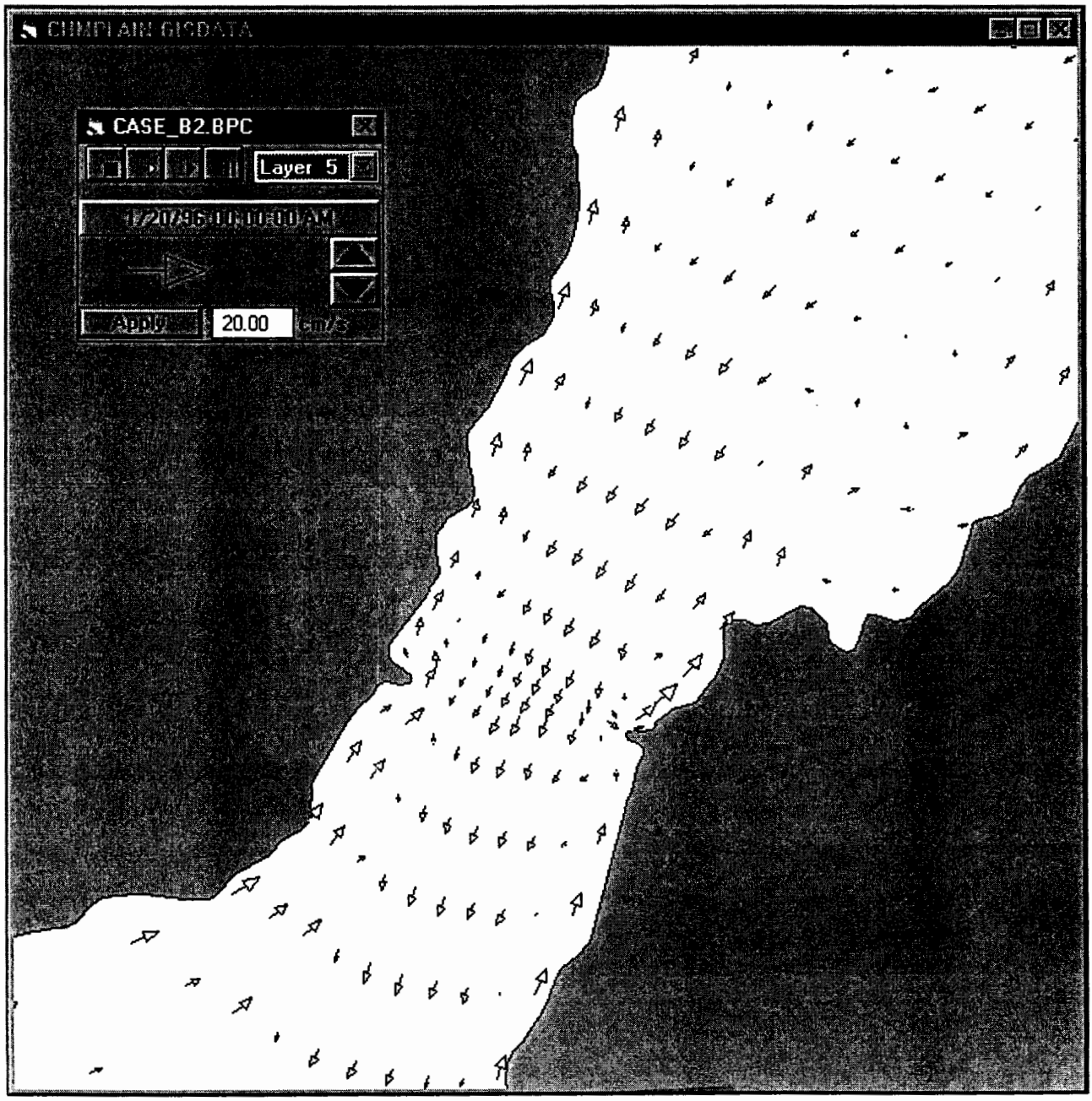

Figure 6.7 Detailed plan view of surface currents in the area near the causeway for Case B2 (base case with the causeway completely removed).

s_b_b2.bmp

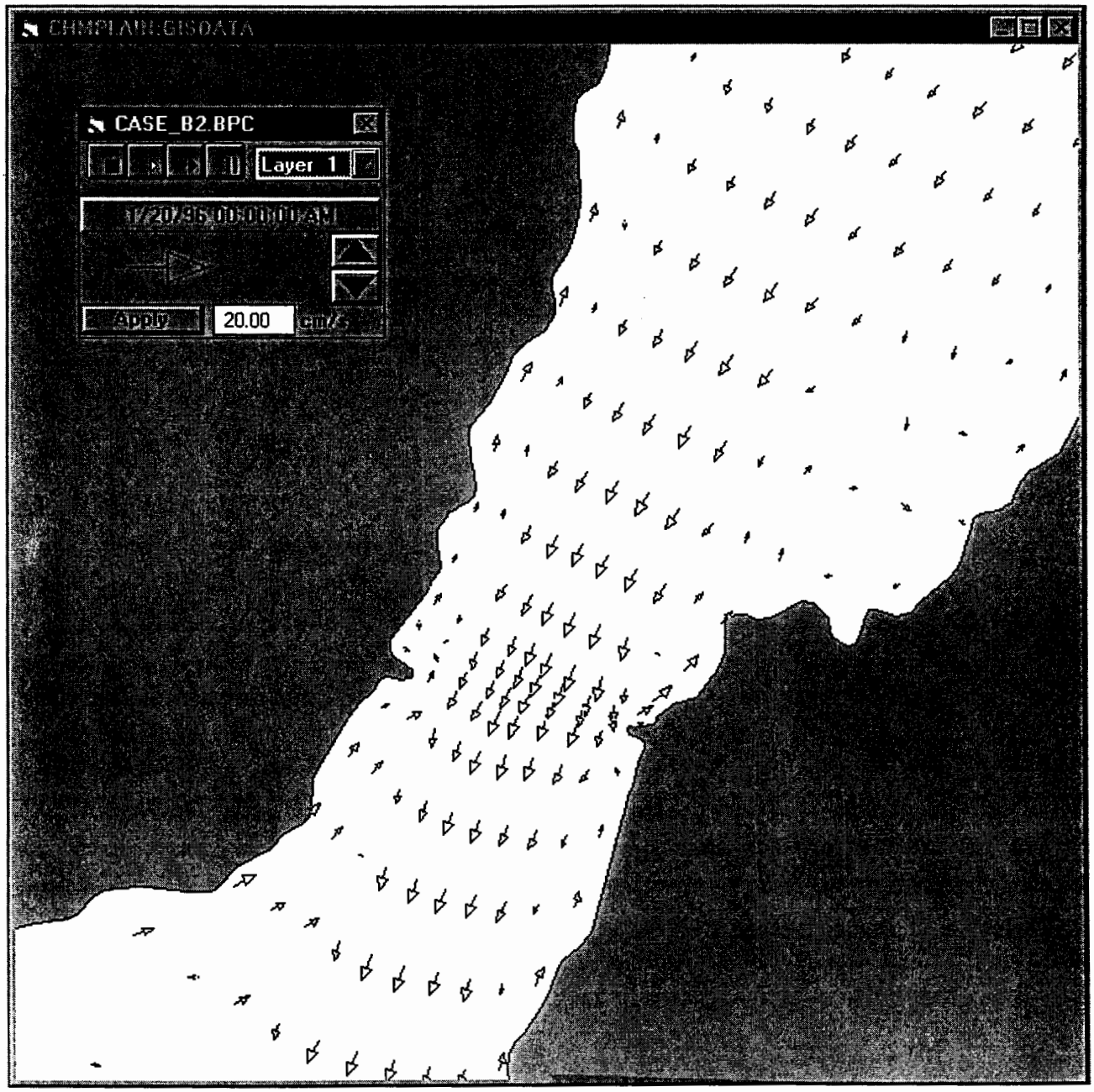

Figure 6.8 Detailed plan view of bottom currents in the area near the causeway for Case B2 (base case with the causeway completely removed).

w_s1.bmp

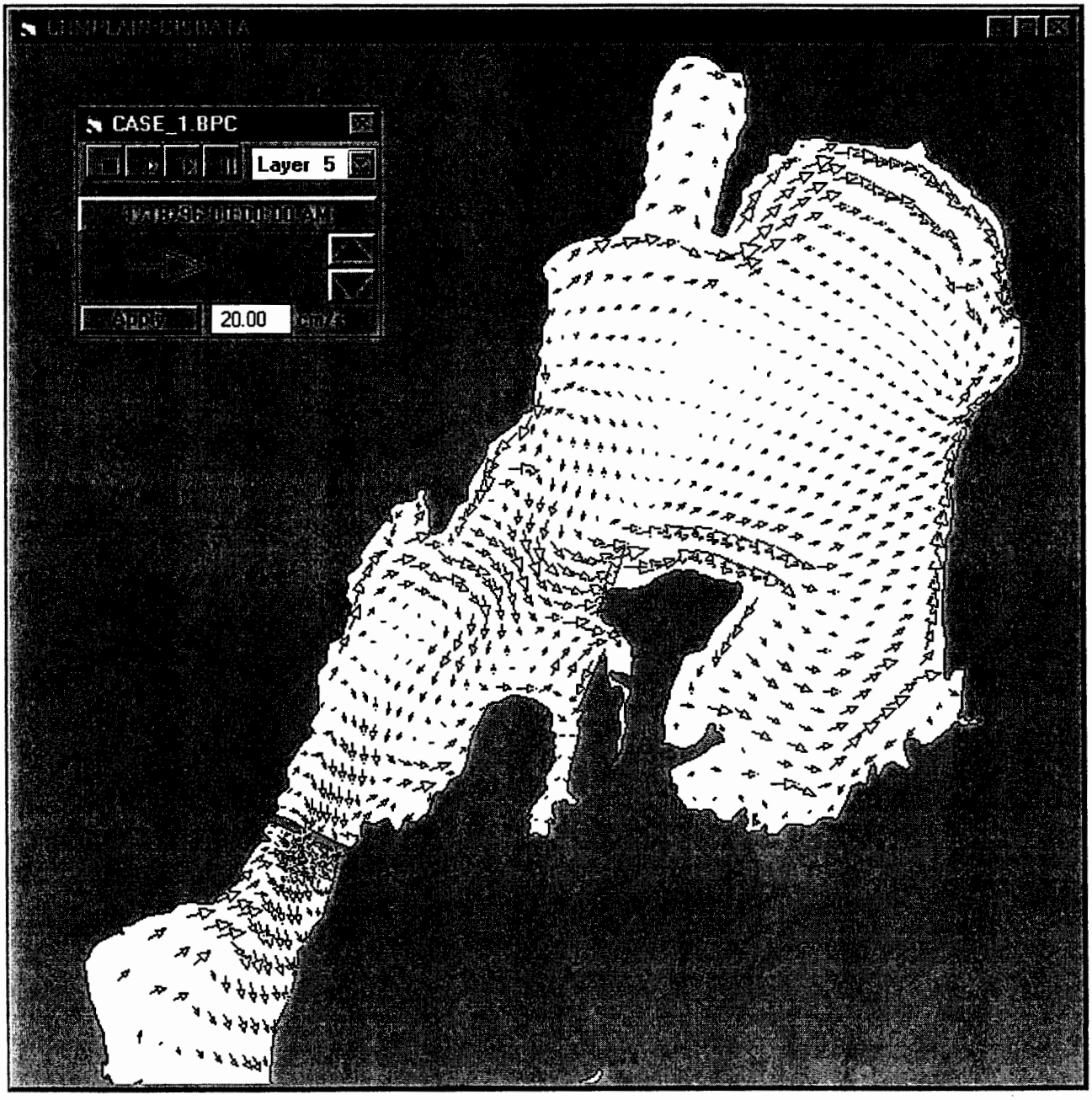

Figure 6.9 Plan view of surface currents for Case 1 (west wind with present causeway configuration).

w_b1.bmp

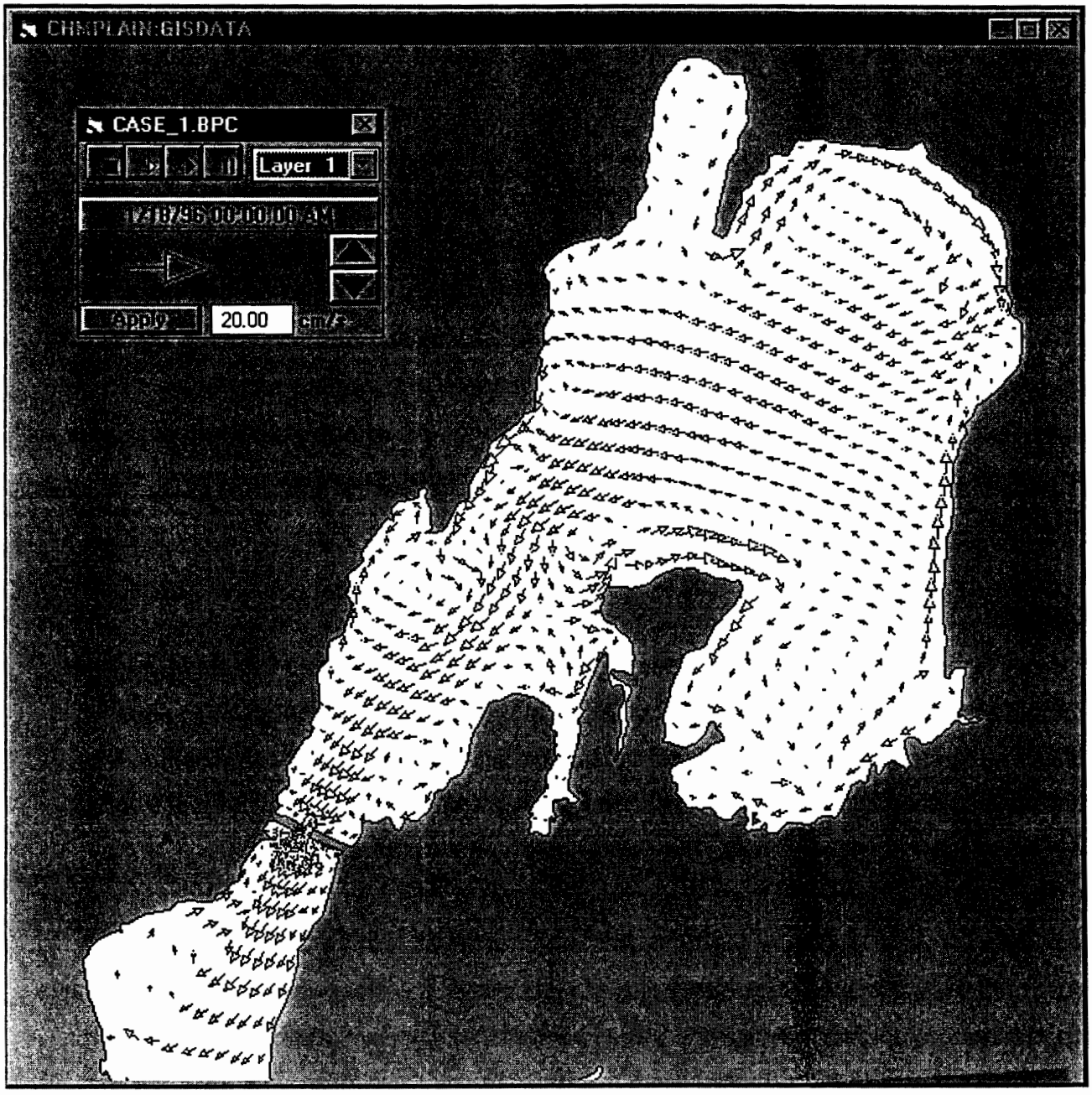

Figure 6.10 Plan view of bottom currents for Case 1 (west wind with present causeway configuration).

The current patterns near the causeway for the surface and bottom are shown in Figures 6.11 and 6.12, respectively. Again the effect of the west wind is quite apparent to the north and the south of the causeway. The flow through the causeway however is quite similar to south-southwest wind case with both the surface and bottom currents flowing out of the bay at between 10-15 cm/s.

Case 2

The specifications for case 2 are identical to case 1 except that the causeway has been completely removed. Detailed views of the currents in the entrance area to the bay, near the causeway are shown in Figures 6.13 and 6.14, respectively. Here again the current pattern is quite different than the pattern predicted for the 'with causeway', west wind case (case 1). It is also quite different than case B2, without the causeway for a south-southwest wind. As with the with and without causeway comparison for the base cases, the current speeds for the without causeway are quite a bit smaller than the with causeway case, indicating that although the patterns have changed, the net flow is equivalent.

Case 16

The circulation in the bay in response to a wind blowing from the north is shown in Figures 6.15 and 6.16 for the surface layer and bottom layer respectively. Again a different picture emerges when compared to the base case (B1). The currents in the shallower shoreline areas have a distinct southward trend along both sides of the bay. In most of the open deeper area the flow is also to the south at the surface (Figure 6.15). Along the bottom in the deeper areas however, the flow is now to the north again opposing the wind direction (Figure 6.16). An interesting feature that appears to the west of the Missisquoi River delta, north of Hog Island is a clockwise circulation cell. It is interesting to compare this with the base case (south wind) which shows a counter-clockwise circulation pattern (Figures 6.1 and 6.2).

w_s_1.bmp

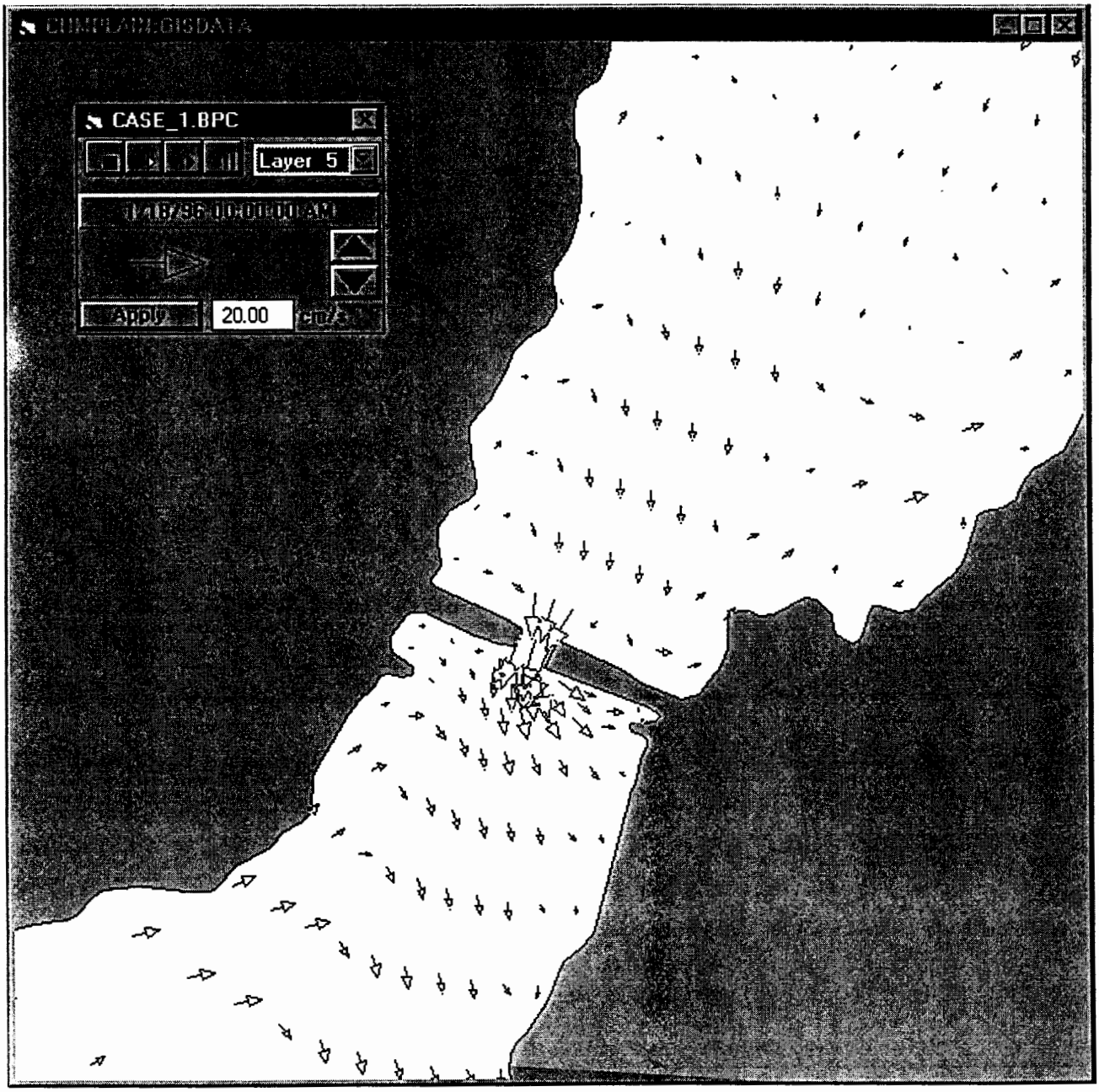

Figure 6.11 Detailed plan view of surface currents in the area near the causeway for Case 1 (west wind with present causeway configuration).

w_b_1.bmp

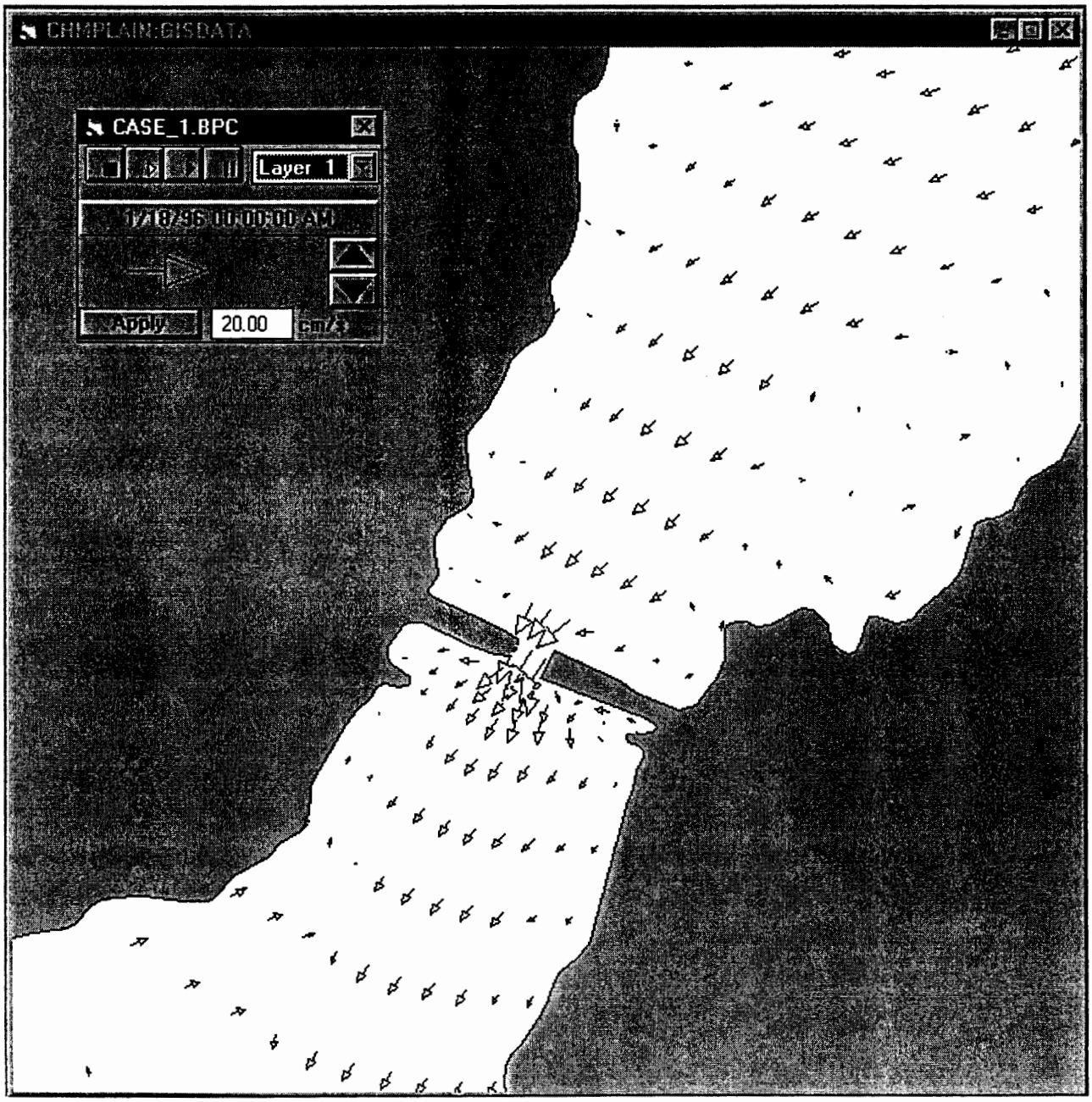

Figure 6.12 Detailed plan view of bottom currents in the area near the causeway for Case 1 (west wind with present causeway configuration).

w_2_2.bmp

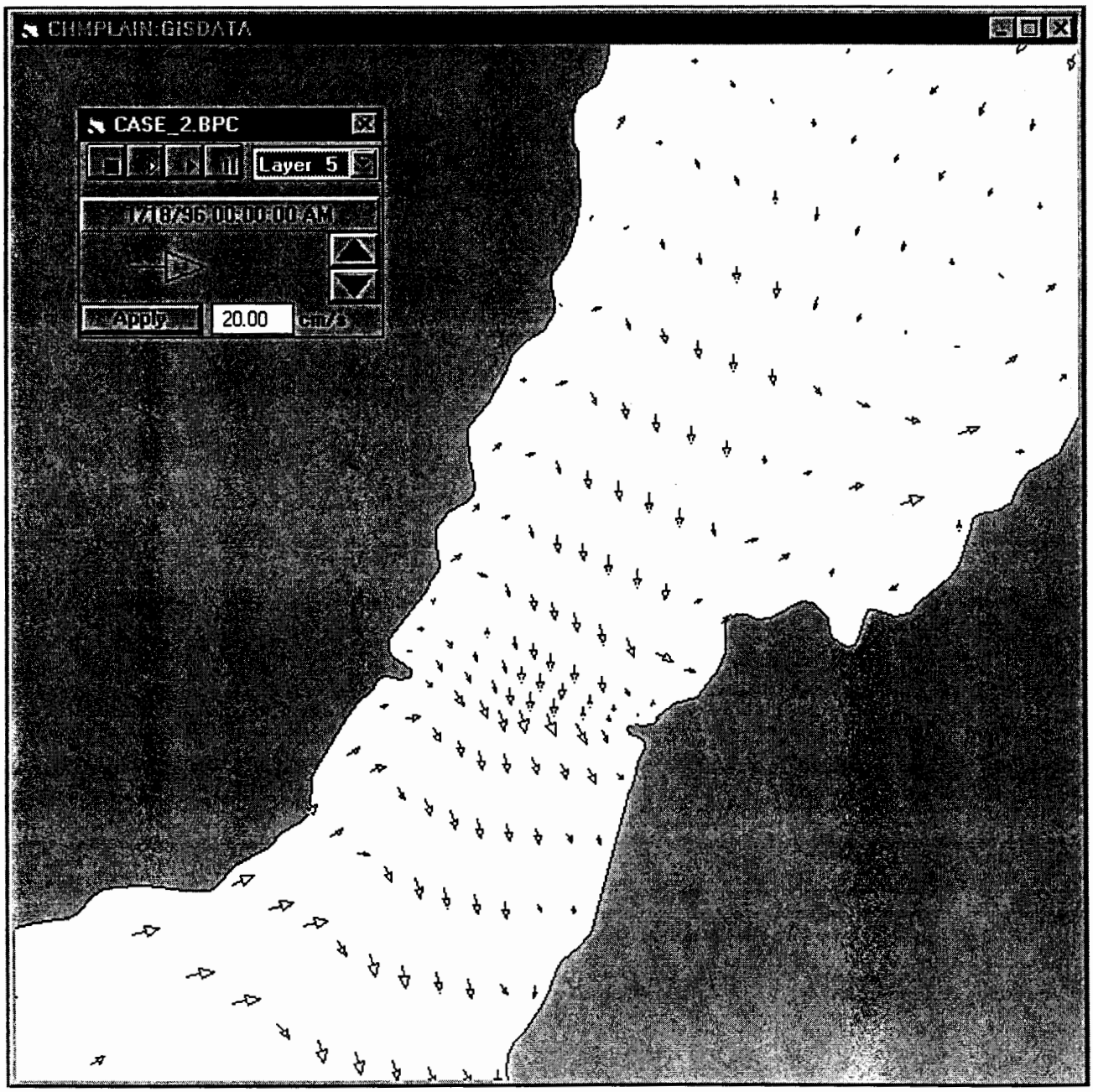

Figure 6.13 Detailed plan view of surface currents in the area near the causeway for Case 2 (west wind with the causeway completely removed).

w_b_2.bmp

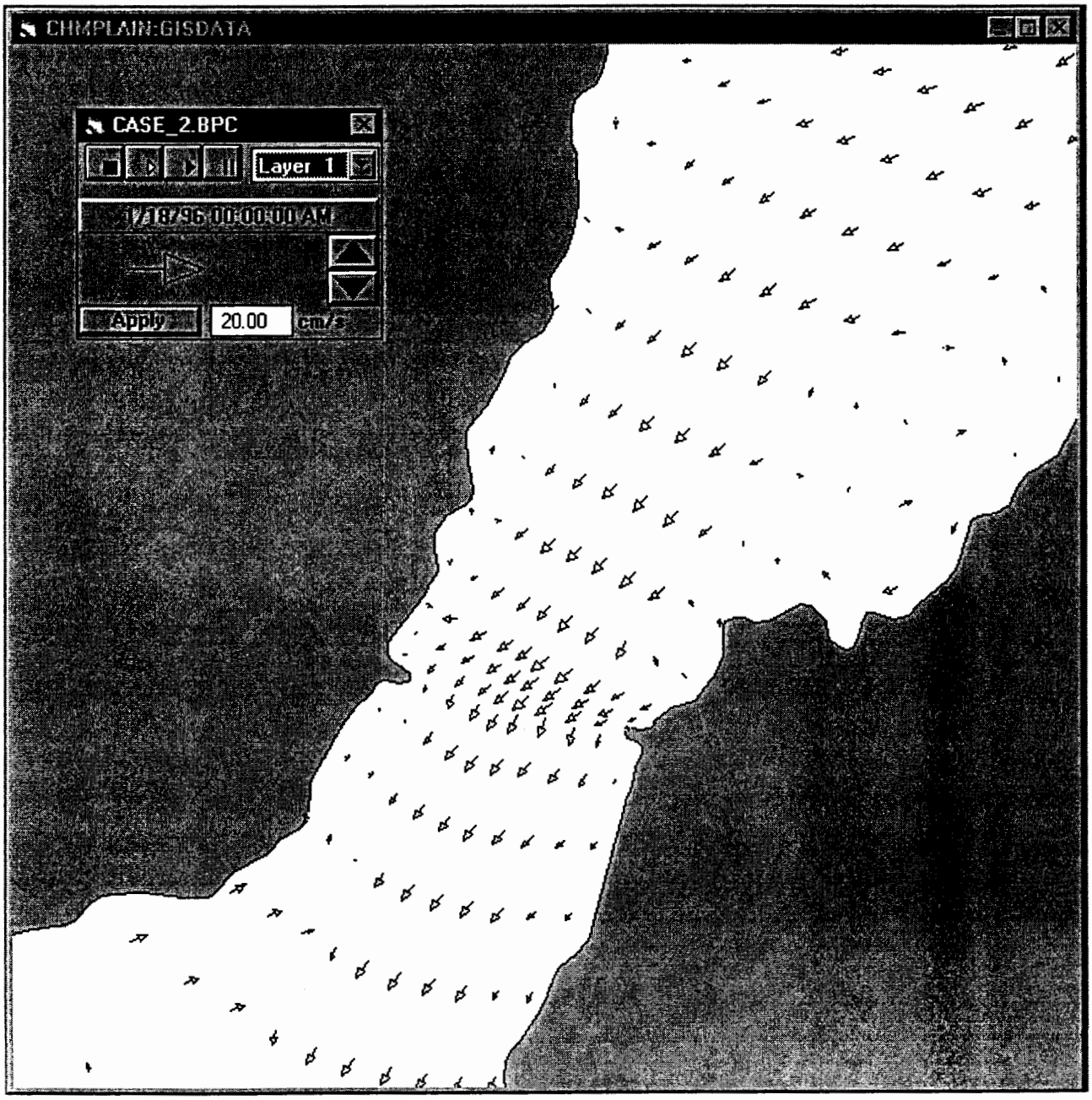

Figure 6.14 Detailed plan view of bottom currents in the area near the causeway for Case 2 (west wind with the causeway completely removed).

n_s1.bmp

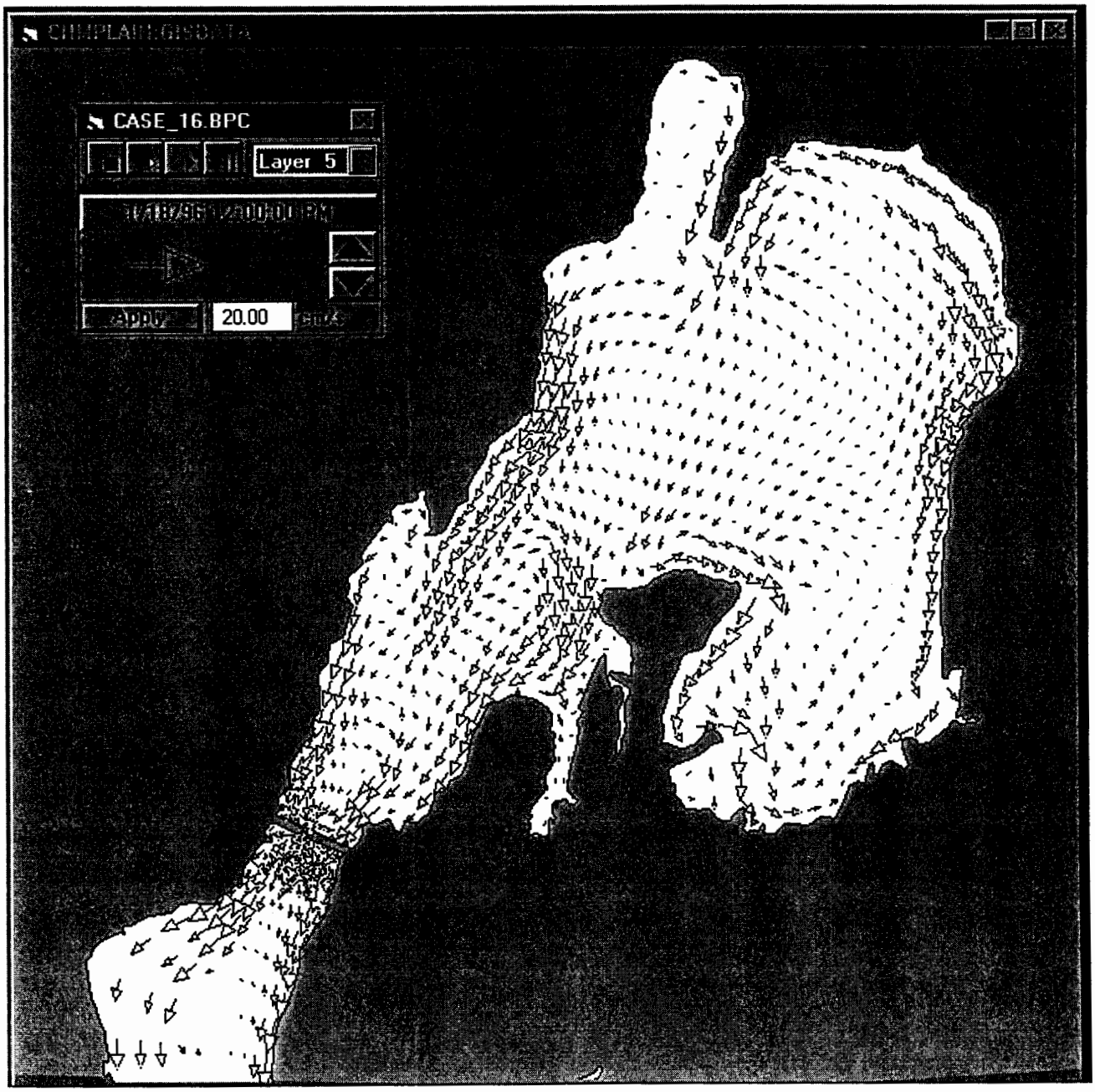

Figure 6.15 Plan view of surface currents for Case 16 (north wind with present causeway configuration).

n_b1.bmp

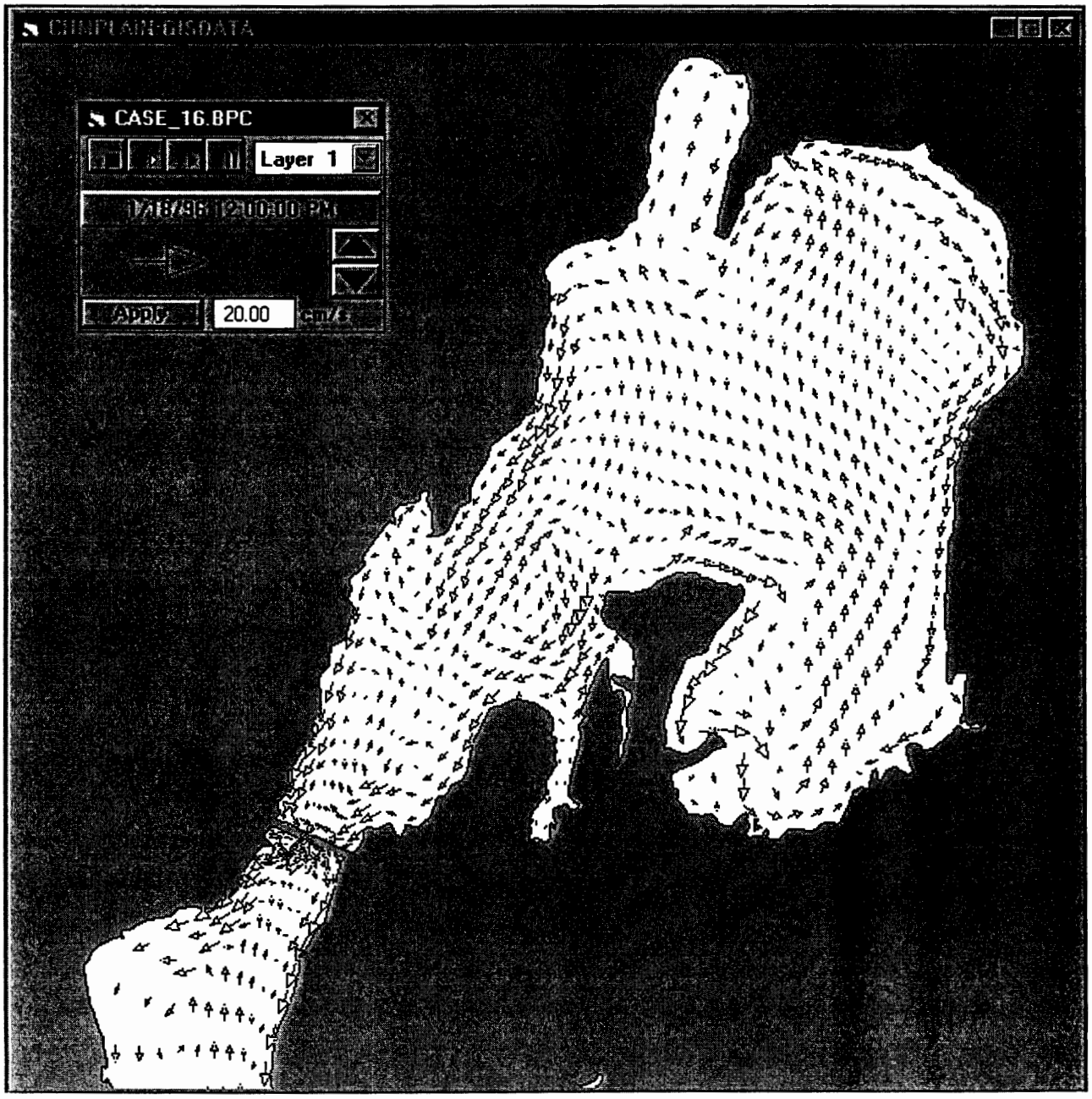

Figure 6.16 Plan view of bottom currents for Case 16 (north wind with present causeway configuration).

Case 20

The east wind forcing response (case 20) presents an almost mirror image of the west wind response in the bay. Figures 6.17 and 6.18 show the surface and bottom currents respectively. The greatest differences between the east and west wind cases again occur in the area north of the causeway and south of Chapman Bay. Here a strong surface flow to the south on both the east and west shores is visible. Surface and bottom, in the east wind case where a strong bottom flow down the center is present in the west wind case (Figure 6.10).

Case 28

As a point of reference case 28, in which no wind forcing was applied, has been included. This is equivalent to calm wind conditions, which prevailed nearly 22% of the time between 1976 and 1995 according to the Philipsburg meteorologic data (Figure 2.1). For this case the surface and bottom currents are identical and thus the surface layer only is shown in Figures 6.19 and 6.20 for the whole bay and as a close up of the causeway area, respectively. Both Figures 6.19 and 6.20 show a steady, even flow pattern of currents headed out of the bay in almost uniform strength across the inlet area west of Hog Island. It should be noted that the magnitude of the currents through the causeway opening itself is of the same order as the current magnitude for the wind driven cases. This highlights the fact that the net steady contribution of the flow through the causeway is attributable to the river influx to the bay and not to the wind driven components.

Other Cases

The process for the other cases was identical to that described for cases B1,B2, etc. described above. Although the currents varied in magnitude, for the high wind cases for example, the patterns were not substantially different.

As a matter of interest, detailed plan views of surface and bottom current patters near the causeway for the partial causeway removal cases, (cases 14 and 15) are shown in Figures 6.21-6.24. Figures 6.21 and 6.22 show the surface and bottom currents for the case with 50% of the causeway removed from the central section,

e_s1.bmp

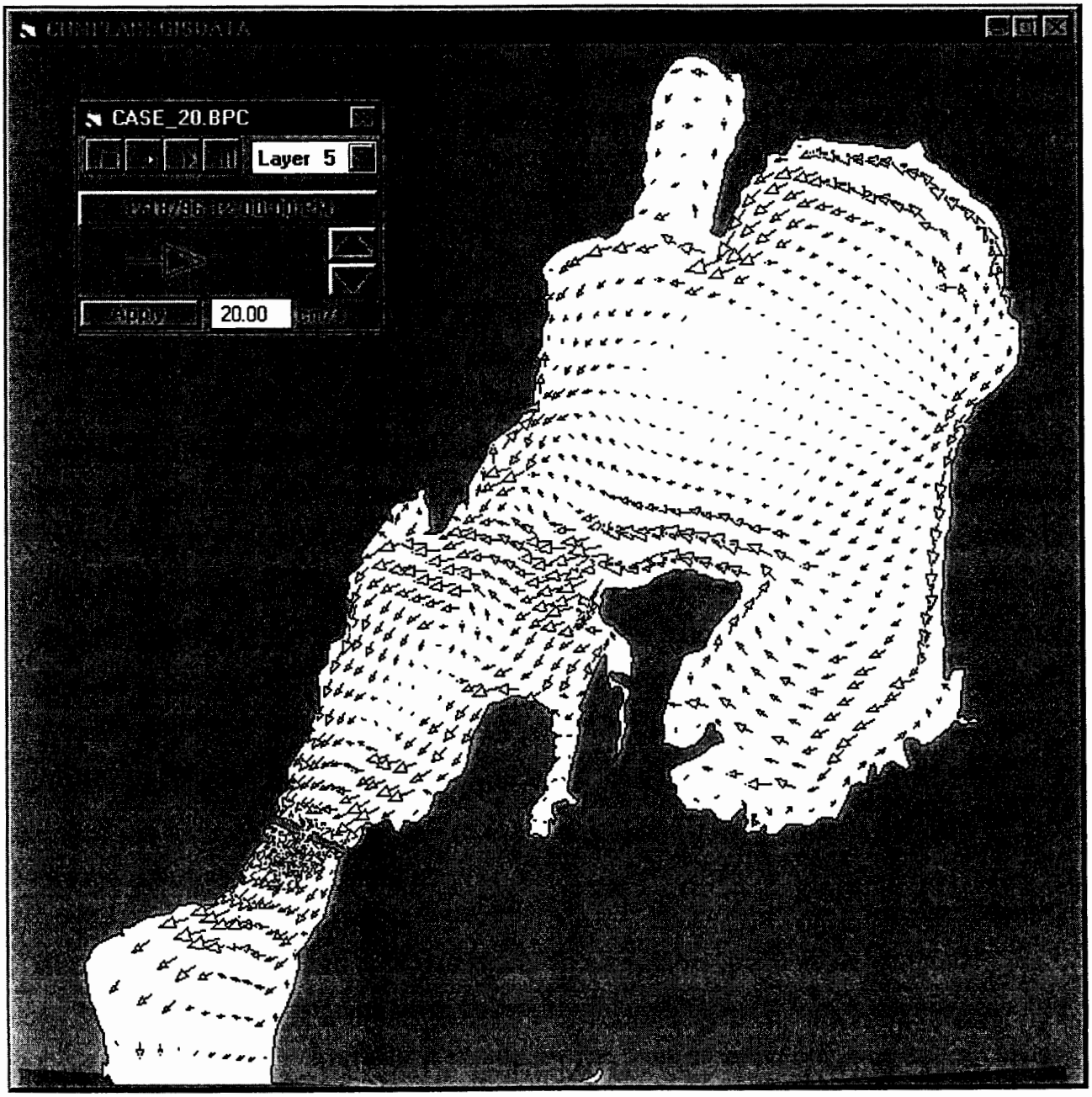

Figure 6.17 Plan view of surface currents for Case 20 (east wind with present causeway configuration).

respectively. Figures 6.23 and 6.24 show the surface and bottom currents for case 15, with 25% of the causeway removed from each shore. Each current pattern shows features easily identified with their respective causeway configurations.

6.2 Flushing Model

Again results from the two base cases (B1 and B2) and several of the more interesting cases will be presented below. These include the west wind direction case, the northwind, east wind and no wind cases with and without the causeway. Results for all of the other cases are summarized in Table 6.1 for model predicted baywide a table of flushing times.

The model predicted baywide 'flushing times' were calculated as follows. The concentration in each grid cell was multiplied by its volume (grid cell area times level thickness, for all 5 levels) to give the mass of constituent in each grid cell. These masses were summed over all grids and the result divided by the volume of the entire bay to provide the volume weighted concentration at each model output time step. The calculated volume weighted concentration at a given time was then divided by the initial volume weighted concentration to give a normalized value (between 0 and 1). The slope of the log of normalized concentration versus time is the model predicted dilution rate or flushing rate. The inverse of the model predicted rate is equivalent to a time constant, hereafter called the flushing time for a particular simulation. For the flushing model cases run in this study the concentration ratio as a function of time was not a straight line (see Figure 6.25(b) below) indicating that several processes were contributing to the flushing of the bay which will be discussed at greater length below. The flushing time estimates were made for the period covering the first 5 days.

Case B1

Figure 6.25(a) shows the plan view of the vertically averaged water column concentrations 40 days into the simulation. As expected the concentrations are lowest near the highway causeway and where the rivers enter the bay, (the rivers were set to zero concentration for the flushing time calculations). Highest concentrations (lowest

e_b1.bmp

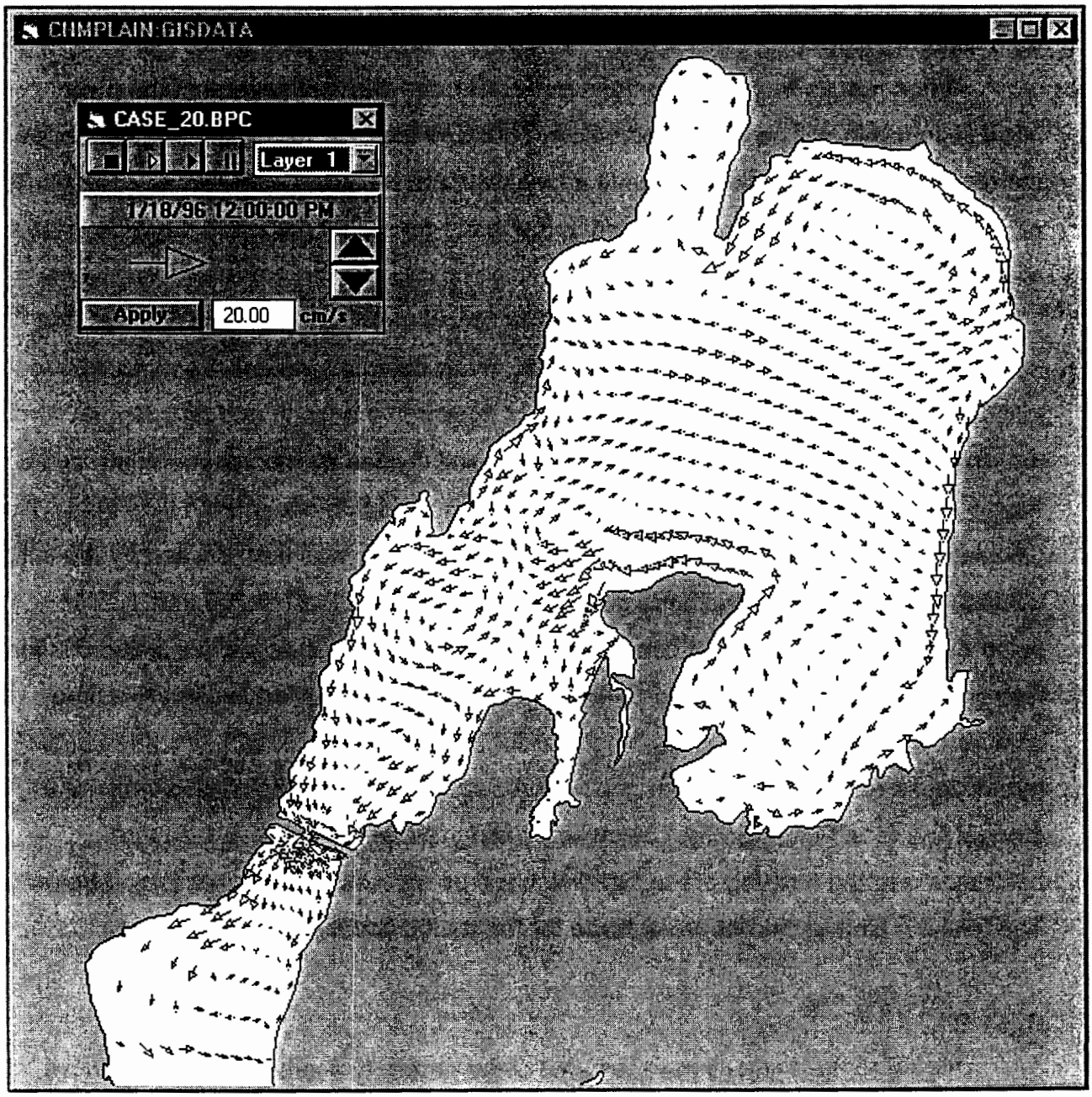

Figure 6.18 Plan view of bottom currents for Case 20 (east wind with present causeway configuration).

riv_s1.bmp

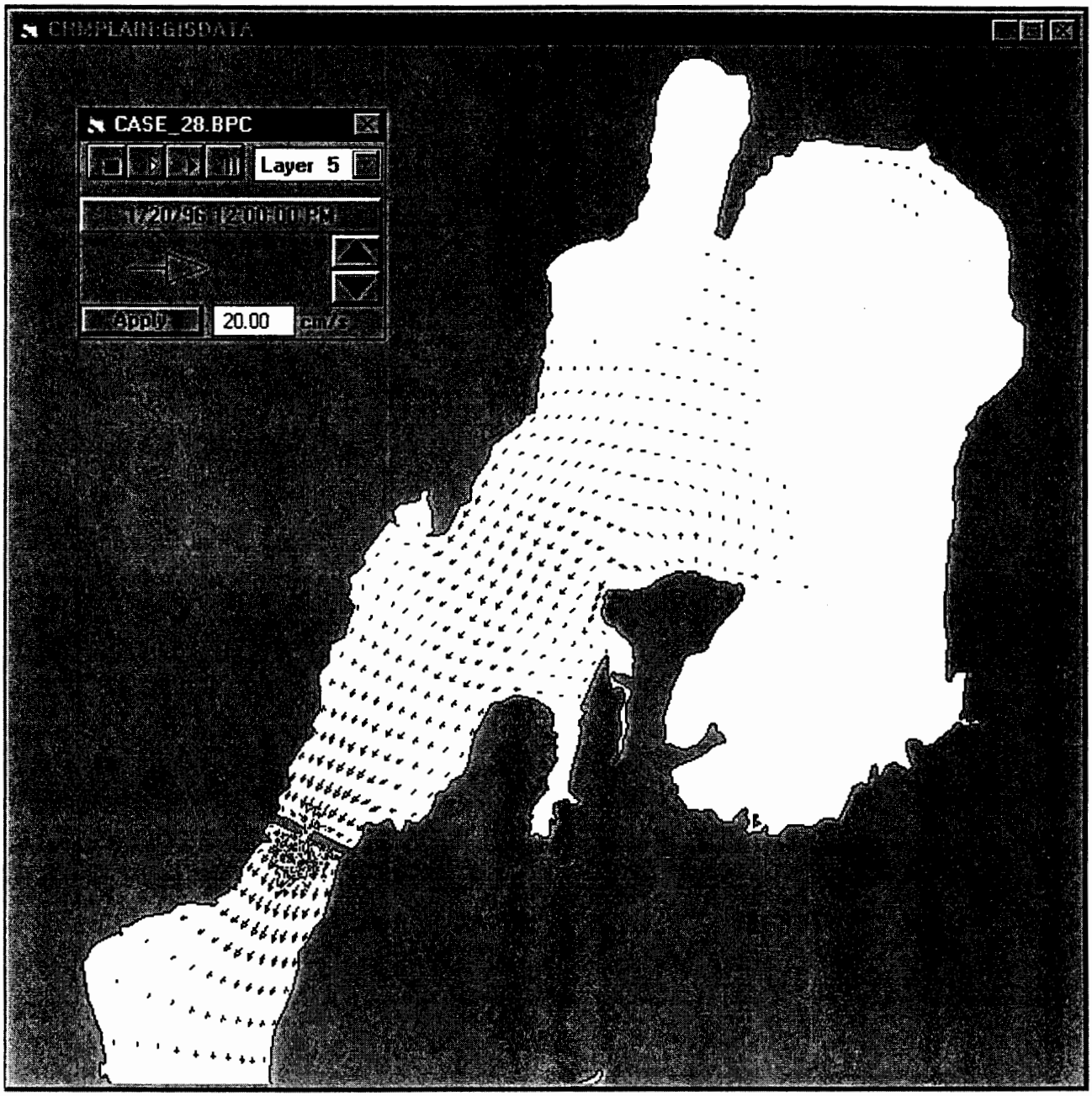

Figure 6.19 Plan view of surface currents for Case 28 (no wind, with present causeway configuration).

riv_s_28.bmp

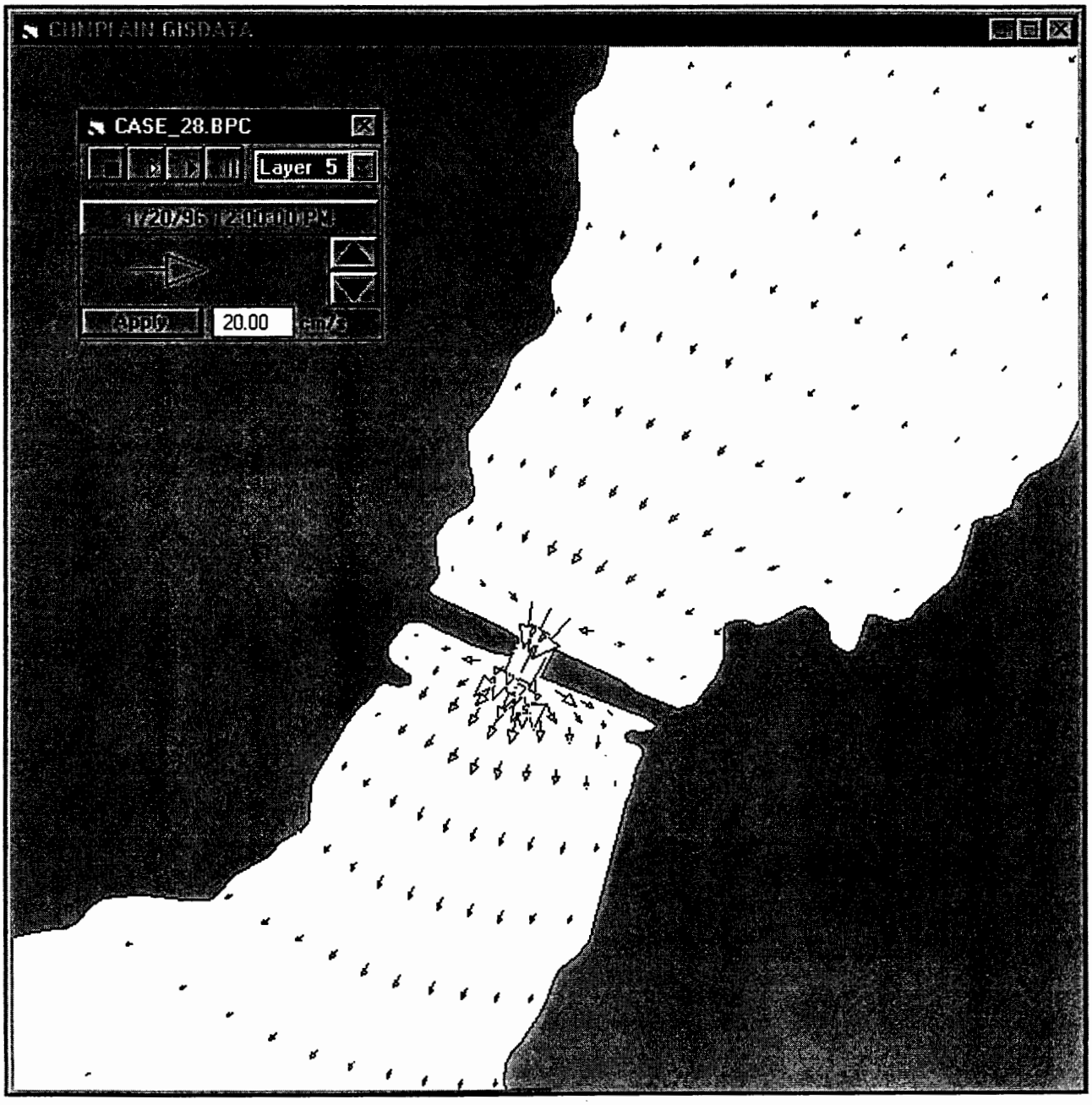

Figure 6.20 Detailed plan view of surface currents for Case 28 (no wind, with present causeway configuration).

case14_s.bmp

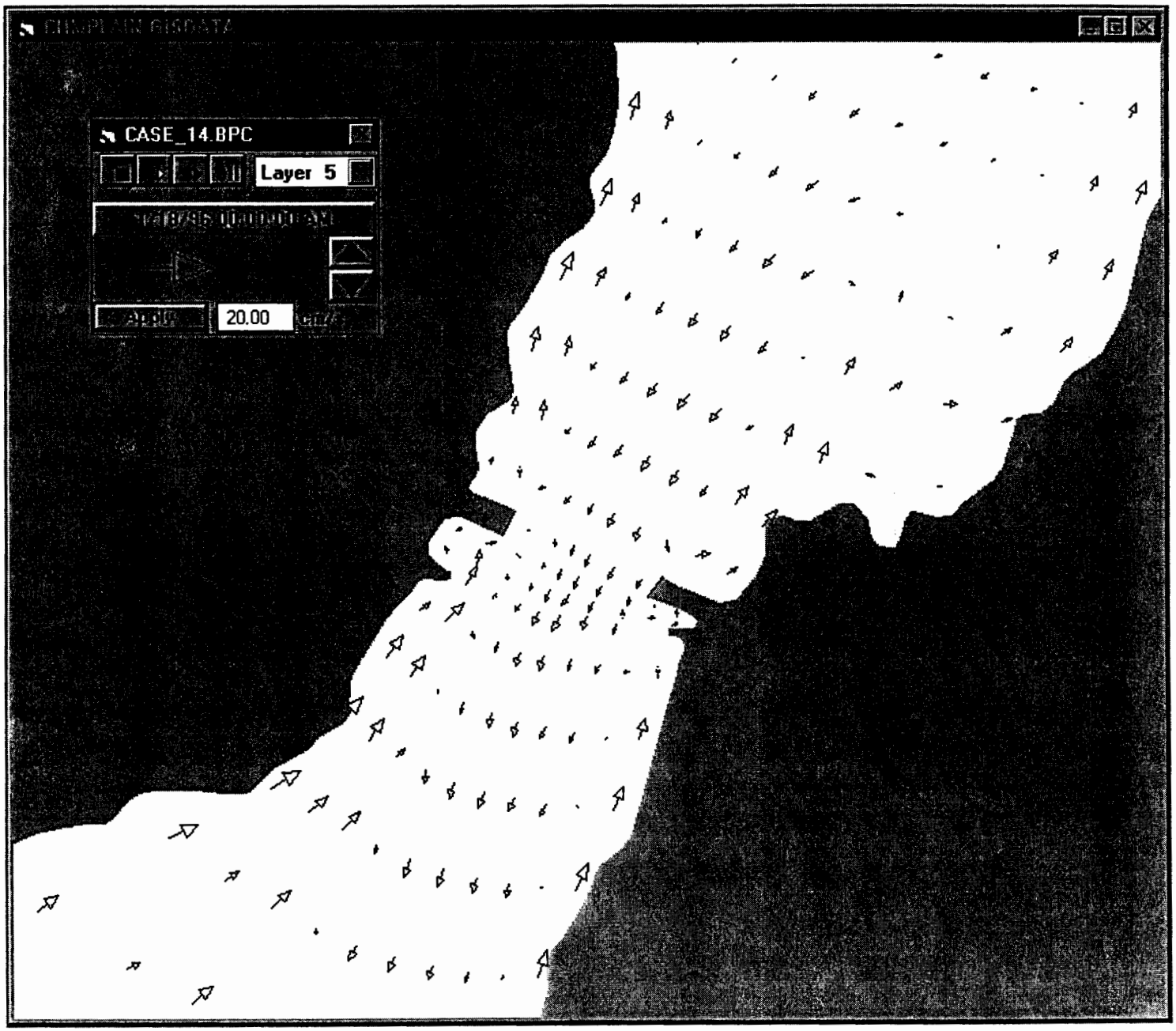

Figure 6.21 Detailed plan view of surface currents in the area near the causeway for Case 14 (50% of causeway removed from the center).

case14_b.bmp

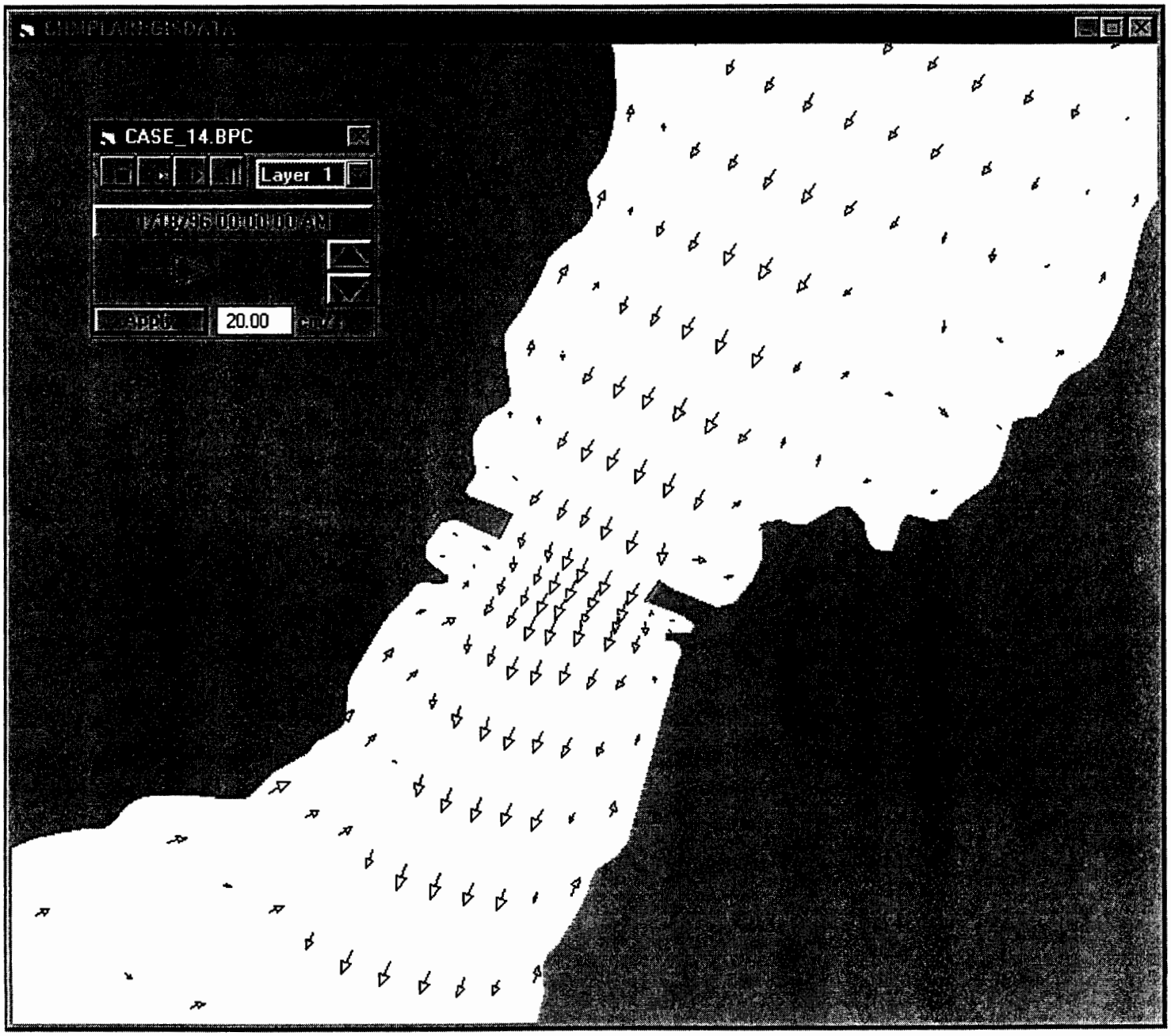

Figure 6.22 Detailed plan view of bottom currents in the area near the causeway for Case 14 (50% of causeway removed from the center).

case15_s.bmp

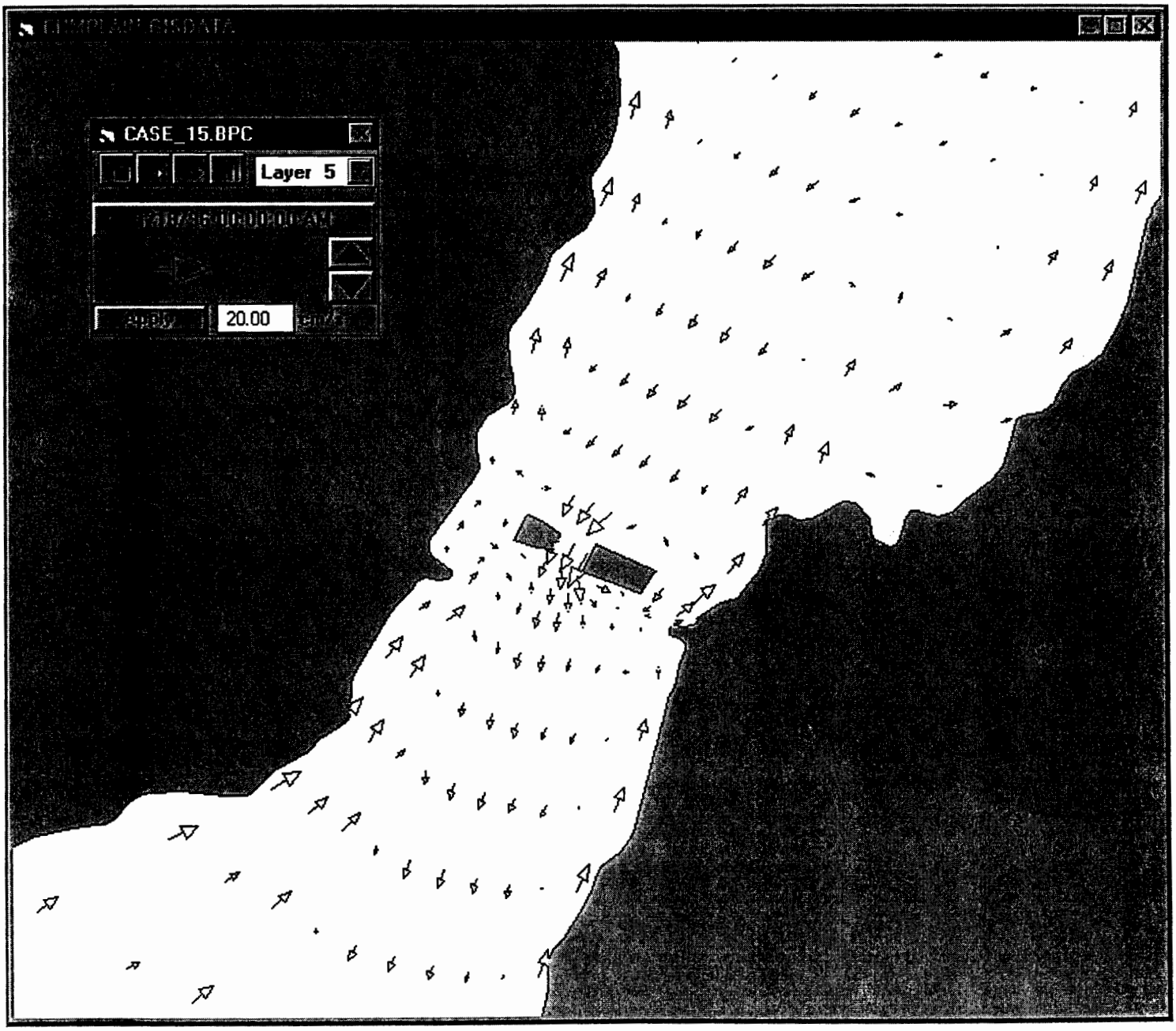

Figure 6.23 Detailed plan view of surface currents in the area near the causeway for Case 15 (25% of causeway removed from each shore).

case15_b.bmp

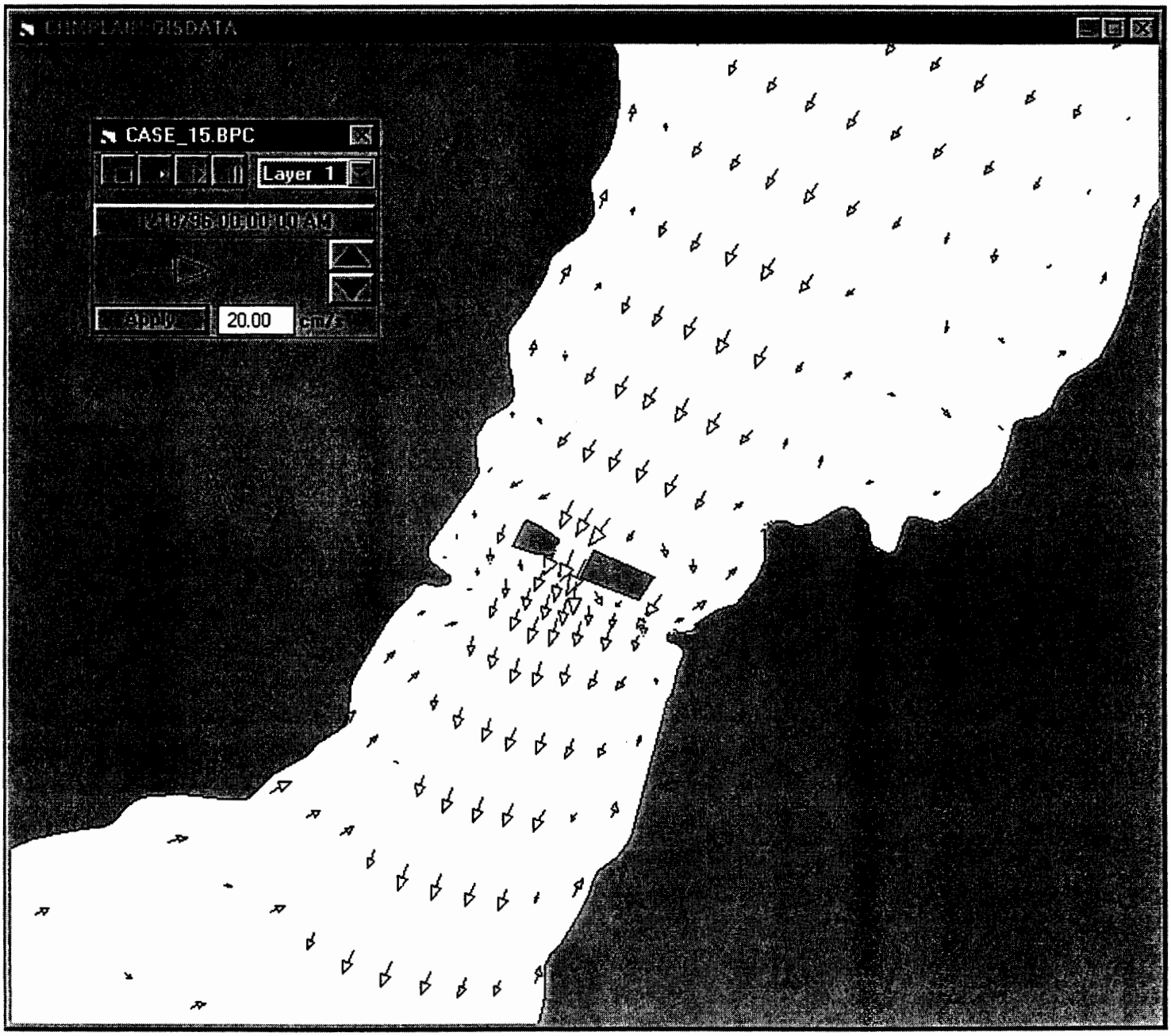

Figure 6.24 Detailed plan view of bottom currents in the area near the causeway for Case 15 (25% of causeway removed from each shore).

Figure 6.25(a) Plan view of vertically averaged water column concentrations for Case B1 (base case with present causeway configuration).

Table 6.1 Model predicted flushing times for Missisquoi Bay.

Case Name	Case pair Description	Flushing estimate (days)	Case difference (with-without)
case_b1	Base case	26.8	
case_b2		25.4	1.4
case_1	West wind	24.2	
case_2		23.6	0.6
case_3	20 mph wind	32.7	
case_4		26.4	6.3
case_5	30 mph wind	34.8	
case_6		26.8	8
case_30	5 mph wind	27.4	
case_7		26.8	0.6
case_31	Low river flow	105.8	
case_9		52.6	53.2
case_10	Railroad trestle	27.8	
case_11		25.6	2.2
case_12	Real wind	25.2	
case_13		26.5	-1.3
case_14	Center removal	26	
case_15	Shore removal	27	-1
case_16	North wind	15.1	
case_17		14.9	0.2
case_18	North-east wind	14.5	
case_19		14.3	0.2
case_20	East wind	23.6	
case_21		24.2	-0.6
case_22	South-east wind	30.6	
case_23		30.4	0.2
case_24	South-west wind	28.5	
case_25		27	1.5
case_26	North-west wind	15.4	
case_27		15	0.4
case_28	No wind	22.3	
case_29		21.8	0.5
case_32	No river flow	2697	
case_33		692.1	2004.9

flushing) are seen in the central portion of the bay, and in the smaller bays off the main bay (Venise Bay and Goose Bay), farthest from the river entrances and the entrance to the bay at the causeway.

The model predicted flushing time for this case is 26.8 days and is shown in Table 6.1, which includes the results of all 33 cases.

The concentration pattern shown in Figure 6.25(a) appears to have reached a quasi-steady state based on the volume weighted concentration data shown in Figure 6.25(b). The overall (volume weighted) concentration is decreasing over time but at a different rate than it did i

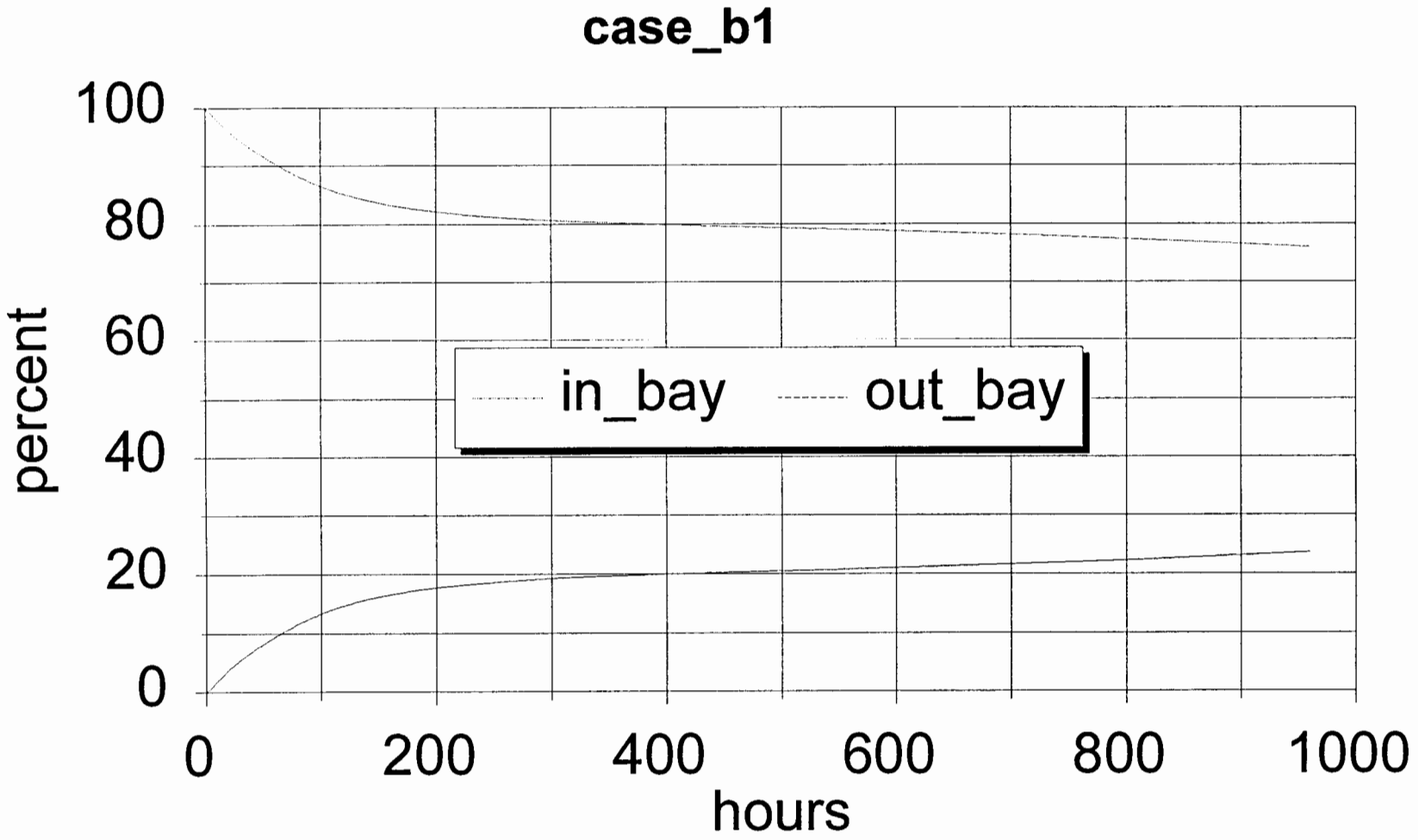

Figure 6.25(b) Volume weighted concentration change as a function of time for Case B1 (base case with present causeway configuration).

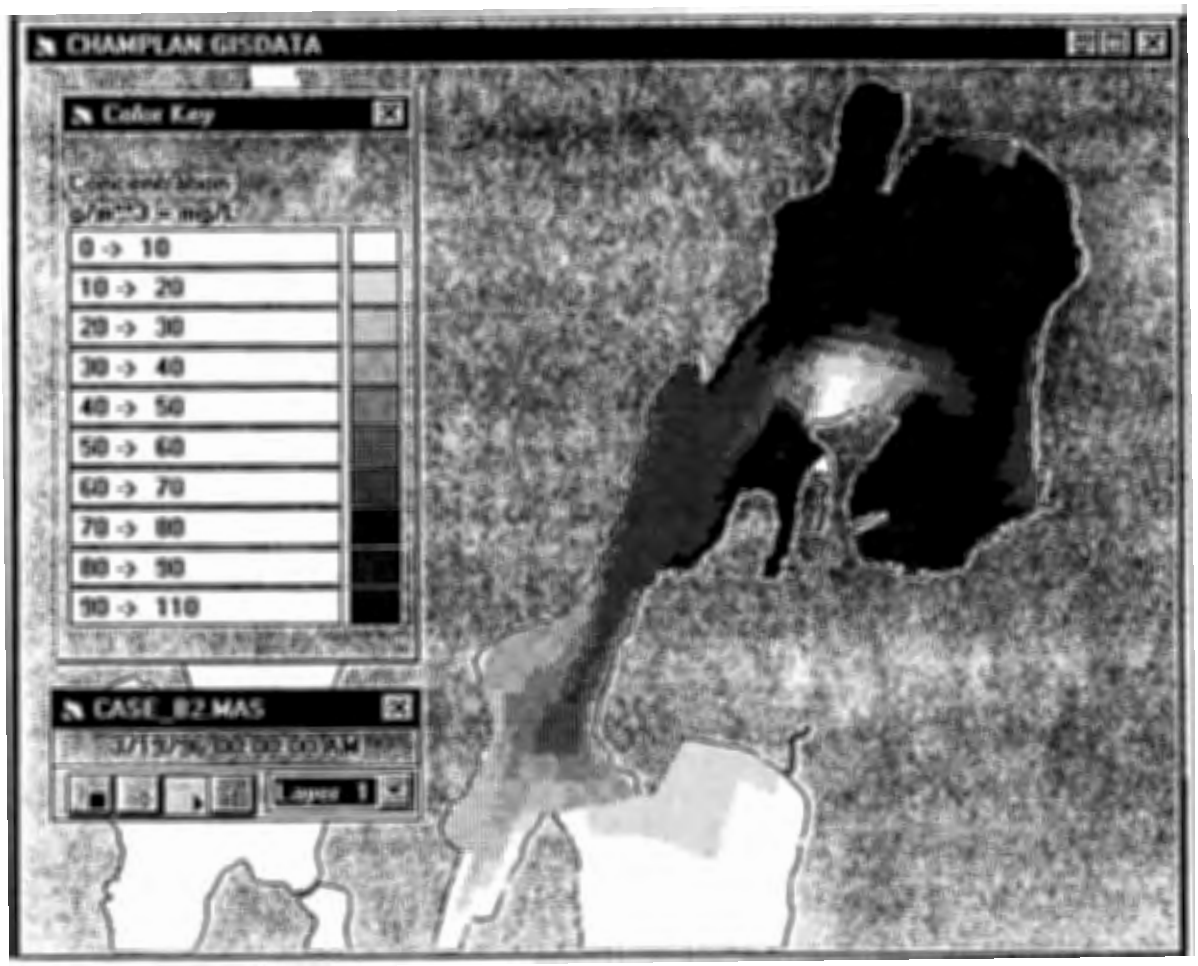

Figure 6.26 Plan view of vertically averaged water column concentrations for Case B2 (base case with the causeway completely removed).

somewhat lower than for case B1, which might be expected with the larger cross-sectional area for exchange. North of the entrance area, although the pattern exhibits slight variations, the concentrations are, overall, of the same order of magnitude.

The model-predicted flushing time for case B2 is 25.4 days. Comparing to 26.8 for case B1 a difference of 1.4 days, it can be seen that there is a small but appreciable change between the with and without causeway cases (~5%). This is an interesting result in light of the differences found between Figures 6.25(a) and 6.26. It is apparent that although the distribution of the mass in the bay has changed somewhat as a result of removal of the causeway, the overall mass in the bay remains substantially unchanged.

Case 1

Figure 6.27 shows the plan view of vertically averaged water column concentrations for Case 1 (west wind with present causeway configuration) again 40 days into the simulation. Comparing the concentration contours with the base case (case B1) a substantial difference is noticeable. Most of the bay shows lower concentrations for this case, particularly in the eastern half of the basin. The concentration plume also extends much farther into the Northeast Arm, for case 1 than for the base case, covering Maquam Bay and south along the east shore.

The model predicted flushing time for Case 1 is 24.2 days. Comparing this to 26.8 days for the with causeway base case shows a 2.7 day difference. The west wind case appears to flush the bay quite a bit faster than the comparable case with a south-southwest wind. This appears to be due at least in part to the fact that the Missisquoi River flows to the east under a west wind rather than towards the causeway, as in the base case. With the Missisquoi River and its lower (zero) concentration input heading east, this allows a sustained flushing of waters with higher concentrations at least initially.

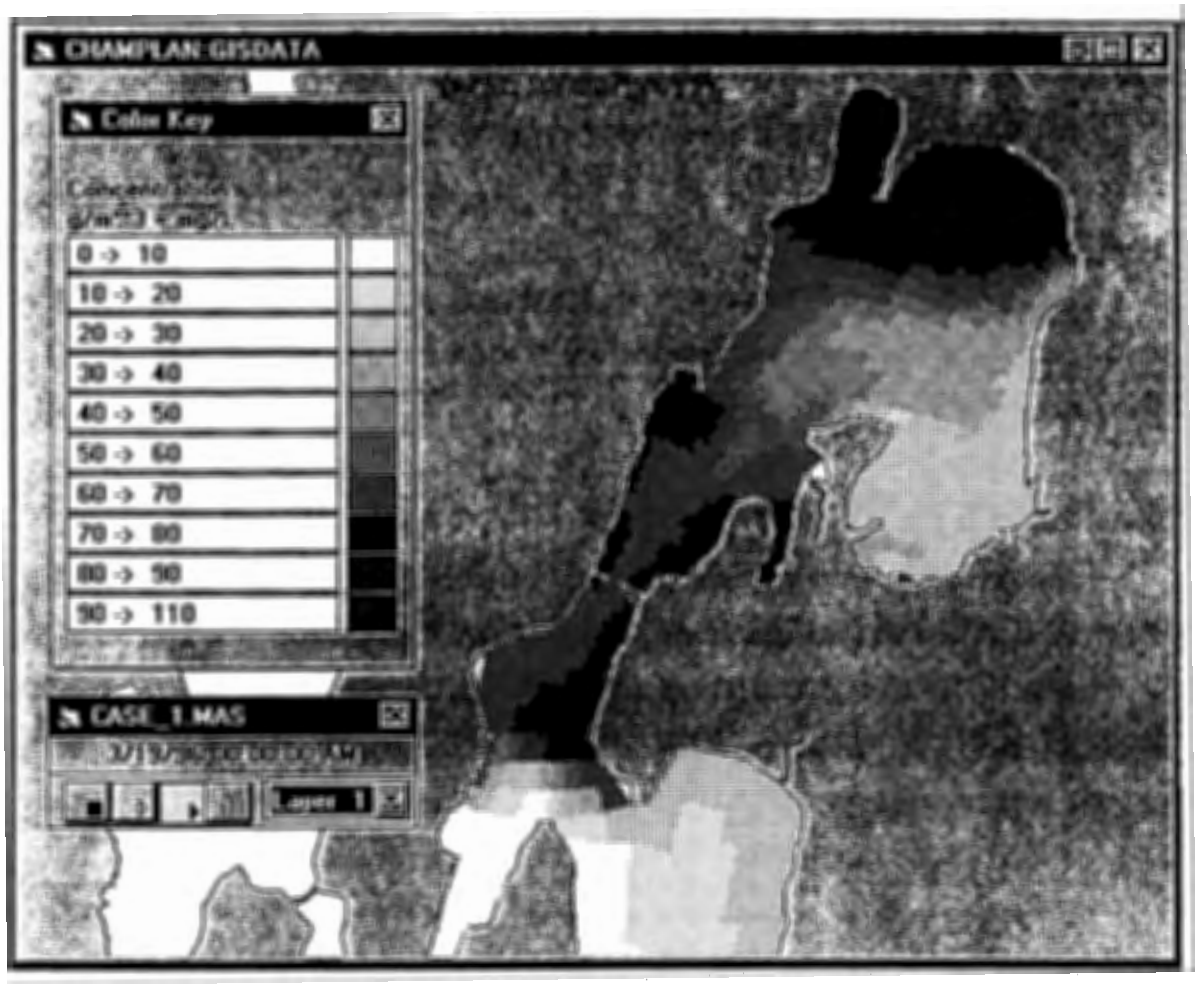

Figure 6.27 Plan view of vertically averaged water column concentrations for Case 1 (west wind with present causeway configuration).

Case 2

The vertically averaged water column concentration contours for case 2 with the causeway removed are shown in Figure 6.28. The contours are nearly identical to those predicted for case 1 (with the causeway).

The model predicted flushing time for Case 2 is 23.6 days. Comparing this to the 24.2 days for case 1 it can be seen that there is only a 0.6 day difference in the flushing rate between the two (~2%).

Cases 16, 17, 20 and 21

The vertically averaged water column concentration contours for Cases 16 and 17 (north wind and without causeway, respectively) are shown in Figures 6.29 and 6.30. By inspection, it is clear that flushing occurs far more rapidly with a north wind than with either the south-southwest or west winds. The model predicted flushing times for the with and without cases are 15.1 and 14.9 days respectively, only a 1% difference between the two, but approximately 43% increase over the base cases.

The water column concentrations for the east wind cases (Case 20 and 21 for with and without causeway, respectively) also show a substantial decrease in concentration over the base cases as can be seen in Figures 6.31 and 6.32. The predicted flushing times for cases 20 and 21 are 23.6 and 24.2 days, respectively. These times do not show the dramatic reduction that the north wind cases did, but are still substantially lower than the base cases (an 11% decrease). There is also an increase in flushing time for the with causeway case for the east wind (a 0.6 day increment, 2%).

The model predicted flushing time as a function of wind direction is given in Table 6.2 for the complete set of eight points of the compass. What becomes clear immediately from Table 6.2 is the tendency for wind pointing towards the causeway, (northwest, north and northeast) to have reduced flushing times. Conversely, winds directed into the bay from the causeway appear to inhibit flushing (increased flushing times).

Figure 6.28 Plan view of vertically averaged water column concentrations for Case 2 (west wind with the causeway completely removed).

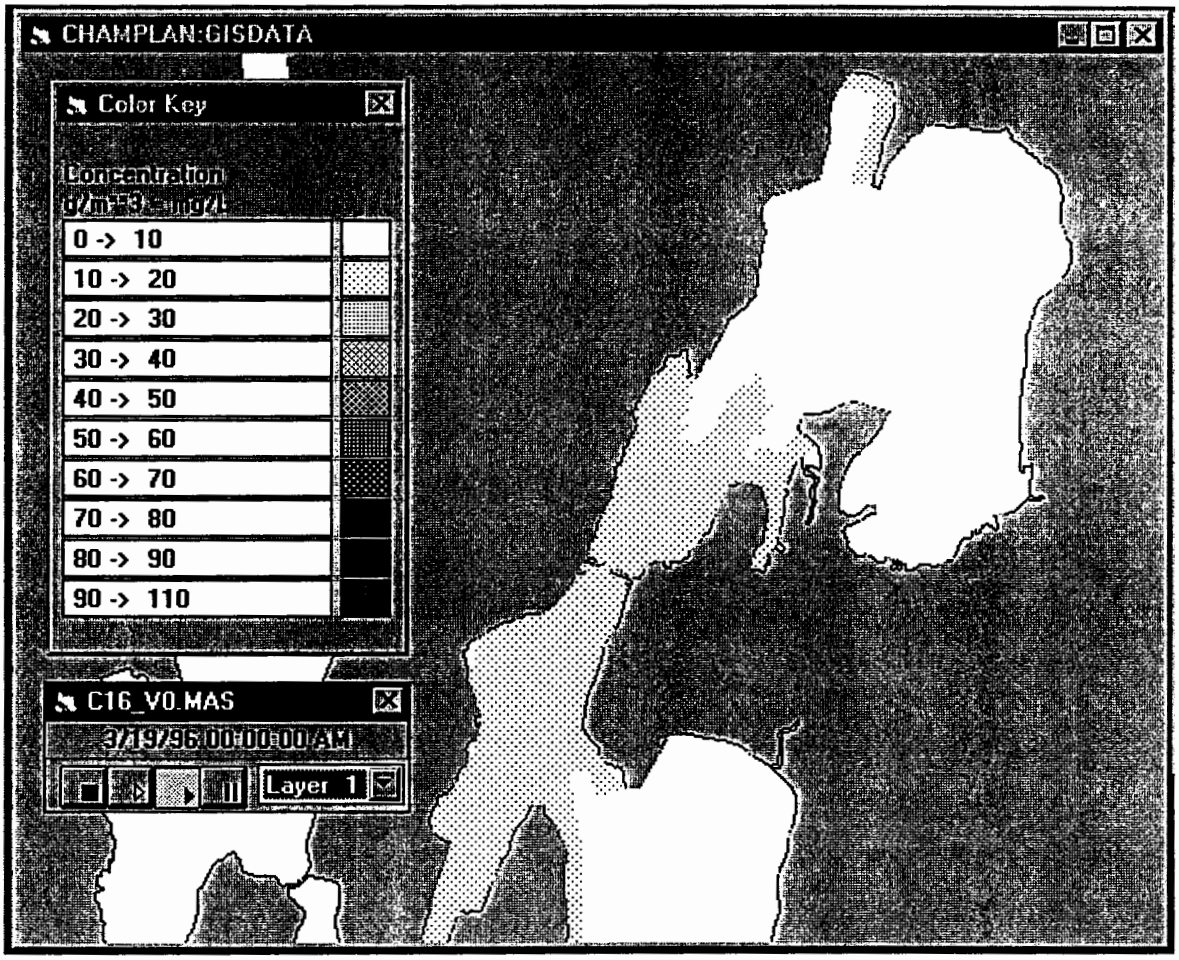

Figure 6.29 Plan view of vertically averaged water column concentrations for Case 16 (north wind with present causeway configuration).

Figure 6.30 Plan view of vertically averaged water column concentrations for Case 17 (north wind with causeway completely removed).

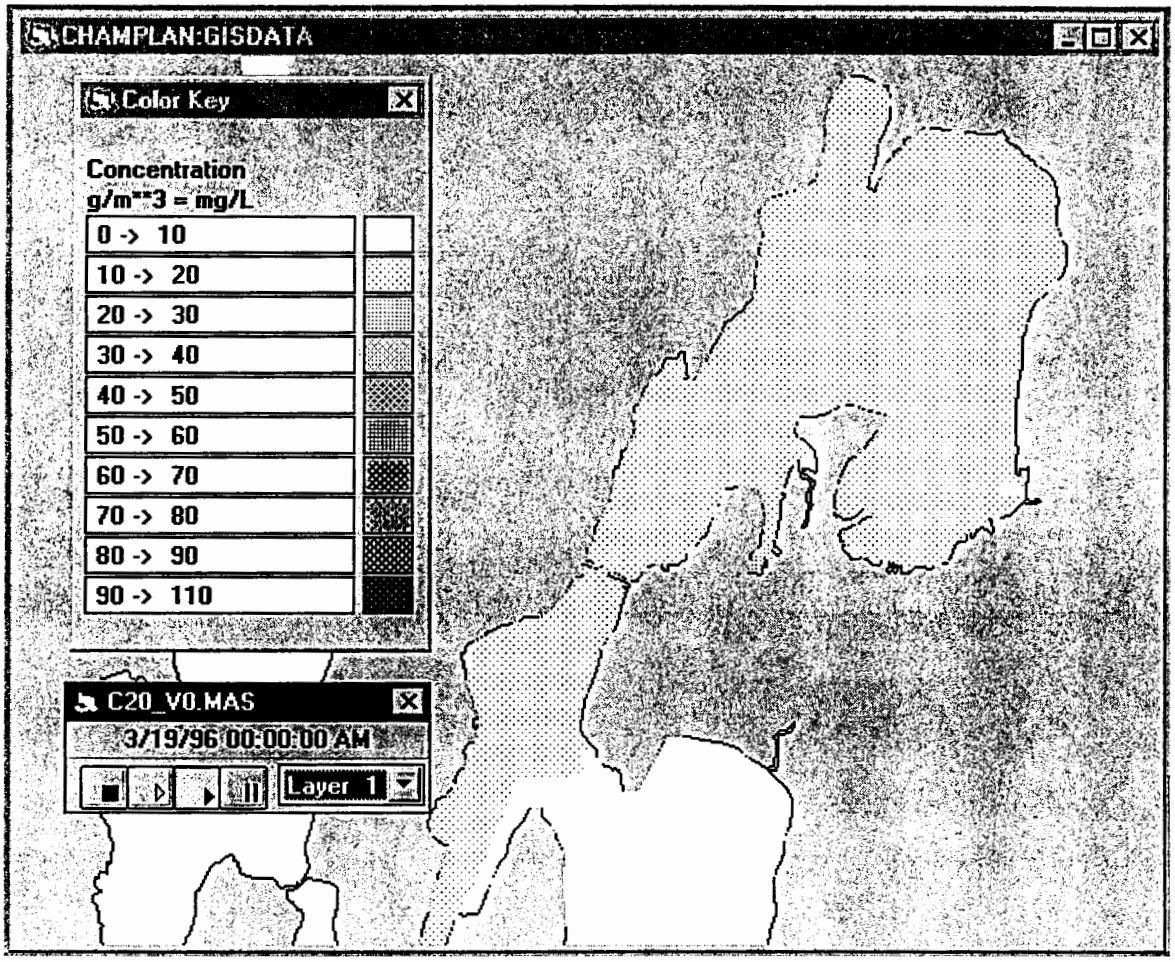

Figure 6.31 Plan view of vertically averaged water column concentrations for Case 20 (east wind with present causeway configuration).

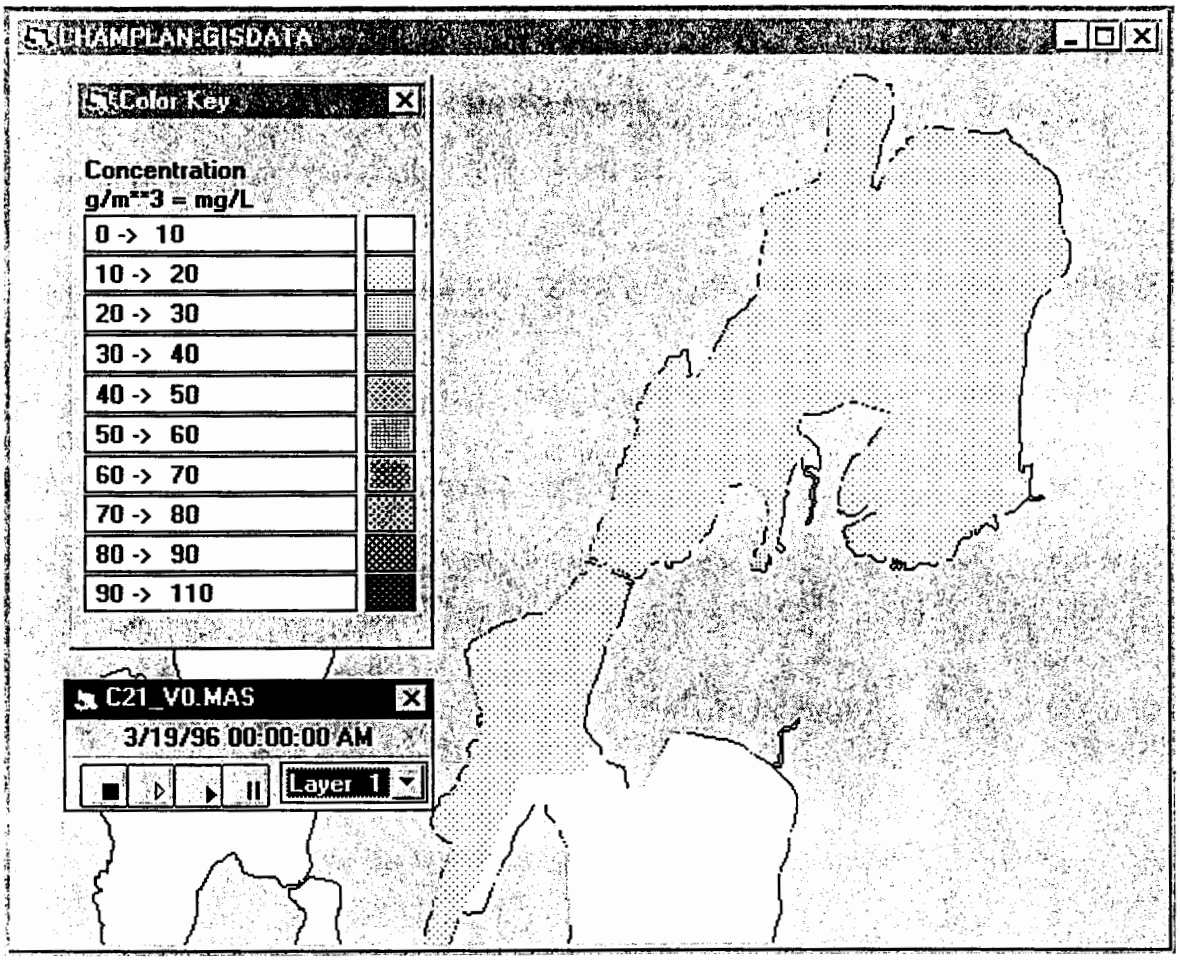

Figure 6.32 Plan view of vertically averaged water column concentrations for Case 21 (east wind with causeway completely removed).

Cases 28 and 29

For the no wind cases (28 and 29) the water column concentration plan views show three low concentration zones at the mouth of each river as expected (Figures 6.33 and 6.34). The size of the low concentration areas are also proportional to the river flow rate and all spread evenly away from the river mouth towards the causeway. The predicted flushing time for the no wind cases are 22.3 and 21.8 days for the wind and without causeway cases respectively. Interestingly, these numbers are exactly equal to the mean of the eight wind direction cases.

Table 6.2 Model predicted flushing times for Missisquoi Bay as a function of wind direction.

Wind Direction	"Flushing Days" with	without	difference
N	**15.1**	**14.9**	**0.2**
NE	**14.5**	**14.3**	**0.2**
E	**23.6**	**24.2**	**-0.6**
SE	**30.6**	**30.4**	**0.2**
SSW	**26.8**	**25.4**	**1.4**
SW	**28.5**	**27.0**	**1.5**
W	**24.2**	**23.6**	**0.6**
NW	**15.4**	**15.0**	**0.4**
No wind	**22.3**	**21.8**	**0.5**
Low River Flow	**105.8**	**52.6**	**53.2**
No River Flow	**2697.**	**1050.**	**2004.**

Cases 32 and 33

The no river flow, no wind flow cases for configurations with and without the causeway, (cases 32 and 33, respectively) were added to assist in the understanding of how the purely diffusive forces were influencing the flushing of the bay. From the model predicted flushing times shown in Table 6.1 it is clear that if the only forces working on the bay were diffusive in nature then the causeway would provide a huge impediment to the movement of material out of the bay. The implications of this result are that

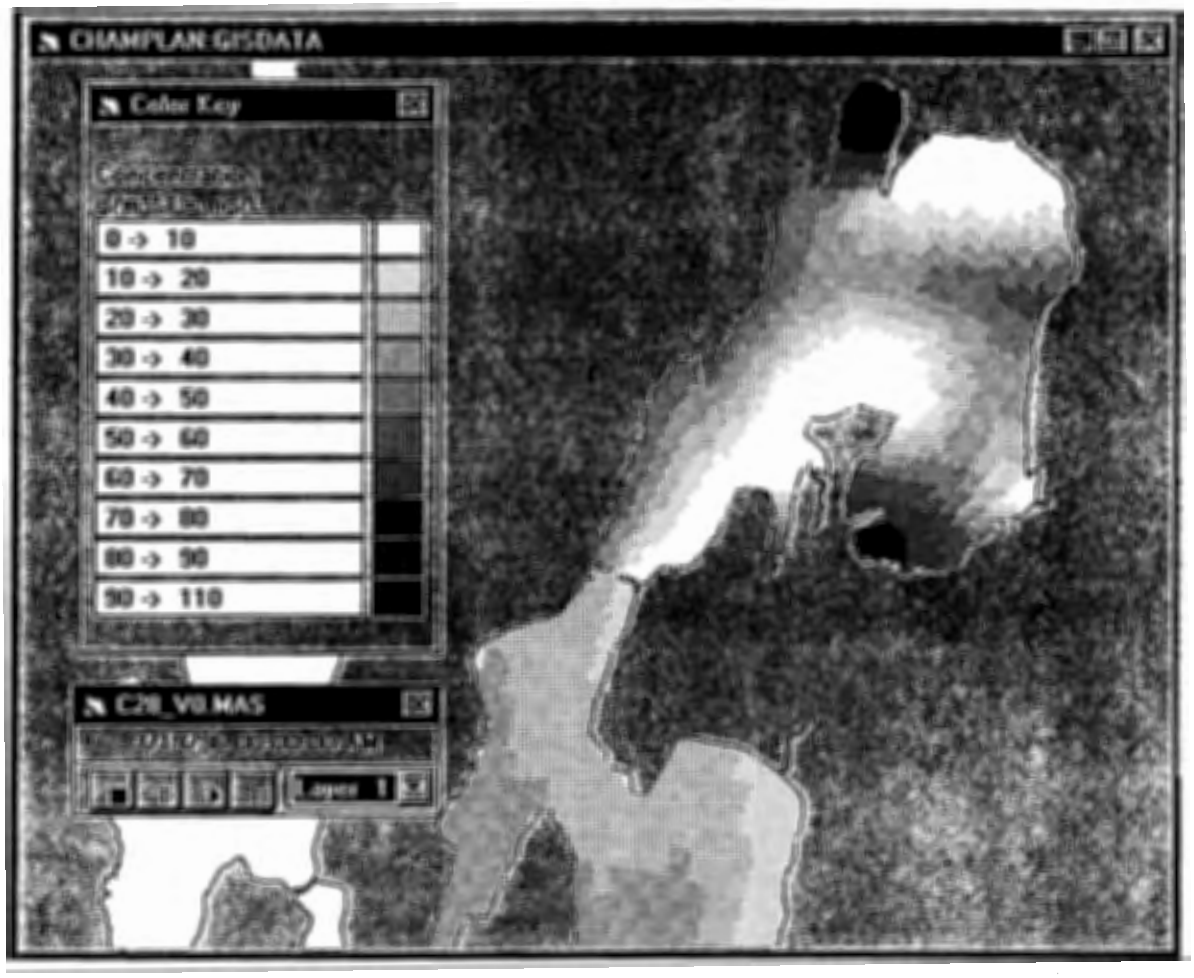

Figure 6.33 Plan view of vertically averaged water column concentrations for Case 28 (no wind with present causeway configuration).

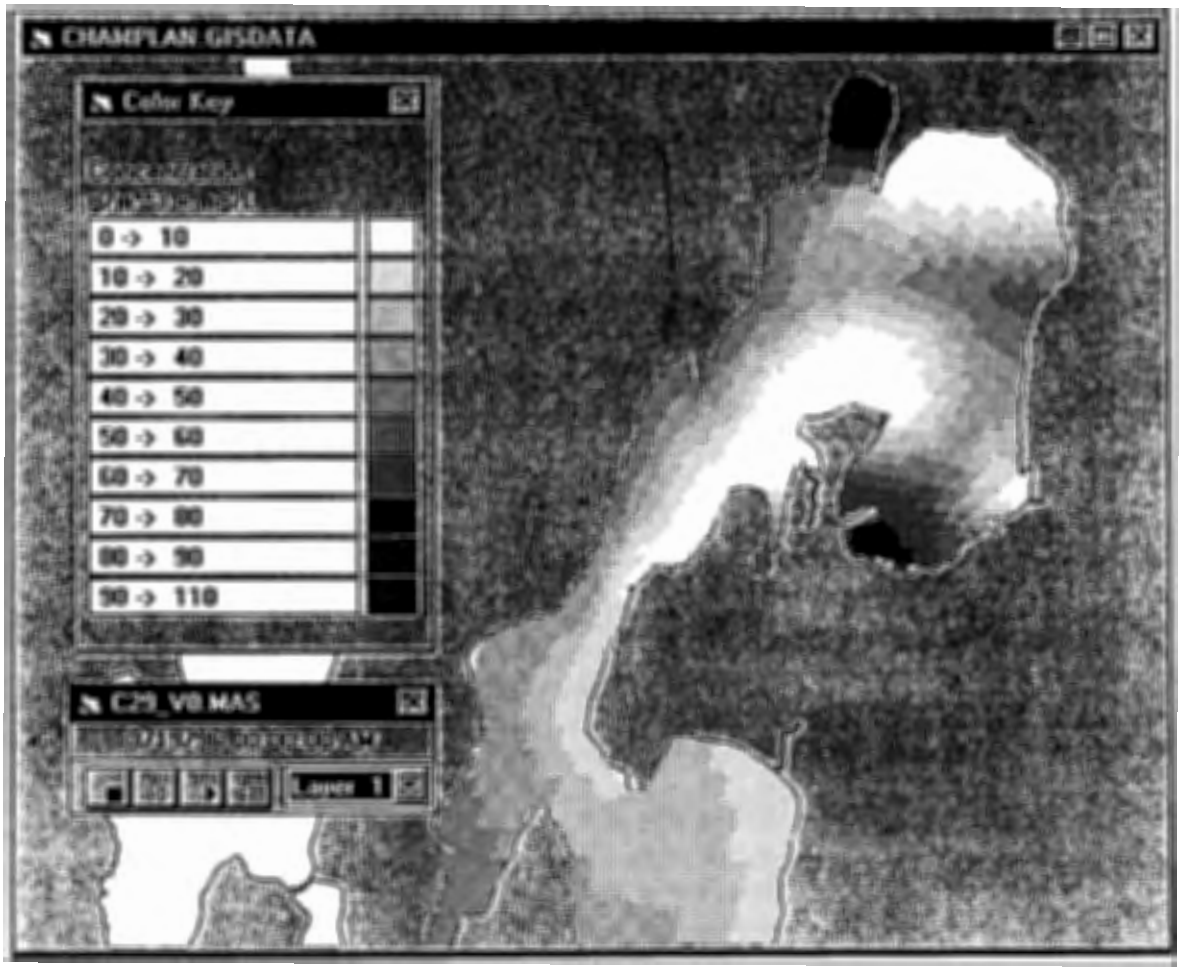

Figure 6.34 Plan view of vertically averaged water column concentrations for Case 29 (no wind with causeway completely removed).

as the river flow decreases the width of the opening at the causeway becomes increasingly important. Compare, for example, the base cases, the low river cases and this set (Cases B1, B2, 31, 9, 32, 33).

Other Cases

The final concentration ratio for each case can be found in Table 6.1 for comparison. Following is a summary of each of the cases not described above.

The simulation with high lake level (case 8) showed a slight decrease in flushing time over the base case.

The real wind time series cases provided no real insight into the flushing response of the basin. The simulations were run for a period covering 40 days starting on April 1, 1991. The calculated flushing times for both cases do not substantially deviate from the base cases except that the case with no causeway has a slightly higher flushing time than the present case, (opposite to that of the base cases).

The smallest dilution (i.e., the longest flushing time, 105.8 days; not including the no river flow case) was for the reduced river flow case with the present causeway configuration (case 31). This case was followed in flushing time length by its no causeway counterpart (case 9) which had a 52.6 day flushing time.

The railroad trestle variation (cases 10 and 11) appeared to have little effect, increasing the flushing time 0.2 days over the base case (<1%).

6.3 Sediment Transport Model

The sediment transport model was run for 28 of the original 35 case matrix. Several of the cases run in the preliminary flushing analyses provided little additional insight into the behavior of the bay and so were dropped from the sediment transport study. Again results from the two base cases (B1 and B2) will be presented along with the wind direction variation cases including the west, north, and east wind cases, with and without the causeway.

The sediment transport simulation output for the selected cases is presented in two steps; the sedimentation rate in the bay for the present causeway configuration and the difference in sedimentation rate between the present causeway configuration and the complete causeway removal cases. The sedimentation rate difference contours

display both positive and negative values. The difference is calculated as the sedimentation rate with the present causeway configuration less the rate with the causeway removed, (e.g. Case_B1 - Case_B2). A positive difference reflects a greater sedimentation rate with the present causeway configuration. Therefore, a positive rate differences in the bay implies more sediment is being transported out of the bay with the causeway removed case.

At the end of each case the total amount of sediment within the bay and the total outside the bay are calculated and a percentage is determined. The difference between the with and without causeway cases is then tallied. The results of these calculation is presented in Table 6.3 for each of the cases.

Cases B1 and B2

The plan view of the sedimentation rate in the bay for Case B1, (the base case, south-southwest wind with the present causeway configuration) is shown in Figure 6.35. The settling velocity for this case was 0.2 m/day. The figure shows a not unexpected sedimentation pattern, highest near the mouth of the Missisquoi (it appears white because it is off the scale at the high end) and decreasing as you move away from the river. The other rivers exhibit a similar behavior although not at the same magnitude. There is a distinct sedimentation 'plume' heading towards the causeway from the Missisquoi delta area which continues out of the bay through the causeway. The small bays farthest from the source rivers, (e.g. Venise Bay to the north) show the least sedimentation.

Figure 6.36 shows the plan view of the sedimentation rate difference between the Cases B1 and B2, (with and without the causeway). Note that the sedimentation rate scale is not linear and that it shows both positive and negative rate differences, a large range of differences is therefore represented on each difference plot. There is a striking feature in the area just north of the causeway between the causeway and Chapman Bay on the west shore. Here a long strip of positive sedimentation rate difference can be seen to extend from the causeway to Chapman Bay and from the shore to the center of the channel. The positive sedimentation rate difference indicates that less sediment would be deposited there if the causeway were removed.

Conversely, a negative rate is seen in the area outside of the bay to the south west of Hog Island.

To put the positive sedimentation rate difference south of Chapman Bay in perspective, the 0.025-0.05 ($g/m^2/hr$) contour is roughly equivalent to 0.25-0.5 kg per square meter less material per year in that area. The larger contour, including Chapman Bay, is roughly equivalent to 0.01-0.25 kg per square meter less material per year. Outside of the bay the predicted increase in sedimentation southwest of Hog Island is roughly equivalent to a 0.01-0.25 kg per square meter increase of material per year over a somewhat larger area. It should be noted at this point that these estimates assume a total suspended sediment load from the rivers of 4515 (g/sec).

Refering to Table 6.3 it can be seen that the difference of the total sedimented material in the bay for the present causeway configuration versus that with the causeway completely removed is only 0.28%. A slight decrease in sedimentation if the causeway is removed.

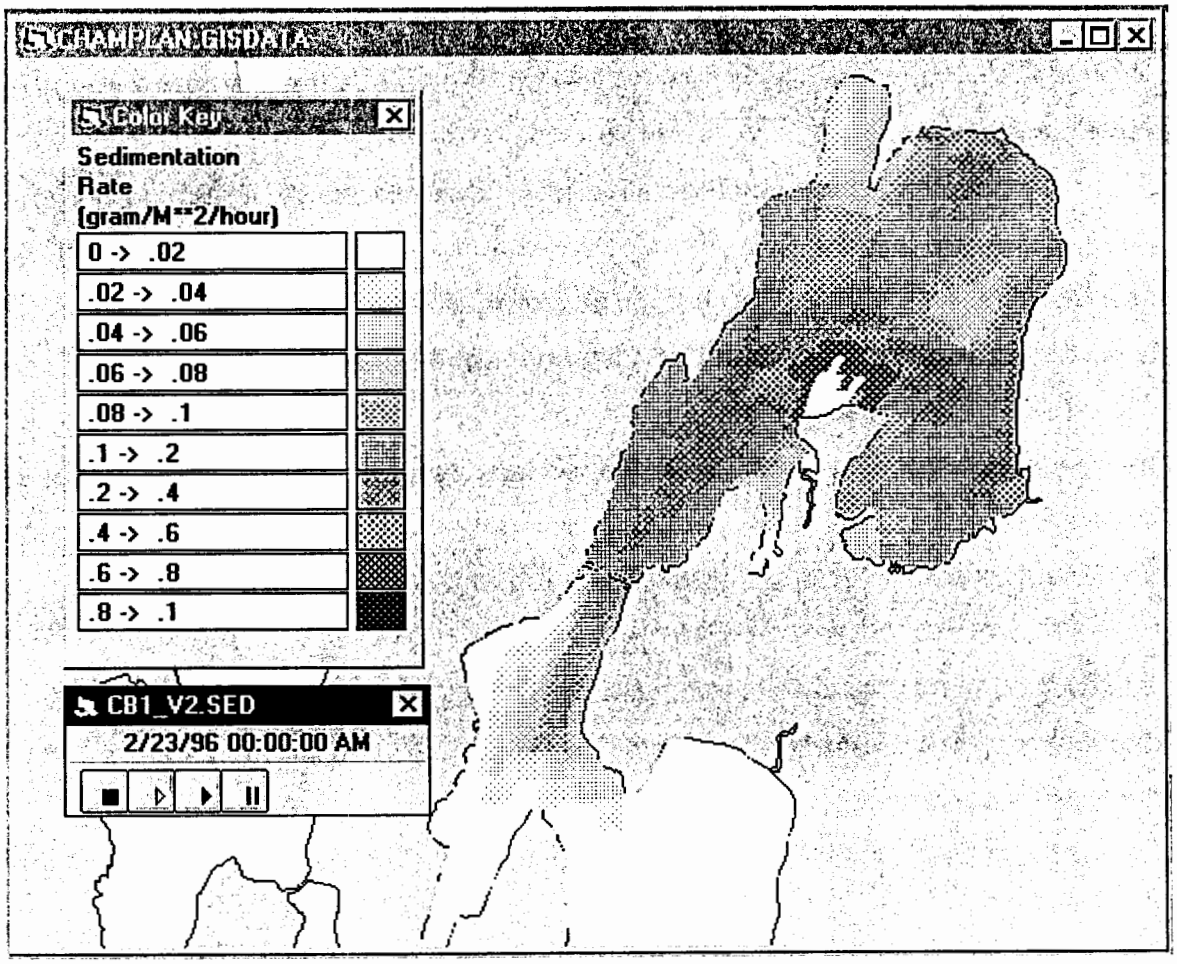

Figure 6.35 Plan view of the sedimentation rate for Case B1 (base case with present causeway configuration).

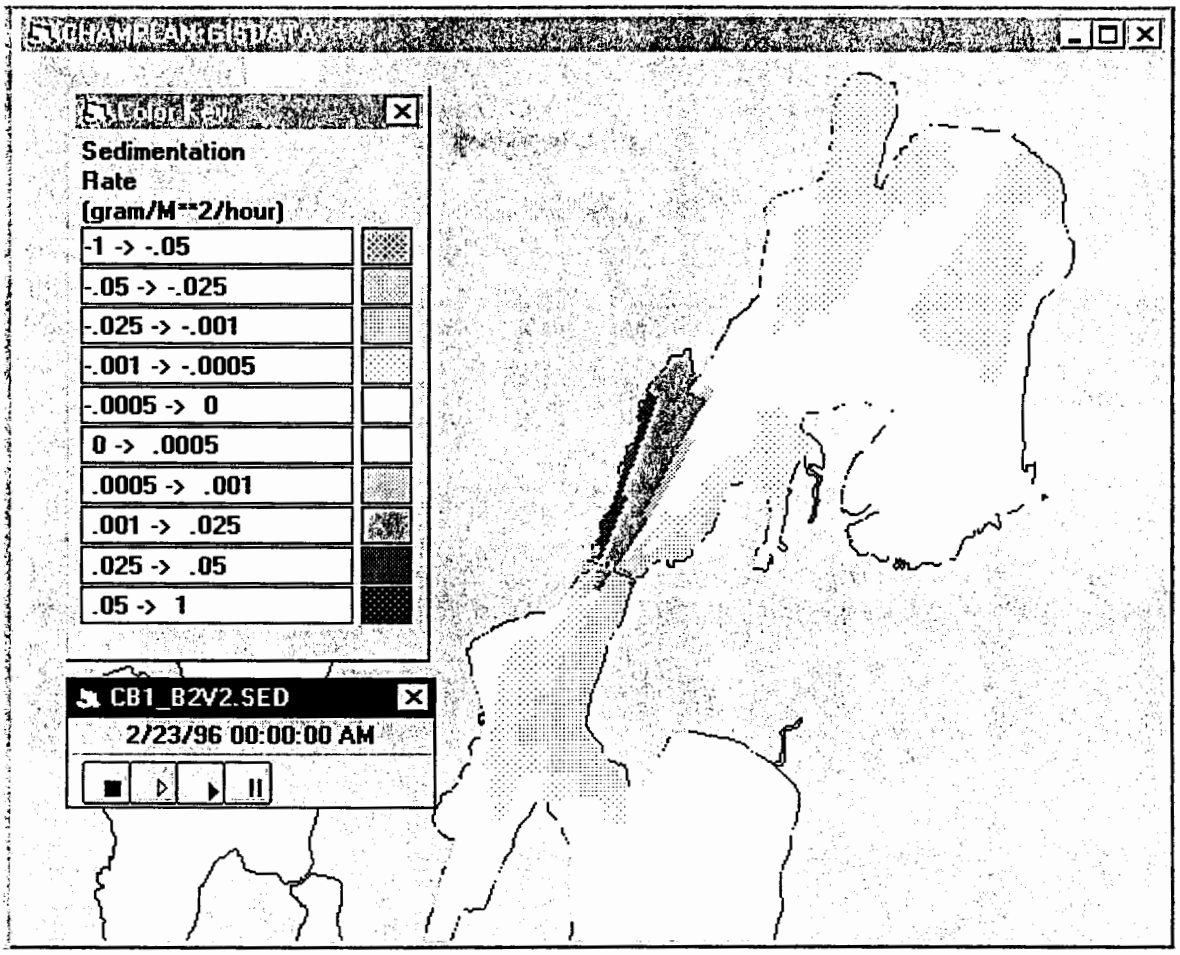

Figure 6.36 Plan view of the difference in sedimentation rate between Case B1 and Case B2 (base case with and without the causeway, respectively).

Table 6.3 Model predicted sediment deposition rate and deposition rate difference for cases with and without the causeway.

Case Name	Case Description	Sediment deposition (%) in the bay	out	NOCW-WCW	cell by cell difference min-max (gram/M**2/hour)	
CB1_V2	Base case	93.63	6.37			
CB2_V2		93.35	6.65	0.28	0.071	-0.114
C1_V2	West wind	98.27	1.73			
C2_V2		98.25	1.75	0.02	0.006	-0.010
C5_V2	30 mph wind	96.12	3.88			
C6_V2		95.10	4.90	1.02	0.100	-0.105
C30_V2	5 mph wind	92.31	7.69			
C7_V2		92.24	7.76	0.07	0.048	-0.101
C31_V2	Low river flow	99.49	0.51			
C9_V2		99.03	0.97	0.46	0.039	-0.045
C12_V2	Real wind	85.54	14.46			
C13_V2		95.46	4.54	-9.92	1.280	-0.217
C16_V2	North wind	97.69	2.31			
C17_V2		97.59	2.41	0.10	0.012	-0.026
C18_V2	North-east wind	83.62	16.38			
C19_V2		82.73	17.27	0.89	0.086	-0.145
C20_V2	East-wind	85.18	14.82			
C21_V2		84.58	15.42	0.60	0.024	-0.054
C22_V2	South-east wind	89.89	10.11			
C23_V2		90.09	9.91	-0.20	0.040	-0.035
C24_V2	South-west wind	96.21	3.79			
C25_V2		96.03	3.97	0.18	0.041	-0.069
C26_V2	North-west wind	97.99	2.01			
C27_V2		97.89	2.11	0.10	0.001	-0.008
C28_V2	No wind	94.25	5.75			
C29_V2		94.05	5.95	0.20	0.042	-0.106

Summary count : no significant difference (less then 1.%) : 10
more out with the causeway (> 1.0) : 2
more out without the causeway (< 1.0) : 1
total : 13

Cases 1 and 2

The plan view of the sedimentation rate for Case 1, (west wind with the present causeway configuration) is shown in Figure 6.37. The pattern of deposition is somewhat different here most noticably reflecting the eastward current flow at the mouth of the Missisquoi River (Figures 6.9 and 6.10). Currents at the mouth of the Pike River also drive the suspended sediments to the east leaving the area to the west with a lower deposition rate.

The sedimentation rate difference between Cases 1 and 2 (with and without the causeway) is shown in Figure 6.38. The differences are slight and confined to the region in the vicinity of the causeway. A total sedimentation difference of only 0.02% was calculated for this case.

Cases 16 and 17

For the north wind cases (16 and 17) the sedimentation rate pattern is quite different than that of either the base cases or the west wind cases as can be seen in Figure 6.39. The area to the north of the causeway appears to sustain a lower rate than that of the base case. Increased sedimentation rates are again seen to the east of the Missisquoi delta as a result of currents. Sedimentation rate patterns are clearly influenced by the circulation patterns displayed by the hydrodynamic model predictions.

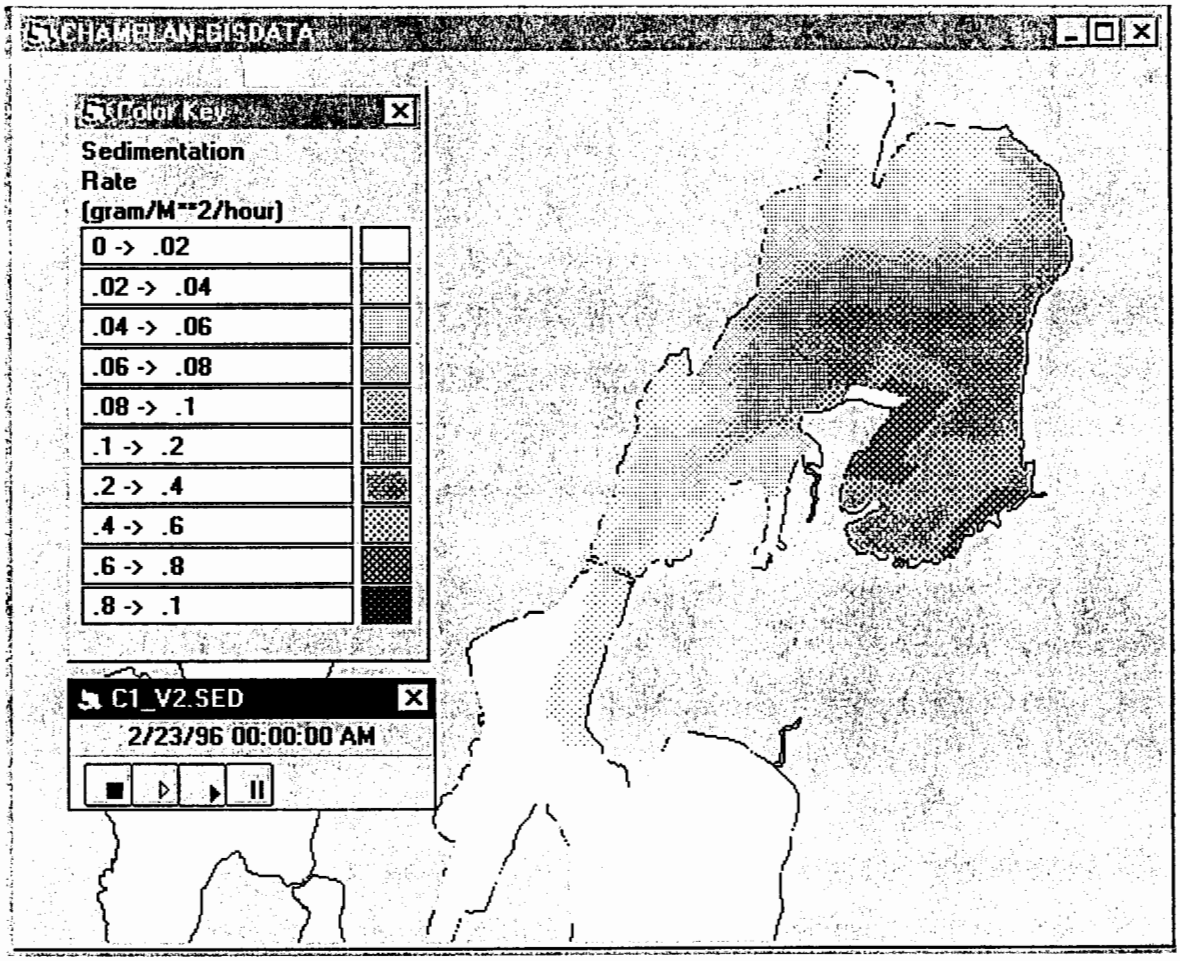

Figure 6.37 Plan view of the sedimentation rate for Case 1 (west wind with present causeway configuration).

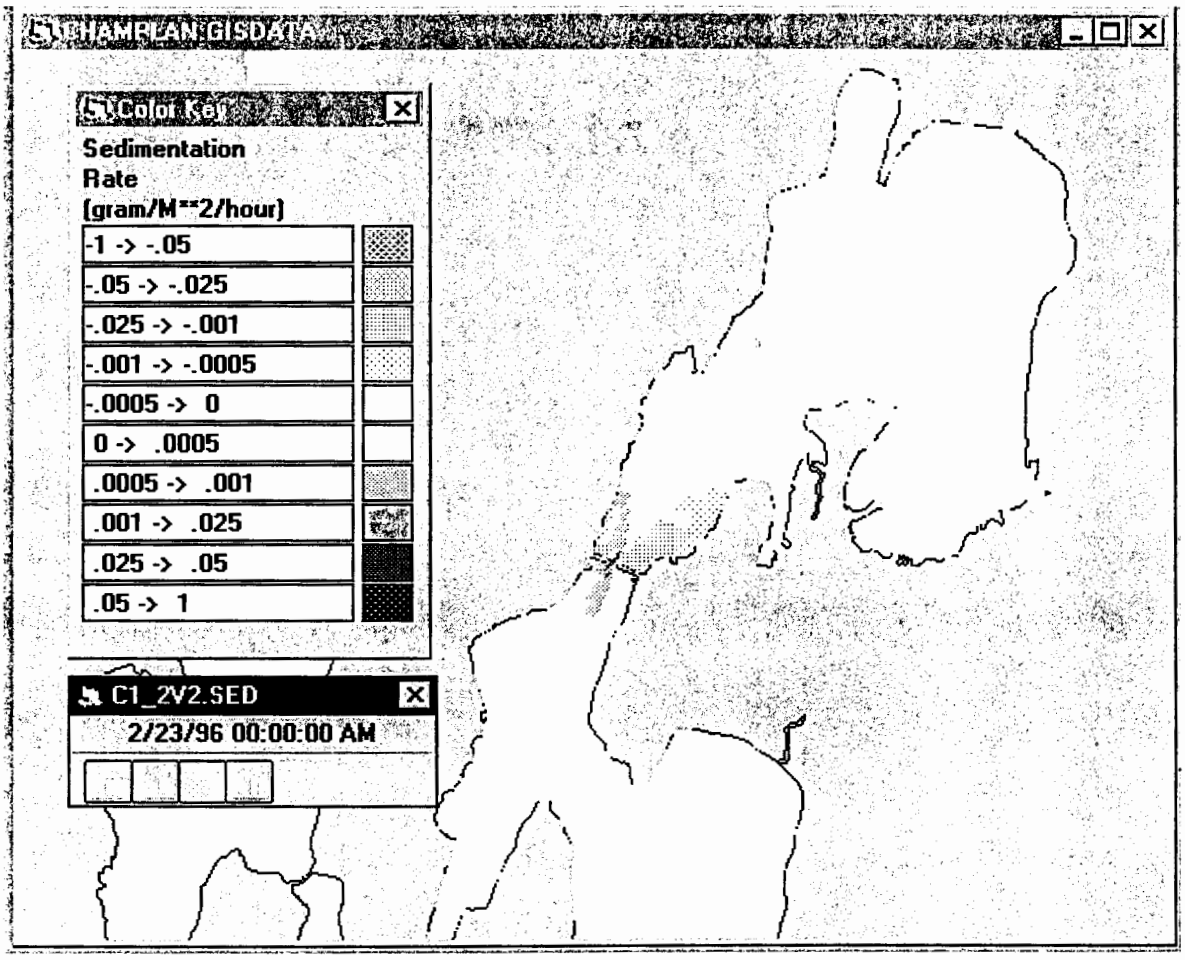

Figure 6.38 Plan view of the difference in sedimentation rate between Case 1 and Case 2 (west wind with and without the causeway, respectively).

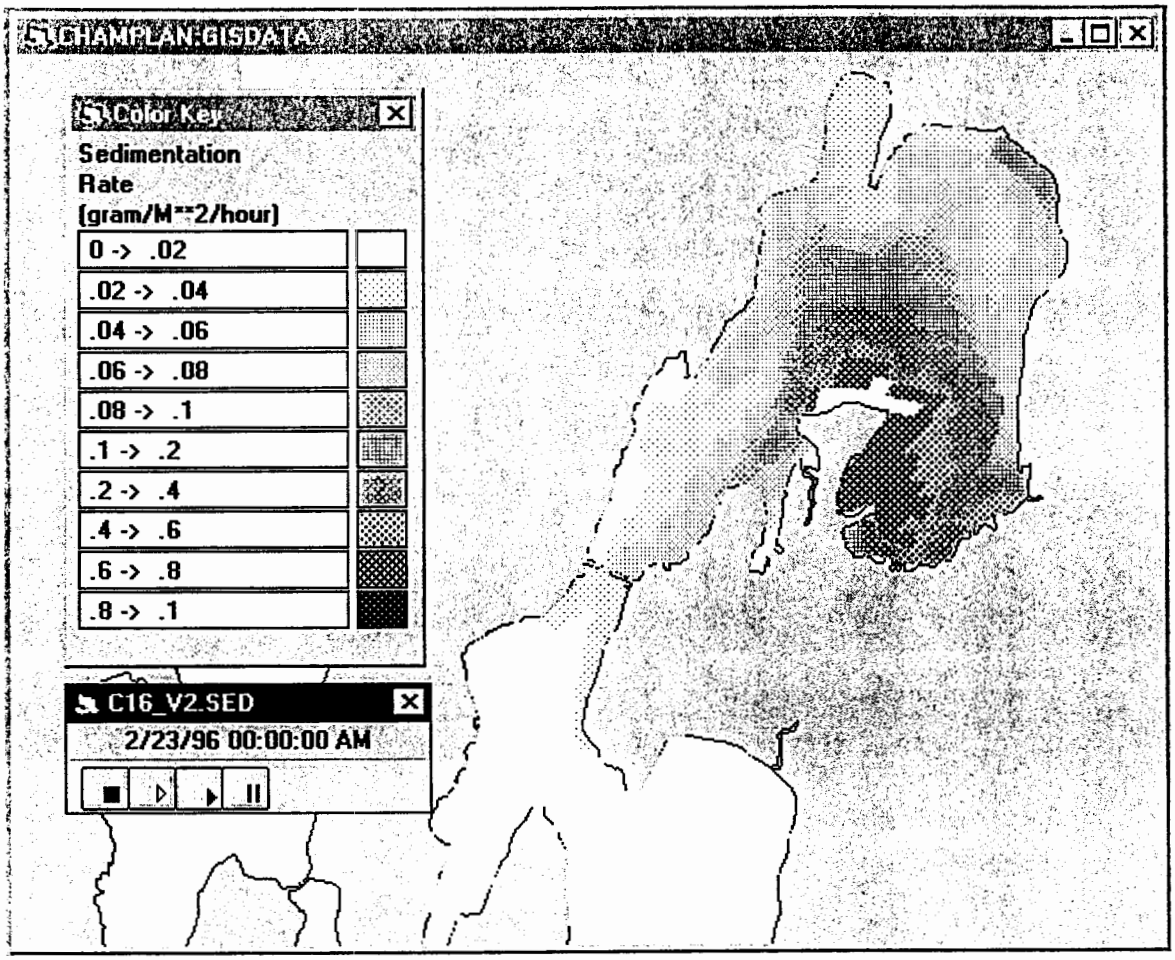

Figure 6.39 Plan view of the sedimentation rate for Case 16 (north wind with present causeway configuration).

The sedimentation rate difference plan view is shown in Figure 6.40. The picture here reflects the north winds ability to efficiently flush the bay, discovered in the flushing study (section 6.2). Most of the major differences occur outside of the bay in the passage to the west of and to the north of North Hero Island. Intersetingly results both positive and negative are seen both inside and outside of the bay making any difinitive conlusion difficult. The total sedimentation difference between the cases is also rather small at 0.1%.

Cases 20 and 21

The sedimentation rate for the Case 20 (east wind with the present causeway configuration) again displays the influence of the wind driven circulation as can be seen in Figure 6.41. The difference in sedimentation rate between the with and wihtout causeway cases (Figure 6.42) however is substantially different than any so far. Again the results are mixed with both positive and negative differences inside the bay. There is a large band of positive rate difference across the southern half of the bay and a correnspondingnegative difference across the mid section of the bay. In addition there is a large area of negative difference covering most of the area north of North Hero Island outside of the causeway.

Cases 28 and 29

For the no wind cases the sedimentation rate decreases smoothly as you move away from the river mouths as shown in Figure 6.43. This is the expected result and can be used to guage the wind driven effects on thr sedimentation rate shown in the previous cases. Sediment deposited from the effluent of the Missisquoi River also appears to hug the eastern shore of the passage to the causeway, (i.e. material emanating from the river is less likely to 'cross' the passage than it is to be deposited at some point on the path to the causeway.

The difference in deposition rate, shown in Figure 6.44, has some very interesting features. There appears to be a decrease in deposition in the bay by removing the causeway (i.e. positive sedimentation rate difference) not suprisingly following a path very similar to the deposition rate 'plume'. In addition the model also

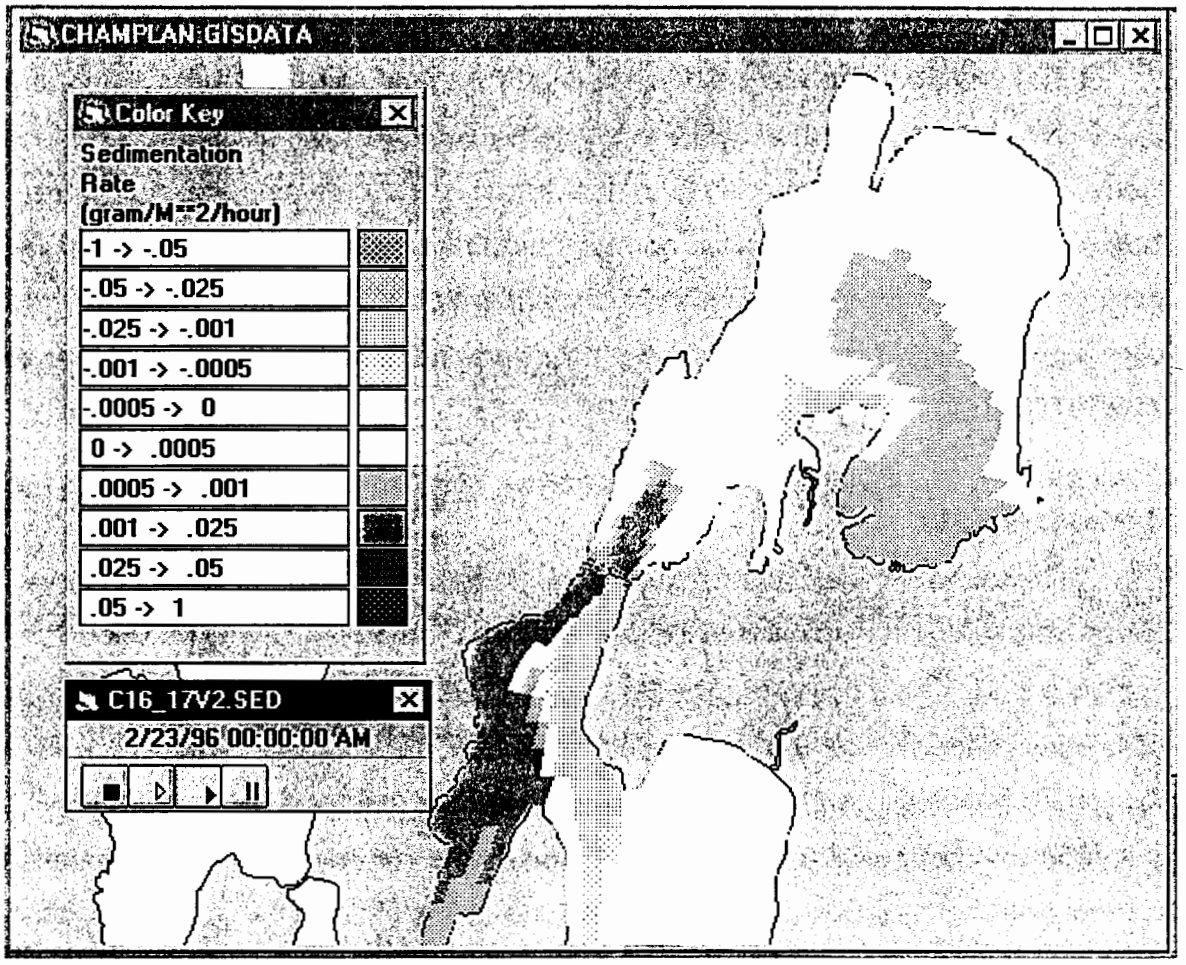

Figure 6.40 Plan view of the difference in sedimentation rate between Case 16 and Case 17 (north wind with and without the causeway, respectively).

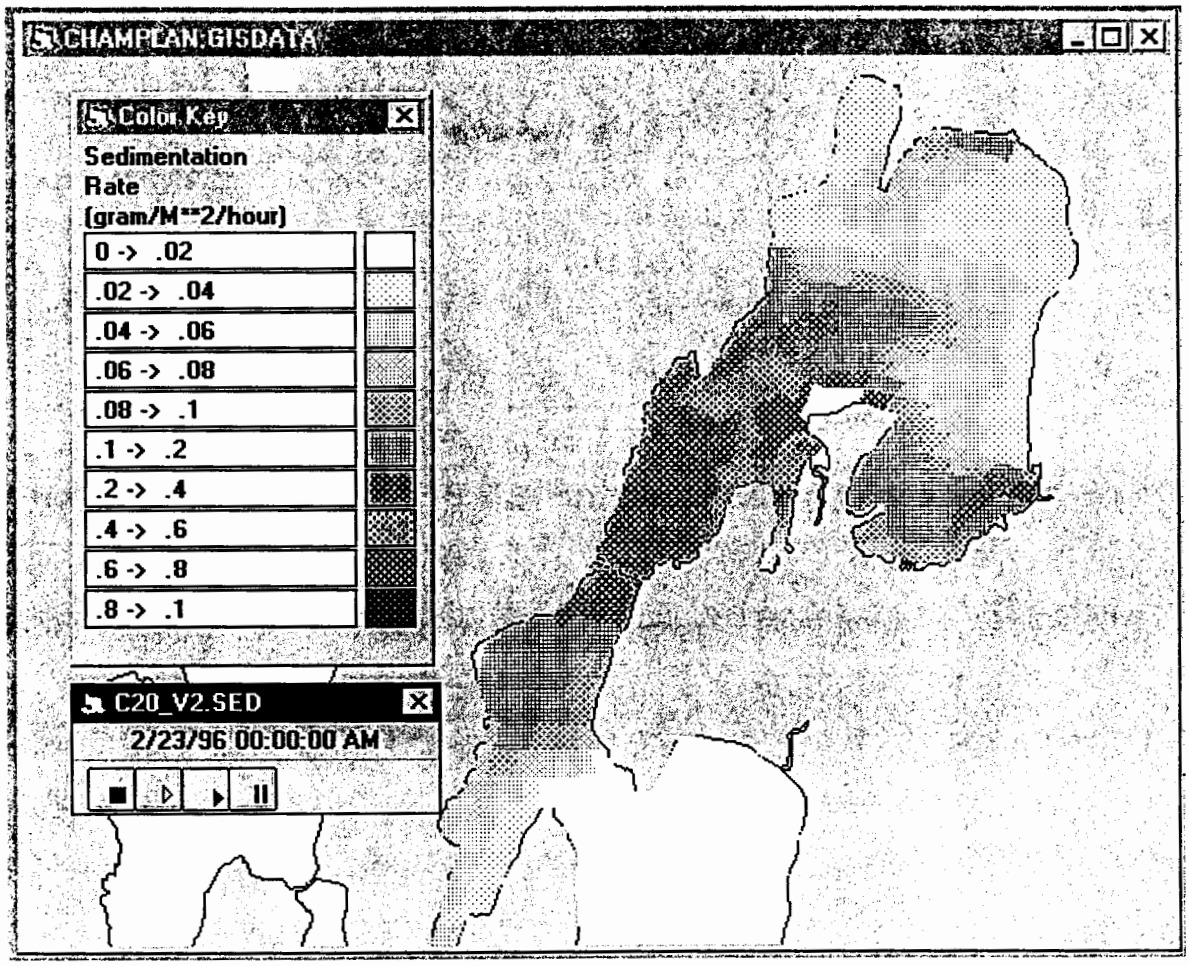

Figure 6.41 Plan view of the sedimentation rate for Case 20 (east wind with present causeway configuration).

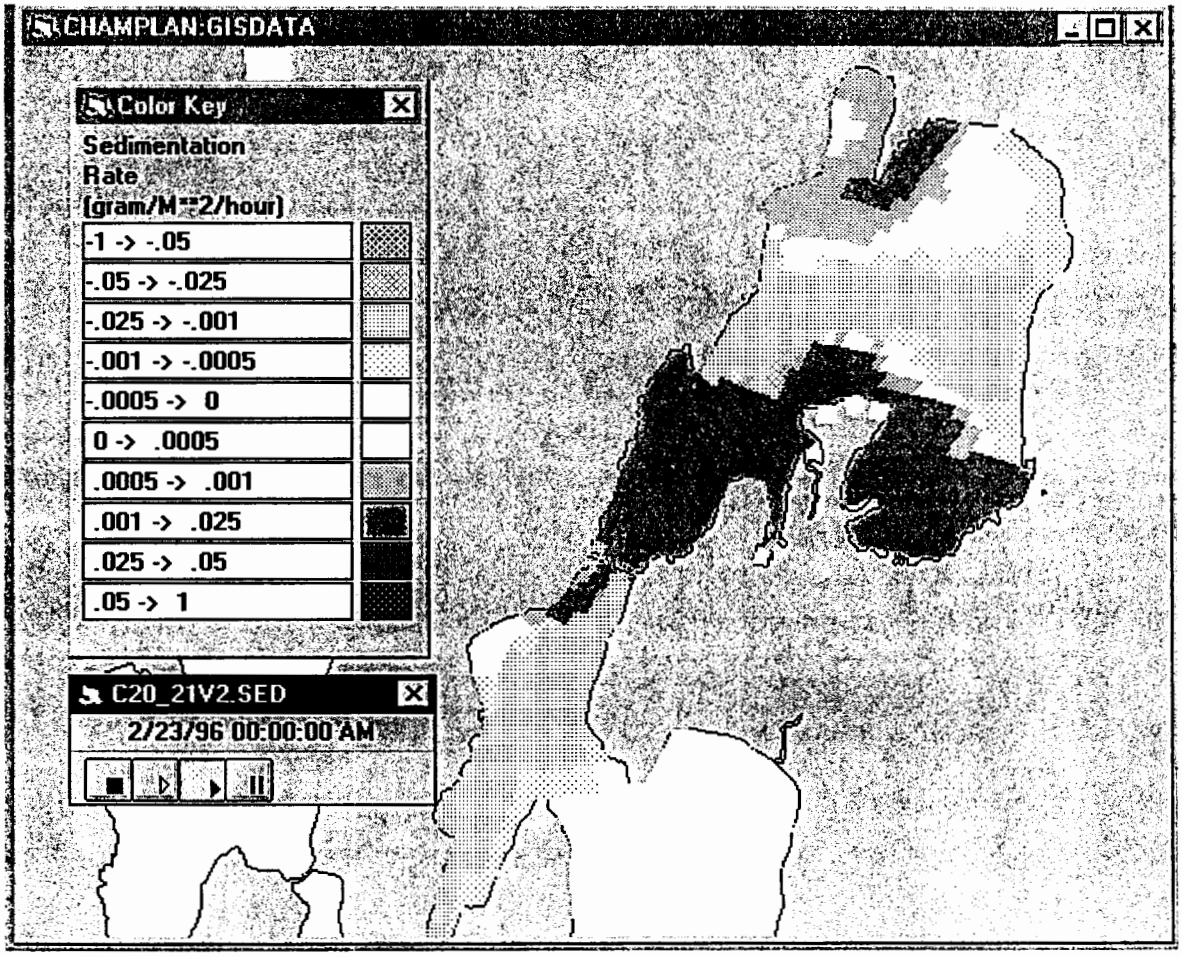

Figure 6.42 Plan view of the difference in sedimentation rate between Case 20 and Case 21 (east wind with and without the causeway, respectively).

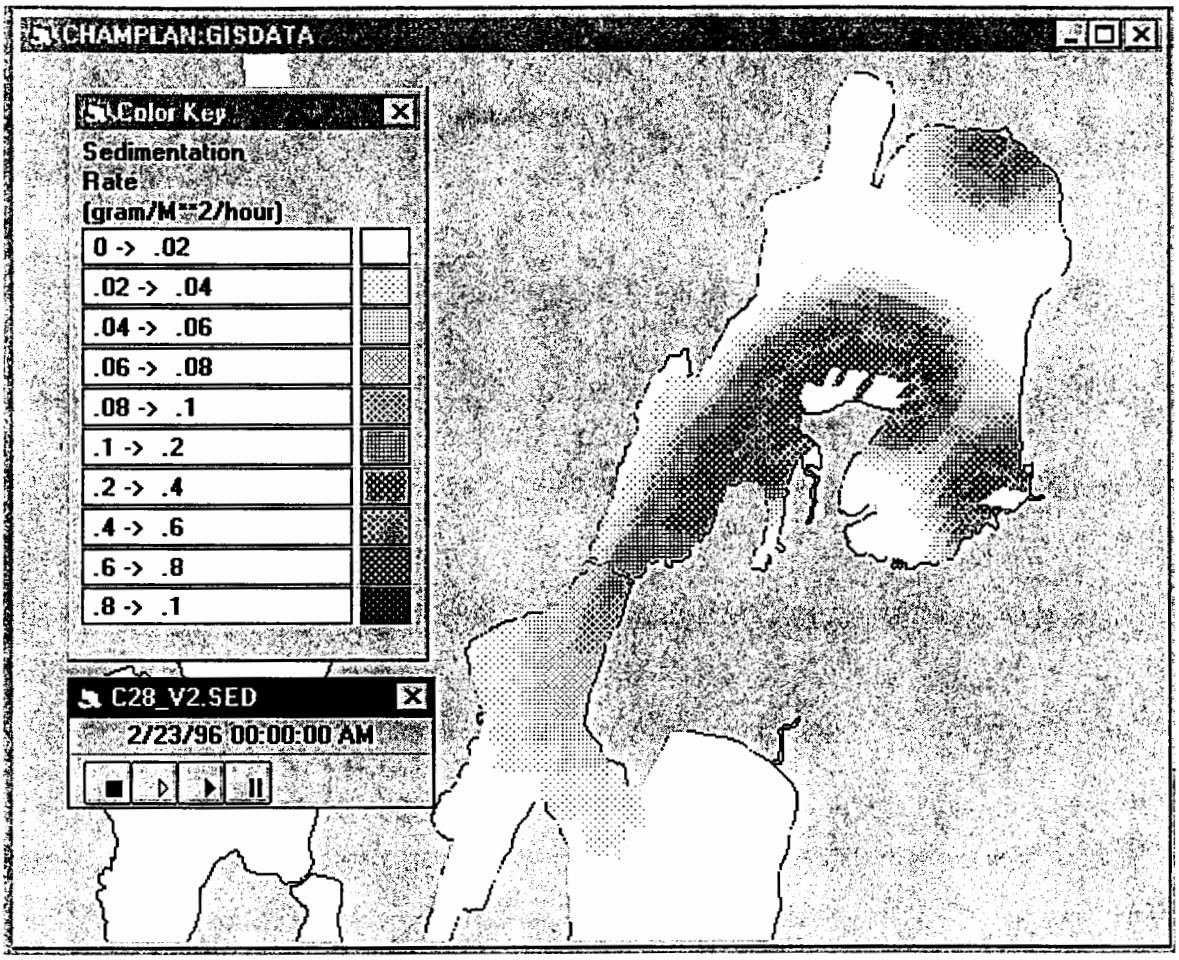

Figure 6.43 Plan view of the sedimentation rate for Case 28 (no wind with present causeway configuration).

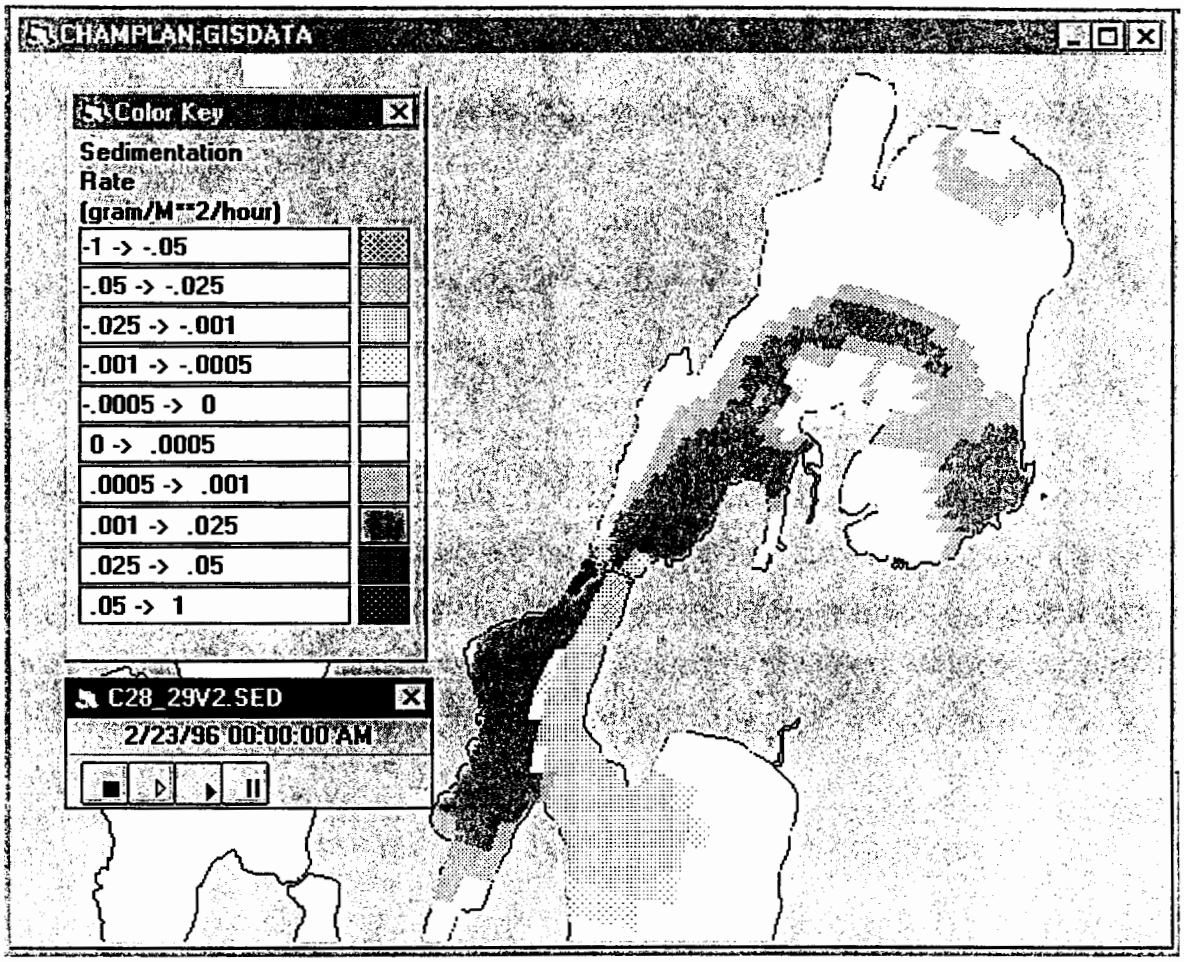

Figure 6.44 Plan view of the difference in sedimentation rate between Case 28 and Case 29 (no wind with and without the causeway, respectively).

predicts decrease in deposition outside of the causeway on the west side of the passage but a comperable increase in deposition on the east side of the passage north of North Hero Island. This difference appears to be split almost exactly down the middle of the passage. The difference between the total amount of material deposited for the with and without causeway cases is none the less only 0.2%.

Other Cases

Table 6.4 summarizes the effect of the directional variation of the wind on the sedimentation rate. Also shown are specific results from the wind speed variation tests as well as the settling rate variation tests on the base case. For the settling rate variation test, as can be expected the amount of material that escapes the bay rather than settles within the bay increases with decreasing settling rate. By halving the rate the percentage that settles within the bay jumps from approximately 5% to 25%.

Table 6.4 Model predicted sediment deposition rate and deposition rate difference as a function of wind direction.

Wind Direction	% Sediment Deposition in the bay with	without	difference
N	97.69	97.59	0.10
NE	83.62	82.73	0.89
E	85.18	84.58	0.60
SE	89.89	90.09	-0.20
SSW	93.63	93.35	0.28
SW	96.21	96.03	0.18
W	98.27	98.25	0.02
NW	97.99	97.89	0.10
High wind	96.12	95.10	1.02
Low wind	92.31	92.24	0.07

Fast settling	95.79 (0.4 m/day)
Mid settling	93.63 (0.2 m/day)
Slow settling	74.25 (0.1 m/day)

6.4 Phosphorus Model

The phosphorus model was run for the base case to begin to assess the effects of the various environmental forces on the on the phosphorus concentration in the bay. The output for the phosphorus model runs is set up in a manner similar to that for sediment transport runs; plan views of the vertically averaged water column phosphorus concentration after 40 days and a plan view of the difference in concentration between the with and without causeway cases.

Cases B1 and B2

The plan view of the vertically averaged water column concentration of phosphorus for the base case with the present causeway configuration (B1) is shown in Figure 6.45 and with the causeway completely removed (B2) is shown in Figure 6.46. There is a clear trend towards higher concentrations on the east side of the bay resulting from the relatively highly concentrated Rock River effluent. The Missisquoi, although it has a much larger river flow, has a significantly lower phosphorus concentration. The central portion of the bay maintains a concentration in the 20-30 µg/L range in the west to the 40-50 µg/L, with a strip of very high concentrations hugging the eastern shore. The mean in the bay is approximately 35 µg/L which agrees with the insitu concentrations reported in 'Lake Champlain diagnostic-feasibility study', (VTDEC & NYSDEC, 1994). It is not possible to discern any difference in the concentration between case B1 and B2 from the concentration maps shown as the magnitude of the difference is substantially smaller than the actual concentrations.

The difference in the vertically averaged phosphorus concentration between the with and without causeway cases is shown in Figure 6.47. As with the sedimentation rate difference plots a positive difference shows a decrease in concentration for the without causeway case. The differences in shown in Figure 6.47 are remarkably similar to those shown in the sedimentation rate base case comparison (Figure 6.36), here showing between a 0.5 µg/L and 2.0 µg/L decrease in phosphorus concentration in a thin strip along the west shore of the Missisquoi Bay entrance between the causeway

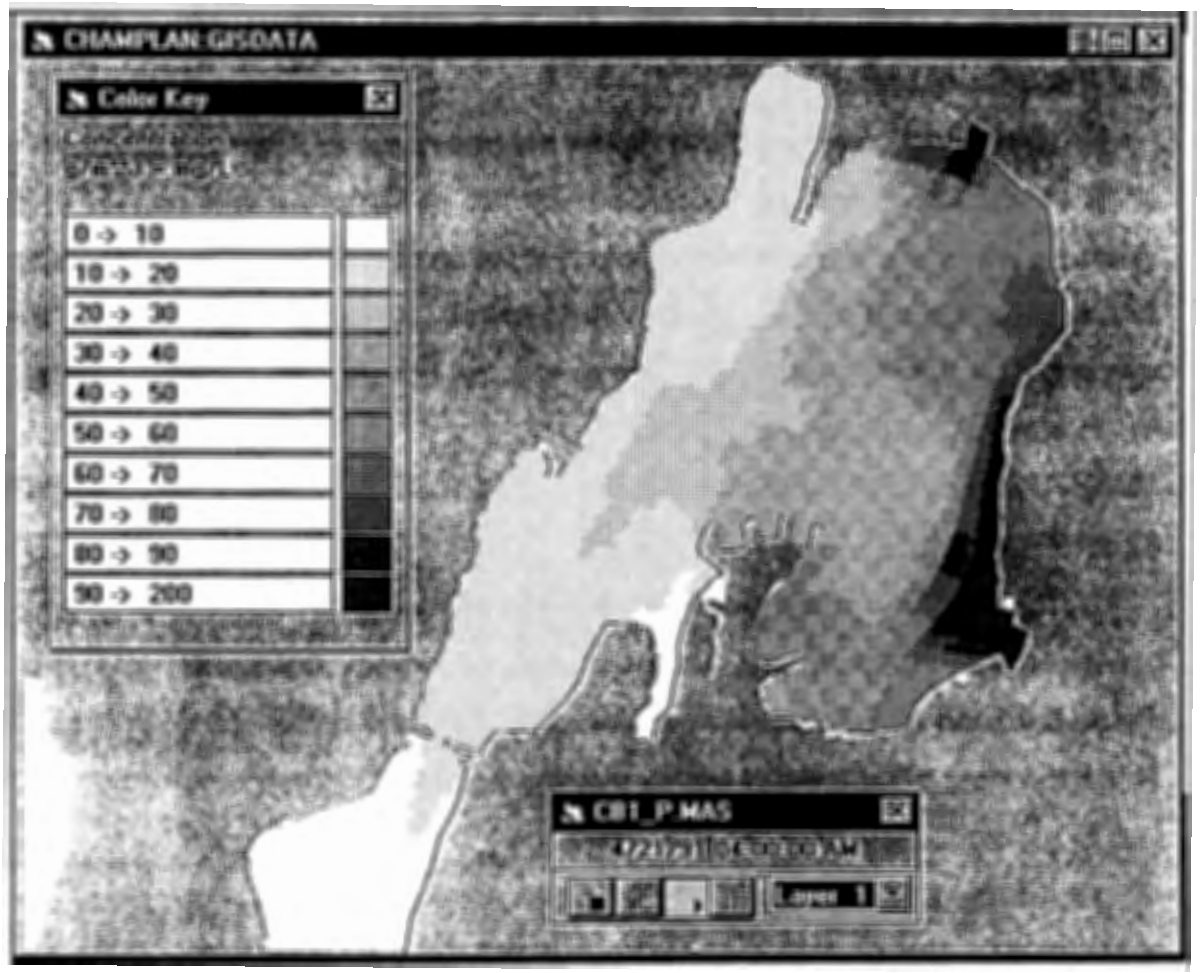

Figure 6.45 Plan view of vertically averaged water column phosphorus concentration for Case B1 (base case with the present causeway configuration).

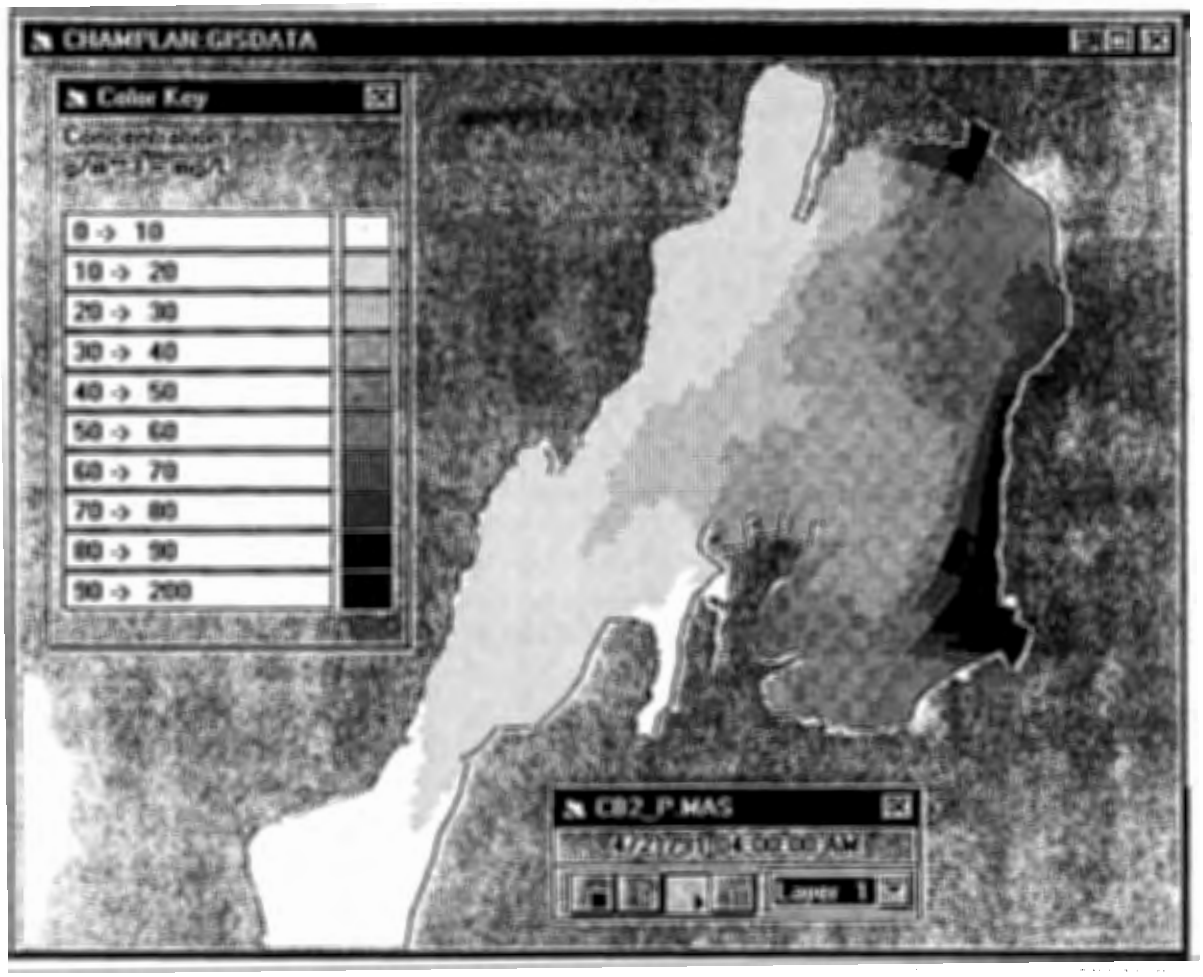

Figure 6.46 Plan view of vertically averaged water column phosphorus concentration for Case B2 (base case with the causeway completely removed).

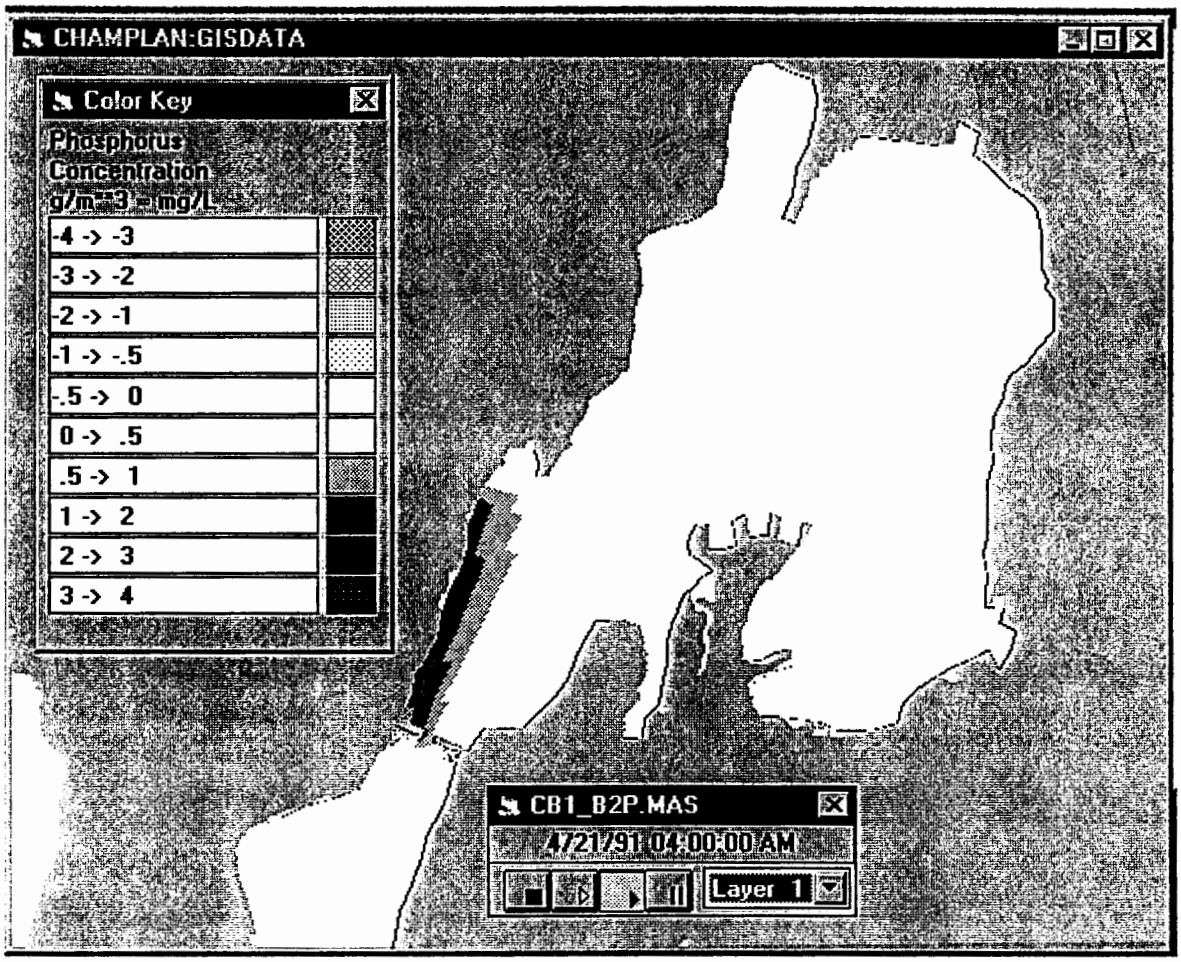

Figure 6.47 Plan view of the difference in vertically averaged water column phosphorus concentration between Case B1 and Case B2 (base case with and without causeway, respectively).

and Chapman Bay. There is also a corresponding (although slightly larger) increase in concentration in the immediate vicinity of the causeway for the without causeway case.

7. DISCUSSION AND CONCLUSIONS

Using a set of hydrodynamic and constituent transport models based on a boundary fitted coordinate model system a matrix of test cases were run to evaluate the response of Missisquoi Bay to environmental forces. These cases included variations of environmental conditions (winds and river flow) and bridge geometries. The matrix of simulations and anlysis of the results were aimed at determining how these forces affect flushing, sediment transport and deposition and phosphorus concentrations in the bay with the causeway as it is now and to predict and compare those results with a similar set simulating the condiftions should the causeway be removed.

Hydrodynamic Model Case Summary

There are a few very distinct pattens that emerge as characteristic of the currents in Missisquoi Bay. For the wind driven cases currents in the shallow areas along the shorelines uniformly respond with the wind, flowing in the direction of the wind. This is also true, but to a lesser extent, of the surface layer in general, with the exception of the deeper areas where return flow is often found. The lower layer of the main portion of the bay on the other hand almost uniformly presents a flow counter to the wind direction.

The exception to these patterns is in the lower south west section of the bay defined by the area north of the causeway and south of Chapman Bay, west of the Missisquoi River delta. In this region the currents are often strong and variable and circulation cells appear in several of the cases (north and south winds).

For calm (no wind) conditions the river flow generated currents are very small in the main portion of the bay but increase in the lower portion of the bay near the causeway as the cross sectional area through which it flows decreases. For the steady wind cases (all but the real wind cases) the steady net flow through the causeway opening is equivalent to the river flow.

For a few cases, for example the south and southwest wind cases with the causeway removed, the exchange through the causeway area appears to be increased somewhat by the northward flowing components in the shallower areas along the shore. The flushing and sediment transport studies will evaluate how much difference the apparent increase in exchange makes.

Although some rather substantial circulation differences are experienced between sets of cases, corresponding to changes in wind speed and direction and river flow rate, very little difference is found between the with and without causeway cases. A speed difference analysis comparing the with and without causeway cases found that the variations between the cases is confined to a thin strip approximately 200 meters wide both north and south of the causeway. This finding proposes that the causeway does not hydraulically restrict the water flow between Missisquoi Bay and the Northeast Arm. Water does not 'pile up' behind the causeway for any of the cases tested. The causeway then merely represents an obstacle that the water must go around.

The localized differences in the velocities are generally not sufficient to result in additional sediment resuspension. In general velocities in the region of the causeway would be decreased from the resulting increase in cross-sectional area if the causeway were removed.

Flushing Model Case Summary

An indicator of the differences among cases is the model predicted flushing time (described under case B1 above), which are summarized in Table 6.1, for each of the 33 cases. The range of flushing times is from 14.3 days for Case 19 (north wind with the causeway completely removed) to 105.8 days for Case 31 (low river flow with present causeway configuration) . These flushing times are an indication of how fast the bay will flush under the various environmental conditions, and more importantly how the presence or absence of the causeway affects the flushing under those environmental conditions.

It is clear from the results of the wind direction variation analysis that the direction the wind is blowing from is extremely important to the flushing of the bay.

These differences are due to the flow patterns that develop within the bay, specifically, flushing appears to increase if currents carry water with higher concentrations towards the causeway and the river flow, with its lower concentration is carried away. If on the other hand the river plumes (particularly from the Missisquoi) are directed out of the bay, as with the south west wind, then the higher concentration water is less effectively flushed. From the perspective of flushing material that is suspended in the water of the bay at large, Missisquoi Bay is subject to the unfortunate coincidence that it experiences the least effective flushing from winds that originate from the southern end of the bay, which is the predominant wind direction. Conversely, a prolonged south west wind would apparently act to direct suspended sediments entering the bay from the Missisquoi River on a path out of the bay.

With the exception of the east wind case (Cases 20 and 21), the wind comparison cases show a slight decrease in the flushing time for all of the 'without causeway' cases when compared to the identical 'with causeway' cases. The differences ranged from a 0.6 day (2.5%) increase for the east wind case to an 8 day (23%) decrease in flushing time between the 30 mph wind cases (Cases 5 and 6). The flushing time also appears to increase (as does the difference between cases) with increasing wind speed, (Cases B1, B2, 3, 4, 5, 6).

Lower river flows cause significant increases in the model predicted flushing time as well as increases in the difference between with and without causeway configurations. For example, the low river flow case shows a decrease in flushing time of 53.2 days (50%) for the case with no causeway compared to the case with the causeway, where the base case difference is on the order of 1 day (5%). The implications of the results are that as the river flow decreases the width of the opening at the causeway becomes increasingly important. From the perspective of actual flushing time though, even the smaller flushing time of the no causeway case is two to three times as long as the other cases. The differences between cases may therefore pale to insignificance when integrated into the ensemble flushing response of the bay to varied conditions. These differences are only exaggerated for the no river flow cases.

Sediment Transport Case Summary

For most of the cases the sediment released from the three rivers deposits within the bay. Only a small portion of the material actually leaves the bay as can be seen by reviewing the calculated percentages presented in Table 6.3. In general the sedimentation rate patterns agree with the flushing model concentration patterns. In addition the percentages of sediment deposition within the bay have a similar distribution with wind direction as the flushing times; winds coming from the northeasterly directions favor flushing/transport out of the bay whereas the southwesterly directions inhibit them. The higher the flushing (i.e. the smaller the flushing time) the lower the deposition within the bay as exhibited by the cases with the wind coming from the northern half of the bay. The numerical difference between the with and without causeway cases also increases for these cases however the increase is not substantial. This trend may be more noticeable for slower settling sediments approaching the flushing case with decreasing settling rate.

Trends in the local deposition rate differences are difficult to generalize other than to say that a decreased deposition rate in one portion of the lake is accompanied by an increased rate in another. The difference in sedimentation rate between the with and without causeway cases is substantially smaller than the sedimentation rate variability with wind direction.

The most notable local differences in the sediment deposition rate between the with and without causeway cases occur in the areas (near the causeway) where higher concentrations of sediment move into areas with lower current speeds in the 'with causeway' case where higher currents may develop if the causeway were to be removed.

Phosphorus Model Case Summary

The model predicted distribution shown for case B1 may or may not accurately reflect the actual concentration distribution within the bay in that the base case, although representative of mean conditions in the bay, is a steady state solution. On the other hand if it can be assumed that the concentrations and river flows are

representative of prevailing conditions then this distribution or some variation thereof will probably hold.

The generalizations that can be made regarding the model predicted phosphorus concentrations are that the magnitude of the total difference between the with and without causeway cases is small and is similar to the those predicted for both the flushing and sediment transport studies for similar cases. In addition the concentration difference pattern is very much like the sedimentation rate difference pattern for the same case. These generalizations can most likely be extrapolated to the other cases in the matrix.

Conclusions

The following conclusions summarize the results of the four model applications taken together and generalize some of the more important findings.

- For the majority of the cases, with a few exceptions, there is a persistent but small improvement in the flushing and sedimentation for cases with the causeway completely removed over the cases with the present causeway configuration.

- Differences between the cases with the present causeway configuration and cases with the causeway completely removed, when they do occur, are generally confined to the region in the vicinity of the causeway, bounded for the most part by North Hero Island in the south and Chapman Bay to the north.

- Differences in the velocities are generally not sufficient to result in additional sediment resuspension. In general velocities in the region of the causeway would be decreased from the resulting increase in cross-sectional area if the causeway were removed.

- Differences between the with and without causeway cases are substantially smaller than differences caused by variations in the environmental forces.

- Flushing and sedimentation differences caused by variations in the river flow rates are the most sensitive to the cross-sectional area at the causeway. As river flow decreases, the flushing time increases and the difference between with and without causeway cases increases, increasing flushing time for the present causeway configuration.

- Decreases in concentration of constituent within the bay were matched by increases in concentration (although generally mode distributed) in the Northeast Arm.

- Decreases in sedimentation within the bay were matched by increases of sedimentation in the Northeast Arm.

8. REFERENCES

Davis, Richard A., 1983. Depositional Systems. Prentice-Hall, Inc., Englewood Cliffs, New Jersey. 07632.

Hunt, A.S., 1971. Bottom sediments of Lake Champlain, 1965-1971: A completion report to the Office of Water Resources and U.S. Department of Interior, University of Vermont, Burlington VT, 127 pp.

Madala, R.V. and S.A. Piascek, 1977. A semi implicit numerical model for Baroclinic Oceans. Journal of Computational Physics, 23, pp. 167-178.

Mendelsohn, D.L., T. Isaji, and H. Rines, 1994. Hydrodynamic and water quality modeling of Lake Champlain. Final report to Lake Champlain. US Environmental Protection Agency, Region I, Boston, MA and Region II, New York, NY.

Mendelsohn, D.L. and H.M. Rines, 1995. Development and application of a full phosphorous cycle water quality model to Lake Champlain. In Modern Methods for Modeling the Management of Stormwater Impacts. William James (ed.) Compiled and published by Computational Hydraulics International.

Mendelsohn, D.L. and J.C. Swanson, 1992. Application of a Boundary Fitted Coordinate Mass Transport Model, Estuarine and Coastal Modeling. Proceedings of the 2nd International Conference. ed. Malcolm Spaulding, ASCE.

Mendelsohn, D.L., E. Howlett and J. C. Swanson, 1995. WQMAP in a Windows environment. Presented at Estuarine and Modeling IV. Proceedings of the 4th International Conference, ASCE, San Diego, October 26-28, 1995.

Muin, M., and M.L. Spaulding, 1996(In review). A 3-D boundary fitted circulation model. Submitted to the ASCE J. of Hydraulic Engineering.

Muin, M. and M.L. Spaulding, 1993. Development and application of a three-dimensional boundary-fitted model in Providence River. Presented at the

Estuarine and Coastal Modeling III. Proceedings of the 3rd International Conference, Oak Brook, Illinois, September 8-10, 1993.

Muin, M., 1993. A three-dimensional boundary fitted circulation model in spherical coordinates. PhD Dissertation, University of Rhode Island.

Muin, M., 1993. A three-dimensional boundary fitted circulation model in spherical coordinates. Ph.D. Dissertation, Dept. of Ocean Engineering, University of Rhode Island, Narragansett, RI.

Myer, G.E. and G.K. Gruendling, 1979. Limnology of Lake Champlain. Prep for New England River Basins Commission. Burlington, VT.

New York State Department of Environmental Conservation, New York State Biological Survey, and Vermont Department of Environmental Conservation, 1992. Work/QA Project Plan. Long-term water quality and biological monitoring project for Lake Champlain. Prep. for U.S. Environmental Protection Agency. Regions I and II. Albany, NY and Waterbury, CT.

Smeltzer, E, 1994. Vermont Route 78 Swanton-Alburg bridge project water quality assessment update. Vermont Agency of Natural Resources, Department of Environmental Conservation, Water Quality Division, Waterbury, VT.

Spaulding, M.L., 1984. A vertically averaged circulation model using boundary-fitted coordinates. Journal of Physical Oceanography, 14, p. 973-982.

Swanson, J.C. and D.L. Mendelsohn, 1994. Application of a Water Quality Modeling, Mapping and Analysis System to Evaluate Effects of CSO Abatement Alternatives on Upper Narragansett Bay, Rhode Island. 1994 Water Environment Federation CSO Specialty Conference, Louisville, Kentucky, July 1994.

Swanson, J.C., 1986. A three dimensional numerical model system of coastal circulation and water quality. PhD Dissertation, University of Rhode Island.

Swanson, J.C., 1986. A three-dimensional numerical model system of coastal circulation and water quality. Ph.D. Dissertation, Department of Ocean Engineering, University of Rhode Island, Kingston, Rhode Island.

Swanson, J.C., M. Spaulding, J.P. Mathisen, O.O. Jenssen, 1989. A three dimensional boundary fitted coordinate hydrodynamic model: Part I, Development and testing. Deutsche Hydrographische Zeitschrift, 42, H.3-6, pp. 170-186.

Vermont Department of Conservation and New York State Department of Environmental Conservation, 1994. Lake Champlain diagnostic-feasibility study,

Final Report, Part 1: A phosphorus budget, model and load allocation for Lake Champlain. US Environmental Protection Agency, Region I, Boston, MA and Region II, New York, NY.

Vermont Department of Conservation and New York State Department of Environmental Conservation, 1992. Lake Champlain diagnostic-feasibility study, Interim Progress Report. US Environmental Protection Agency, Region I, Boston, MA and Region II, New York, NY.

Appendix A Wind Statistics for Philipsburg, Quebec, Station 702604. Direction de l'hydraulique, Ministere de l'Environnement.

DIRECTION DES RESEAUX ATMOSPHERI

STATISTIQUES SUR LES VENTS
OBSERVATIONS A 8H ET 18H (HNE)

STATION : 7026040 (R - 6)
PERIODE : 1977-1989

NOM : PHILIPSBURG
SEQUENCE: 239150

ROSE DES VENTS
FREQUENCE PAR DIRECTION

	NORD	NE	EST	SE	SUD	SW	WEST	NW	CALM	
JANVIER	11.45	3.07	4.33	6.15	20.53	11.31	16.06	6.98	20.11	
FEVRIER	9.34	3.16	3.59	3.45	16.38	12.64	22.56	7.76	21.12	
MARS	12.41	4.47	4.71	3.72	18.61	9.80	15.14	9.18	21.96	
AVRIL	12.05	5.34	3 56	4.79	14.79	12.19	16.71	8.90	21.64	
MAI	9.93	4.90	3.40	4 08	21.09	11.56	14.83	6.26	23.95	
JUIN	7.05	2.53	3.19	5.19	24.07	12.23	18.35	8.38	19.02	
JUILLET	4.94	0.89	2.28	7.72	27.59	11.52	13.80	7.09	24.18	
AOUT	5.11	1.53	3.70	4.34	22.09	11.75	13.15	7.02	31.29	
SEPTEM	5.74	1.83	2.74	6.13	21.90	12.65	15.78	9.65	23.60	
OCTOBR	11.28	1.50	4.14	5.01	19.92	12.41	15.41	7.27	23.06	
NOVEMB	10.64	2.33	4.93	6.74	21.14	12.71	14.92	8.17	18.42	
DECEMB	9.67	3.94	7.00	7.89	19.85	10.81	13.99	7.12	19.72	
ANNUEL	9.11	2.94	3.98	5.45	20.72	11.79	15.82	7.82	22.38	100.01
HIVER	10.15	3.41	5.05	5.91	18.97	11.56	17.38	7.28	20.29	
PRINTEM	11.49	4.89	3.92	4.18	18.19	11.14	15.54	8.15	22.50	
ETE	5.68	1.63	3.05	5.76	24.60	11.83	15.05	7.48	24.90	
AUTOMN	9.25	1.88	3.94	5.95	20.98	12.59	15.37	8.35	21.70	

OCCURENCE DES OBSERVATIONS

X	NORD	NE	EST	SE	SUD	SW	WEST	NW	CALM	TOT
JANVIER	82	22	31	44	147	81	115	50	144	716
FEVRIER	65	22	25	24	114	88	157	54	147	696
MARS	100	36	38	30	150	79	122	74	177	806
AVRIL	88	39	26	35	108	89	122	65	158	730
MAI	73	36	25	30	155	85	109	46	176	735
JUIN	53	19	24	39	181	92	138	63	143	752
JUILLET	39	7	18	61	218	91	109	56	191	790
AOUT	40	12	29	34	173	92	103	55	245	783
SEPTEM	44	14	21	47	168	97	121	74	181	767
OCTOBR	90	12	33	40	159	99	123	58	184	798
NOVEMB	82	18	38	52	163	98	115	63	142	771
DECEMB	76	31	55	62	156	85	110	56	155	786
ANNUAL	332	268	363	498	1892	1076	1444	714	2043	9130
HIVER	223	75	111	130	417	254	382	160	446	2198
PRINTEM	261	111	89	95	413	253	353	185	511	2271
ETE	132	38	71	134	572	275	350	174	579	2325
AUTOMN	216	44	92	139	490	294	359	195	507	2336

DIRECTION DES RESEAUX ATMOSPHERIQUES

STATISTIQUES SUR LES VENTS
OBSERVATIONS A 8H ET 18H (HNE)

STATION : 7026040 (R - 6)
PERIODE : 1977-1989

NOM : PHILIPSBURG
SEQUENCE: 239150

VITESSE MOYENNE PAR DIRECTION (KM/H)

X	NORD	NE	EST	SE	SUD	SW	WEST	NW	VIT.MOY	C.M.VIT.	TOT.OBS	ECT.TYP	CO.VAR
JUANVIE	14.22	14.93	15.46	15.76	18.23	15.37	15.02	15.49	12.7	274.7	716	10.65	83.84
FEVRIER	14.66	15.97	12.75	18.96	15.32	17.48	14.55	14.61	12.12	245.4	696	9.92	81.88
MARS	14.91	15.83	13.16	18.63	17.81	17.39	17.25	17.02	13.06	286.69	806	10.77	82.48
AVRIL	13.91	14.85	15.6	18.1	15.59	17.21	17.44	16.16	12.65	259.68	730	9.98	78.87
MAI	14.09	14.57	16.4	15.17	19.43	17.72	16.97	16.2	12.97	274.58	735	10.32	79.57
JUIN	16.21	15.15	14.09	16.71	18.29	16.21	16.58	16.27	13.63	292.7	752	10.34	75.81
JUILLET	14.33	15.31	12.93	14.84	16.11	16.64	15.32	16.15	11.9	232.37	790	9.52	79.98
AOUT	14.34	14.83	11.24	14.74	16.58	14.02	15.26	15.09	10.39	203.18	783	9.75	93.85
SEPTEM	15.26	15.29	13.35	17.17	18.72	17.01	14.19	16.32	12.64	262.99	767	10.16	80.41
OCTOBR	15.15	17.86	13.42	16.4	18.7	17.62	15.55	17.35	12.92	281.8	798	10.72	82.92
NOVEMB	13.78	9.27	10.35	11.83	19.91	19.11	17.01	15.9	13.47	313.16	771	11.48	85.25
DECEMB	11.83	13.73	13.06	15.58	18.28	17.19	15.55	18.49	12.81	284.3	786	10.97	85.64
ANNUEL	14.32	14.73	13.35	15.86	17.81	16.93	15.87	16.29	12.6	267.71	9130	10.43	82.78
HIVER	13.53	14.74	13.66	16.26	17.45	16.71	14.98	16.24	12.56	268.85	2198	10.55	84
PRINTEM	14.34	15.08	14.78	17.34	17.83	17.44	17.23	16.51	12.9	274.09	2271	10.38	80.45
ETE	15.09	15.08	12.63	15.36	16.95	15.62	15.8	15.86	11.95	242.05	2325	9.96	83.29
AUTOMN	14.65	13.53	12.13	14.95	19.11	17.92	15.56	16.49	13.01	285.98	2336	10.81	83.06

OCCURENCE DES OBSERVATIONS
FREQUENCE DES VITESSES PAR CLASSE

X	NORD	NE	EST	SE	SUD	SW	WEST	NW	CALM	V<6	6-12	12-20	20-29	29-39	V>39
JANVIER	82	22	31	44	147	81	115	50	144	29.89	22.91	25.28	12.85	6.15	2.93
FEVRIER	65	22	25	24	114	88	157	54	147	27.87	24.57	29.31	11.93	4.02	2.3
MARS	100	36	38	30	150	79	122	74	177	28.16	19.98	27.92	15.88	5.21	2.85
AVRIL	88	39	26	35	108	89	122	65	158	27.53	21.51	26.99	18.63	3.56	1.78
MAI	73	36	25	30	155	85	109	46	176	29.8	17.14	26.8	18.78	5.99	1.5
JUIN	53	19	24	39	181	92	138	63	143	24.87	20.48	26.86	19.02	7.18	1.6
JUILLET	39	7	18	61	218	91	109	56	191	29.49	20.76	29.75	14.56	4.81	0.63
AOUT	40	12	29	34	173	92	103	55	245	37.68	21.58	23.88	12.13	3.58	1.15
SEPTEM	44	14	21	47	168	97	121	74	181	30.38	18.9	24.25	19.04	6.39	1.04
OCTOBR	90	12	33	40	159	99	123	58	184	30.95	19.05	22.06	19.8	6.39	1.75
NOVEMB	82	18	38	52	163	98	115	63	142	26.33	25.94	23.48	14.66	6.23	3.37
DECEMB	76	31	55	62	156	85	110	56	155	29.26	25.06	24.55	11.07	6.23	3.82
ANNUEL	832	268	363	498	1892	1076	1444	714	2043	29.39	21.47	25.89	15.71	5.49	2.06
HIVER	223	75	111	130	417	254	382	160	446	29.03	24.2	26.3	11.92	5.51	3.05
PRINTEM	261	111	89	95	413	253	353	185	511	28.49	19.55	27.26	17.7	4.93	2.07
ETE	132	38	71	134	572	275	350	174	579	30.75	20.95	26.84	15.18	5.16	1.12
AUTOMN	216	44	92	139	490	294	359	195	507	29.24	21.28	23.24	17.85	6.34	2.05

Appendix B Muin, M., and M.L. Spaulding, 1997. A 3-D boundary fitted circulation model. Published in the Journal Of Hydraulic Engineering, January 1997.

THREE-DIMENSIONAL BOUNDARY-FITTED CIRCULATION MODEL

By Muslim Muin[1] and Malcolm Spaulding[2]

ABSTRACT: A spherical coordinate, three-dimensional, nonorthogonal, boundary-fitted circulation model (contravariant formulation) for application to estuarine, coastal sea, and continental shelf waters is presented. The model employs a split mode technique where the equations are decomposed into exterior and interior modes. The exterior mode (vertically averaged) described in an earlier paper (Muin and Spaulding 1996) is solved using a semiimplicit solution technique. The interior mode (vertical structure) is solved explicitly, except for the vertical diffusion terms that are solved implicitly. The temporally and spatially varying eddy viscosity and diffusivity are determined from a turbulent kinetic energy equation and an empirically specified length scale. A series of tests are presented to evaluate model performance where analytical solutions or other numerical solutions are available for comparison. The model's ability to predict the point vertical structure of tidal flow is tested against analytic solutions employing (1) constant viscosity; and (2) an eddy viscosity varying linearly with depth with a no-slip bottom boundary condition. The ability of the model to simulate three-dimensional tidal flow was tested against an exact solution for an annular section channel with quadratically varying bathymetry. The model was also tested against analytic solutions for steady residual flow generated by density gradient, wind, and river flow in a channel. The model predicted turbulent energy distributions generated from a bottom boundary were compared to those from a previous numerical study by Davies and Jones (1990). No-slip and bottom stress formulations at the sea bed, and their effect on the vertical structure of the flow are analyzed. The model was used to predict the salinity distribution in a simple rectangular channel identical to the Rotterdam Waterway. The computational method is very economical, stable, and accurate with the CFL stability condition up to 100.

INTRODUCTION

Numerical modeling techniques are routinely used to study circulation and pollutant transport in estuarine and coastal waters. The majority of models employ finite-difference techniques on square grid systems. While this has proven useful in various applications, it becomes expensive when the study region is geometrically and bathymetrically complex. Such difficulties motivate the use of alternative solution approaches that allow flexibility in the grid specification, for example finite elements (Lynch and Werner 1987) and boundary-fitted coordinates (Johnson 1980; Spaulding 1984; Sheng 1986; Swanson 1986; Muin and Spaulding 1996).

This paper presents the extension of a two-dimensional (2D) vertically averaged, boundary fitted, spherical coordinate circulation model developed by Muin and Spaulding (1996) to three dimensions. The paper first presents the governing equations in spherical coordinates with appropriate assumptions and boundary conditions. The equations are further transformed to a σ-coordinate. This is followed by presentations of the governing equations in a generalized curvilinear coordinate system, turbulence parameterization, the solution methodology, and model testing for which analytic (linear problems) solutions or other numerical solutions are readily available. Testing emphasizes calculations of the vertical structure of the flow. Testing of the 2D vertically averaged version of the model for a series of horizontal flow problems (see Lynch and Gray 1978) was presented in Muin and Spaulding (1996).

GOVERNING EQUATIONS

Using a spherical coordinate system, where ϕ = longitude positive east; θ = latitude positive north; and r = positive up, the equations of continuity, momentum, and conservation of substance can be written as

Continuity

$$\frac{1}{r\cos\theta}\frac{\partial u}{\partial \phi}+\frac{1}{r}\frac{\partial v}{\partial \theta}-\frac{v}{r}\tan\theta+\frac{1}{r^2}\frac{\partial r^2 w}{\partial r}=0 \tag{1}$$

Momentum

ϕ-direction

$$\frac{\partial u}{\partial t}+\frac{u}{r\cos\theta}\frac{\partial u}{\partial \phi}+\frac{v}{r}\frac{\partial u}{\partial \theta}-\frac{uv}{r}\tan\theta+w\frac{\partial u}{\partial r}+\frac{uw}{r}-fv$$
$$=-\frac{1}{\rho_o r\cos\theta}\frac{\partial p}{\partial \phi}+\frac{\partial}{\partial r}\left(A_v\frac{\partial u}{\partial r}\right) \tag{2}$$

θ-direction

$$\frac{\partial v}{\partial t}+\frac{u}{r\cos\theta}\frac{\partial v}{\partial \phi}+\frac{v}{r}\frac{\partial v}{\partial \theta}+\frac{uu}{r}\tan\theta+w\frac{\partial v}{\partial r}+\frac{vw}{r}+fu$$
$$=-\frac{1}{\rho_o r\cos\theta}\frac{\partial p}{\partial \theta}+\frac{\partial}{\partial r}\left(A_v\frac{\partial v}{\partial r}\right) \tag{3}$$

r-direction

$$\frac{\partial p}{\partial r}=-\rho g \tag{4}$$

Conservation of Substance

$$\frac{\partial q}{\partial t}+\frac{u}{r\cos\theta}\frac{\partial q}{\partial \phi}+\frac{v}{r}\frac{\partial q}{\partial \theta}+w\frac{\partial q}{\partial r}=\frac{\partial}{\partial r}\left[D_v\left(\frac{\partial q}{\partial r}\right)\right]$$
$$+\frac{D_h}{r^2}\left[\frac{\partial^2 q}{\cos^2\theta\,\partial\phi^2}+\frac{\partial^2 q}{\partial\theta^2}\right] \tag{5}$$

Equation of State of Sea Water

$$\rho=f(S,\Theta) \tag{6}$$

where t = time; u, v and w = velocity components in ϕ, θ, and r directions, respectively; f = Coriolis parameter; p = pressure; g = gravity; ρ = water density; ρ_o = basin-averaged water density; A_v = vertical eddy viscosity; D_v = vertical eddy diffusiv-

[1]Jurusan Teknik Sipil, Institut Teknologi Bandung, Bandung, Indonesia.

[2]Prof. and Chair., Dept. of Oc. Engrg., Univ. of Rhode Island, Narragansett Bay Campus, Narragansett, RI 02882.

Note. Discussion open until June 1, 1997. Separate discussions should be submitted for the individual papers in this symposium. To extend the closing date one month, a written request must be filed with the ASCE Manager of Journals. The manuscript for this paper was submitted for review and possible publication on January 10, 1994. This paper is part of the *Journal of Hydraulic Engineering*, Vol. 123, No. 1, January, 1997. ISSN 0733-9429/97/0001-0002–0012/$4.00 + $.50 per page. Paper No. 7655.

ity; D_h = horizontal eddy diffusivity; Θ = temperature °C; S = salinity (ppt); and q = concentration of a conservative substance such as Θ or S.

The equations described previously assume the following: the flow is incompressible, density differences are neglected unless multiplied by gravity (Boussinesq approximation), the vertical acceleration is very small compared to gravity (hydrostatic assumption), and the horizontal stresses are neglected.

Boundary Conditions

The land boundaries are assumed impermeable where the normal component of velocity is set to zero

$$\vec{V}\cdot\vec{n} = 0 \tag{7}$$

On river boundaries, the velocities are specified and the pressure gradient is set to zero. At open boundaries the water elevation or vertically varying velocity as a function of time is known from field observations or otherwise specified.

At closed boundaries the transport of substance is zero. At an open boundary the concentration must be specified during inflow. On outflow the substance is advected out of the model domain according to

$$\frac{\partial q}{\partial t} + \frac{u}{r\cos\theta}\frac{\partial q}{\partial \phi} = 0 \tag{8a}$$

$$\frac{\partial q}{\partial t} + \frac{v}{r}\frac{\partial q}{\partial \theta} = 0 \tag{8b}$$

At the surface, the wind stress is specified as

$$\tau_{s\phi} = \rho_a C_a W_\phi \sqrt{W_\phi^2 + W_\theta^2}, \quad \tau_{s\theta} = \rho_a C_a W_\theta \sqrt{W_\phi^2 + W_\theta^2} \tag{9}$$

where W_ϕ and W_θ = wind speeds in the ϕ and θ directions, respectively; ρ_a = density of air; and C_a = drag coefficient at the surface.

The kinematic free surface boundary condition is given as

$$w = \frac{\partial \zeta}{\partial t} + \frac{u}{r\cos\theta}\frac{\partial \zeta}{\partial \phi} + \frac{v}{r}\frac{\partial \zeta}{\partial \theta} \tag{10}$$

Two options are available to specify the bottom boundary condition

1. Bottom stress condition

$$\tau_{b\phi} = \rho_o C_b u_b \sqrt{u_b^2 + v_b^2}, \quad \tau_{b\theta} = \rho_o C_b v_b \sqrt{u_b^2 + v_b^2} \tag{11}$$

   where C_b = bottom drag coefficient; and u_b and v_b = velocity components at the bottom in the ϕ and θ directions, respectively.
2. No-slip condition

$$u_b = 0 \quad \text{and} \quad v_b = 0 \tag{12}$$

At the bottom boundary, no momentum flux is allowed and the kinematic condition is specified

$$w = -u_b\frac{1}{r\cos\theta}\frac{\partial h}{\partial \phi} - v_b\frac{1}{r}\frac{\partial h}{\partial \theta} \tag{13}$$

The governing equations are transformed to a σ-coordinate system to resolve bathymetric variations with a constant number of grids. The transformation is defined as

$$\phi = \phi', \quad \theta = \theta', \quad r = R + \zeta + (\sigma - 1)(\zeta + h)/2, \quad t = t' \tag{14}$$

The governing equations now become (dropping the primes for convenience)

Continuity

$$\frac{\partial \zeta}{\partial t} + \frac{1}{r\cos\theta}\frac{\partial uD}{\partial \phi} + \frac{1}{r}\frac{\partial vD}{\partial \theta} - \frac{vD}{r}\tan\theta + \frac{\partial \omega D}{\partial \sigma} = 0 \tag{15}$$

Momentum

ϕ-direction

$$\frac{\partial uD}{\partial t} + \frac{1}{r\cos\theta}\frac{\partial uuD}{\partial \phi} + \frac{1}{r}\frac{\partial uvD}{\partial \theta} - \frac{2uvD}{r}\tan\theta + \frac{\partial u\omega D}{\partial \sigma} - fvD$$
$$= -\frac{gD}{2\rho_o r\cos\theta}\left\{[\lambda + (\rho_s - 2\rho)(1-\sigma)]\frac{\partial D}{\partial \phi} + (4\rho - 2\rho_s)\frac{\partial \zeta}{\partial \phi} + D\frac{\partial \lambda}{\partial \phi}\right\} + \frac{4}{D}\frac{\partial}{\partial \sigma}\left(A_v\frac{\partial u}{\partial \sigma}\right) \tag{16}$$

θ-direction

$$\frac{\partial vD}{\partial t} + \frac{1}{r\cos\theta}\frac{\partial uvD}{\partial \phi} + \frac{1}{r}\frac{\partial vvD}{\partial \theta} - \frac{uu - vv}{r}D\tan\theta + \frac{\partial v\omega D}{\partial \sigma} + fuD$$
$$= -\frac{gD}{2\rho_o r}\left\{[\lambda + (\rho_s - 2\rho)(1-\sigma)]\frac{\partial D}{\partial \theta} + (4\rho - 2\rho_s)\frac{\partial \zeta}{\partial \theta} + D\frac{\partial \lambda}{\partial \theta}\right\} + \frac{4}{D}\frac{\partial}{\partial \sigma}\left(A_v\frac{\partial v}{\partial \sigma}\right) \tag{17}$$

σ-direction

$$\frac{2}{D}\frac{\partial p}{\partial \sigma} = -\rho g \tag{18}$$

Conservation of Substance

$$\frac{\partial q}{\partial t} + \frac{u}{r\cos\theta}\frac{\partial q}{\partial \phi} + \frac{v}{r}\frac{\partial q}{\partial \theta} + \omega\frac{\partial q}{\partial \sigma} = \frac{4}{D^2}\frac{\partial}{\partial \sigma}\left[D_v\left(\frac{\partial q}{\partial \sigma}\right)\right] + \frac{D_h}{r^2}\left(\frac{\partial^2 q}{\cos^2\theta\,\partial \phi^2} + \frac{\partial^2 q}{\partial \theta^2}\right) \tag{19}$$

where

$$\lambda = \int_\sigma^1 \rho\, d\sigma \tag{20a}$$

$$\omega = -\frac{1}{D}(1+\sigma)\frac{\partial \zeta}{\partial t} + \gamma_\phi u + \gamma_\theta v + \frac{2}{D}w \tag{20b}$$

$$\gamma_\phi = \frac{1}{D}\left[\frac{1-\sigma}{r\cos\theta}\frac{\partial h}{\partial \phi} - \frac{1+\sigma}{r\cos\theta}\frac{\partial \zeta}{\partial \phi}\right] \tag{20c}$$

$$\gamma_\theta = \frac{1}{D}\left[\frac{1-\sigma}{r\cos\theta}\frac{\partial h}{\partial \theta} - \frac{1+\sigma}{r\cos\theta}\frac{\partial \zeta}{\partial \theta}\right] \tag{20d}$$

where $D = h + \zeta$ = total water depth.

The horizontal velocities and independent variables are next transformed to a curvilinear coordinate system. The equations of motion and continuity equation in a curvilinear coordinate system (ξ, η), in terms of the contravariant velocity components, are as follows:

Continuity

$$Jr\cos\theta\frac{\partial \zeta}{\partial t} + \frac{\partial}{\partial \xi}(\cos\theta Ju^c D) + \frac{\partial}{\partial \eta}(\cos\theta Jv^c D) + Jr\cos\theta\frac{\partial(\omega D)}{\partial \sigma} = 0 \tag{21}$$

Momentum Equation

ξ-direction

$$\frac{\partial u^c D}{\partial t} = -\frac{\theta_\eta\theta_\eta + \cos^2\theta\phi_\eta\phi_\eta}{J^2\rho_o r\cos^2\theta}\frac{Dg}{2}\left\{[\lambda + (\rho_s - 2\rho)(1-\sigma)]\frac{\partial D}{\partial \xi} + (4\rho - 2\rho_s)\frac{\partial \zeta}{\partial \xi} + D\frac{\partial \lambda}{\partial \xi}\right\} + \frac{\theta_\xi\theta_\eta + \cos^2\theta\phi_\xi\phi_\eta}{J^2\rho_o r\cos^2\theta}\frac{Dg}{2} \cdot\left\{[\lambda + (\rho_s - 2\rho)(1-\sigma)]\frac{\partial D}{\partial \eta} + (4\rho - 2\rho_s)\frac{\partial \zeta}{\partial \eta} + D\frac{\partial \lambda}{\partial \eta}\right\} - \frac{\theta_\eta}{J^2 r\cos^2\theta}\left[\frac{\partial}{\partial \xi}(\phi_\xi\cos^2\theta J u^c u^c D + \phi_\eta\cos^2\theta J u^c v^c D) + \frac{\partial}{\partial \eta}(\phi_\xi\cos^2\theta J u^c v^c D + \phi_\eta\cos^2\theta J v^c v^c D)\right] + \frac{\phi_\eta}{J^2 r\cos^2\theta}\left[\frac{\partial}{\partial \xi}(\theta_\xi\cos^2\theta J u^c u^c D + \theta_\eta\cos^2\theta J u^c v^c D) + \frac{\partial}{\partial \eta}(\theta_\xi\cos^2\theta J u^c v^c D + \theta_\eta\cos^2\theta J v^c v^c D)\right] - \frac{\partial}{\partial \sigma}(\omega u^c D) + \frac{fD}{J\cos\theta}[(\theta_\xi\theta_\eta + \cos^2\theta\phi_\xi\phi_\eta)u^c + (\theta_\eta\theta_\eta + \cos^2\theta\phi_\eta\phi_\eta)v^c] + \frac{4}{D}\frac{\partial}{\partial \sigma}\left(A_v\frac{\partial u^c}{\partial \sigma}\right) \tag{22}$$

η-direction

$$\frac{\partial v^c D}{\partial t} = \frac{\theta_\eta\theta_\xi + \cos^2\theta\phi_\eta\phi_\xi}{J^2\rho_o r\cos^2\theta}\frac{Dg}{2}\left\{[\lambda + (\rho_s - 2\rho)(1-\sigma)]\frac{\partial D}{\partial \xi} + (4\rho - 2\rho_s)\frac{\partial \zeta}{\partial \xi} + D\frac{\partial \lambda}{\partial \xi}\right\} - \frac{\theta_\xi\theta_\xi + \cos^2\theta\phi_\xi\phi_\xi}{J^2\rho_o r\cos^2\theta}\frac{Dg}{2} \cdot\left\{[\lambda + (\rho_s - 2\rho)(1-\sigma)]\frac{\partial D}{\partial \eta} + (4\rho - 2\rho_s)\frac{\partial \zeta}{\partial \eta} + D\frac{\partial \lambda}{\partial \eta}\right\} + \frac{\theta_\xi}{J^2 r\cos^2\theta}\left[\frac{\partial}{\partial \xi}(\phi_\xi\cos^2\theta J u^c u^c D + \phi_\eta\cos^2\theta J u^c v^c D) + \frac{\partial}{\partial \eta}(\phi_\xi\cos^2\theta J u^c v^c D + \phi_\eta\cos^2\theta J v^c v^c D)\right] - \frac{\phi_\xi}{J^2 r\cos^2\theta}\left[\frac{\partial}{\partial \xi}(\theta_\xi\cos^2\theta J u^c u^c D + \theta_\eta\cos^2\theta J u^c v^c D) + \frac{\partial}{\partial \eta}(\theta_\xi\cos^2\theta J u^c v^c D + \theta_\eta\cos^2\theta J v^c v^c D)\right] - \frac{\partial}{\partial \sigma}(\omega v^c D) - \frac{fD}{J\cos\theta}[(\theta_\xi\theta_\xi + \cos^2\theta\phi_\xi\phi_\xi)u^c + (\theta_\xi\theta_\eta + \cos^2\theta\phi_\xi\phi_\eta)v^c] + \frac{4}{D}\frac{\partial}{\partial \sigma}\left(A_v\frac{\partial v^c}{\partial \sigma}\right) \tag{23}$$

Conservation of Substance

$$\frac{\partial q}{\partial t} + \frac{u^c}{r}\frac{\partial q}{\partial \xi} + \frac{v^c}{r}\frac{\partial q}{\partial \eta} + \omega\frac{\partial q}{\partial \sigma} = \frac{4}{D^2}\frac{\partial}{\partial \sigma}\left(D_v\frac{\partial q}{\partial \sigma}\right) + \frac{D_h}{r^2J^2} \cdot\left[\left(\frac{\theta_\eta\theta_\eta}{\cos^2\theta} + \phi_\eta\phi_\eta\right)\frac{\partial^2 q}{\partial \xi^2} - 2\left(\frac{\theta_\xi\theta_\eta}{\cos^2\theta} + \phi_\xi\phi_\eta\right)\frac{\partial^2 q}{\partial \xi\partial \eta} + \left(\frac{\theta_\xi\theta_\xi}{\cos^2\theta} + \phi_\xi\phi_\xi\right)\frac{\partial^2 q}{\partial \eta^2}\right] \tag{24}$$

where u^c and v^c = contravariant velocities in the (ξ, η) directions, respectively; ζ = water elevation; $D = \zeta + \text{depth}$; and the Jacobian, $J = \phi_\xi\theta_\eta - \phi_\eta\theta_\xi$. The relationship between the contravariant velocities (u^c, v^c) and velocities in spherical coordinates (u, v) is given by

$$u = \cos\theta\phi_\xi u^c + \cos\theta\phi_\eta v^c \tag{25a}$$

$$v = \theta_\xi u^c + \theta_\eta v^c \tag{25b}$$

TURBULENCE PARAMETERIZATION

The turbulence parameterization is a key model component for predicting flow and mixing processes in stratified fluids. There is, however, no universally accepted procedure to represent turbulence (ASCE 1988; Cheng and Smith 1990). In this study, we employ a one equation turbulent kinetic energy model to calculate the vertical eddy viscosity and diffusivity. The length scale is specified using the approach suggested by Blackadar (1962) that has been successfully used in modeling turbulence for tidal problems (Davies and Jones 1990). The effect of stratification is accounted for by using an empirical relationship similar to the ones employed for the mixing length approach. This model accounts for the convection, diffusion, and time history of turbulent kinetic energy in unsteady flows.

Turbulent Energy

The turbulence kinetic energy equation in spherical and σ-coordinates is given as follows:

$$\frac{\partial b}{\partial t} + \frac{u}{r\cos\theta}\frac{\partial b}{\partial \phi} + \frac{v}{r}\frac{\partial b}{\partial \theta} + \omega\frac{\partial b}{\partial \sigma} = \frac{4}{D^2}\frac{\partial}{\partial \sigma}\left(\frac{A_v}{\sigma_b}\frac{\partial b}{\partial \sigma}\right) + A_v\left[\left(\frac{2}{D}\frac{\partial u}{\partial \sigma}\right)^2 + \left(\frac{2}{D}\frac{\partial v}{\partial \sigma}\right)^2\right] + \beta g\frac{2A_v}{D\sigma_t}\frac{\partial \Phi}{\partial \sigma} - \varepsilon \tag{26}$$

where b = kinetic energy.

After transformation to curvilinear coordinates (ξ, η), the preceding equation can be written as

$$\frac{\partial b}{\partial t} + \frac{u^c}{r}\frac{\partial b}{\partial \xi} + \frac{v^c}{r}\frac{\partial b}{\partial \eta} + \omega\frac{\partial b}{\partial \sigma} = \frac{4}{D^2}\frac{\partial}{\partial \sigma}\left(\frac{A_v}{\sigma_b}\frac{\partial b}{\partial \sigma}\right) + A_v\left[\left(\frac{2}{D}\frac{\partial u}{\partial \sigma}\right)^2 + \left(\frac{2}{D}\frac{\partial v}{\partial \sigma}\right)^2\right] + \beta g\frac{2A_v}{D\sigma_t}\frac{\partial \Phi}{\partial \sigma} - \varepsilon \tag{27}$$

where β = volumetric expansion coefficient; σ_b = empirical diffusion constant; σ_t = Schmidt number; Φ = mean scalar quantity; and ε = dissipation. In this study the interchange between turbulent kinetic energy and potential energy or production/dissipation by buoyant forces is neglected. It is assumed that the turbulent kinetic energy is advected and diffused in a homogeneous fluid while the effect of stratification is accounted for by an empirical formula using a Richardson number (damping function). As argued by Abraham (1988), the reproduction of internal mixing at tidal slack is beyond the capability of present turbulence models and, hence, they should not be used where this aspect is important.

Eddy Viscosity and Diffusivity Relationships

Based on dimensional reasoning the eddy viscosity is related to the kinetic energy b and mixing length L_m by

$$A_v = C_\mu L_m\sqrt{b} \tag{28}$$

where C_μ = empirical constant.

In homogeneous water, the vertical eddy viscosity and diffusivity are considered to be equal, $A_v = D_v$. In the presence of a stable vertical density gradient, both A_v and D_v are lower than their homogeneous values. The magnitude of A_v is always greater than the corresponding value of D_v.

The general form for the eddy viscosity and diffusivity are given as

$$A_v = f(R_i)C_\mu L_m\sqrt{b} \tag{29a}$$

$$D_v = g(R_i)C_\mu L_m\sqrt{b} \tag{29b}$$

Several semiempirical relations for $f(R_i)$ and $g(R_i)$ have been proposed by Munk and Anderson (1948) and Officer (1976).

Munk and Anderson (1948)

$$f(R_i) = (1 + 10.0R_i)^{-1/2} \tag{30a}$$

$$g(R_i) = (1 + 3.33R_i)^{-3/2} \tag{30b}$$

Officer (1976)

$$f(R_i) = (1 + R_i)^{-1} \tag{31a}$$

$$g(R_i) = (1 + R_i)^{-2} \tag{31b}$$

where the Richardson number, R_i, is defined by

$$R_i = -\frac{2g}{\rho D}\frac{\dfrac{\partial \rho}{\partial \sigma}}{\left[\dfrac{\partial(u)}{\partial \sigma}\right]^2 + \left[\dfrac{\partial(v)}{\partial \sigma}\right]^2} \tag{32}$$

Dissipation

From dimensional analysis the expression for dissipation, in terms of the turbulent kinetic energy and mixing length, is given by

$$\varepsilon = C_d(b^{3/2}/L_m) \tag{33}$$

where C_d = empirical constant.

Mixing Length

The mixing length formulation proposed by Blackadar (1962) is

$$L_m = \frac{KD[1 + (\sigma - 1)/2]}{1 + \dfrac{KD[1 + (\sigma - 1)/2]}{L_o}} \tag{34}$$

where K = Von Karman's constant; D = total water depth and in which the mixing length, L_m, increases from the sea bottom to the surface and the value of L_o is determined by the vertical distribution of the turbulent energy as follows:

$$L_o = \gamma D\frac{\displaystyle\int_{-1}^{1} b^{1/2}[1 + (\sigma - 1)/2]\, d\sigma}{\displaystyle\int_{-1}^{1} b^{1/2}\, d\sigma} \tag{35}$$

The constant γ determines the vertical extent of the boundary layer and vertical eddy viscosity, and is adjusted to match field observations. The viscosity increases rapidly with increasing γ in both amplitude and vertical extent (Mofjeld and Lavelle 1983). The constant γ typically ranges from 0.05 to 0.3. The coefficients in (28), (34), and (35) have values C_μ = 0.463; C_d = 0.1; σ_b = 1.37; and K = 0.4 (Davies and Jones 1990).

Boundary Conditions

The boundary condition at the surface is specified as

$$\frac{2\alpha_b A_v}{D}\frac{\partial b}{\partial \sigma} = \alpha_w U_{*_s}^3 \tag{36}$$

where U_{*_s} = friction velocity due to the wind stress and α_b, α_w are coefficients. A similar boundary condition is used by Davies and Jones (1988) in which α_b = 0.73, and α_w = 2.6. In the absence of wind forcing the flux of turbulence at the surface disappears.

For a no-slip bottom boundary condition, the turbulent kinetic energy flux into the sea bed is zero (Davies and Jones 1988) and, therefore

$$\frac{\partial b}{\partial \sigma} = 0 \tag{37}$$

For the bottom stress boundary condition, the bottom boundary layer is not resolved in detail. The turbulent kinetic energy, b, at the first grid point near the wall (where the turbulence is assumed in equilibrium and the velocity follows the log-law) is given as follows:

$$b = U_{*_b}^2/\sqrt{C_\mu C_d} \tag{38}$$

where U_{*_b} = friction velocity associated with the bottom stress. While this boundary condition is not always rigorously satisfied under unsteady conditions (Celik and Rodi 1985), it is used as a first-order approximation.

SOLUTION TECHNIQUE

The basic approach is to transform the dependent, as well as independent, variables in spherical coordinates to a curvilinear coordinate system. The equation of motion is split into exterior and interior modes to increase the allowable time step and, hence, reduce the computational time.

The velocity is decomposed into

$$u^c = U^c + u^{c\prime} \tag{39a}$$

$$v^c = V^c + v^{c\prime} \tag{39b}$$

where (U^c, V^c) and $(u^{c\prime}, v^{c\prime})$ = vertically averaged velocities and deviation velocity (from the vertically averaged velocity) in (ξ, η) directions, respectively. Solution of the exterior mode using a semiimplicit (space staggered grid) solution, methodology, and presentations of the approach used to generate the boundary conforming grid are presented by Muin and Spaulding (1996). The focus here is on three-dimensional (3D) aspects, including the deviation velocity and the turbulence equation.

Subtracting the vertically averaged momentum equations from the 3D momentum equations gives the vertical deviation velocity equations of motion

$$\frac{\partial u^{c\prime}D}{\partial t} = \frac{4}{D}\frac{\partial}{\partial \sigma}\left(A_v\frac{\partial u^{c\prime}}{\partial \sigma}\right) + A \tag{40a}$$

$$\frac{\partial v^{c\prime}D}{\partial t} = \frac{4}{D}\frac{\partial}{\partial \sigma}\left(A_v\frac{\partial v^{c\prime}}{\partial \sigma}\right) + B \tag{40b}$$

where A and B = nonbarotropic terms in the equations of motion. These terms are solved explicitly. The diffusion term in (40) is solved implicitly using a three-level scheme to damp out spurious oscillations (Fletcher 1988). The algorithm is second-order accurate both in time and space. A tridiagonal set of equations in the unknown velocity deviation is solved using a Thomas algorithm. Both the exterior and interior modes are solved at the same time step.

The finite difference procedure used to solve the turbulent kinetic energy equations has been described by Davies and Jones (1990). In the present study, a three-level time discretization (Fletcher 1988) is used instead of the Crank-Nicholson method of Davies and Jones (1990). A nonstaggered grid is used in the vertical. The C form of Davies and Jones' (1990) numerical scheme is employed to calculate the dissipation term

in the energy equation to ease the time step restriction. No iteration or filtering is employed. The time step is restricted by the horizontal advection term. As will be shown in model testing, a CFL equal to 100 can be used to predict the vertical structure of tidally induced flows.

The transport model (24) is solved by a simple explicit technique, except for the vertical diffusion that is solved by an implicit scheme to ease the time step restriction due to the small vertical length scale. In the present model, two options are available to solve the advection term. The first option is a Lax-Wendroff scheme, which is consistent with a second-order truncation error (Fletcher 1988). The second option is an upwind-differencing scheme (first-order accurate) that introduces artificial diffusivity. The horizontal diffusion term is solved by a centered-in-space, explicit technique. The diffusive and advective stability criteria in these numerical techniques are $\Delta t < \Delta s^2/(2D_h)$, and $\Delta t < \Delta s/U_s$, where Δs and U_s = horizontal grid size and velocity, respectively. To avoid spatial oscillations, the Lax-Wendroff scheme requires $D_h > U_s\Delta s/2$. This gives approximately the same amount of artificial viscosity as inherent in the upwind scheme.

MODEL TESTING

Model formulation and implementation, in computer code, were compared to analytical solutions in which the nonlinear convective acceleration and Coriolis terms were removed and the governing equations solved on a spherical coordinate system, which because of the limited domain approximated a Cartesian grid. Additional test simulations were performed to confirm the operation of the turbulent closure equations to predict the vertical structure of tidal flow and compared to a previous numerical study by Davies and Jones (1990). The model was tested in an application to salinity intrusion in a simple rectangular channel representative of the Rotterdam Waterway.

Residual Flow

The ability of the model to predict residual flow was tested for a basin with vertically constant density and viscosity. The surface boundary was forced by a constant wind stress if wind forcing was used. The test was performed in a simple, rectangular, and constant depth channel open at one end (west). The model was run for two bottom boundary conditions: (1) no-slip condition; and (2) bottom stress condition.

Following Officer's (1976) approach and neglecting advection, the horizontal diffusion of momentum, and the cross channel terms (equations laterally averaged), the steady-state expression for the vertical velocity profiles with linearized bottom friction can be given as follows

$$u = -g\Lambda\left(\frac{z^3}{6\rho A_v} + \frac{h^2}{2\rho k} + \frac{h^3}{6\rho A_v}\right) - g\iota\left(\frac{h}{k} + \frac{h^2}{2A_v} - \frac{z^2}{2A_v}\right) + \frac{\tau_s}{\rho}\left(\frac{1}{k} + \frac{h}{A_v} + \frac{z}{A_v}\right) \tag{41}$$

where

$$g\iota = \frac{\left[-g\Lambda\left(\frac{h^3}{2\rho k} + \frac{h^4}{8\rho A_v}\right) + \frac{\tau_s}{\rho}\left(\frac{h}{k} + \frac{h^2}{2A_v}\right) - hu_o\right]}{\left(\frac{h^2}{k} + \frac{h^3}{3A_v}\right)} \tag{42}$$

where Λ = horizontal density gradient; g = gravity; ι = water elevation slope; τ_s = wind stress; u_o = river flow per width; and k = linearized bottom friction. A similar equation for a no-slip condition at the bottom is given on page 120 of Officer (1976).

Three separate simulations with different forcings were studied: (1) density gradient flow; (2) wind driven flow; and (3) density gradient, wind, and river-induced flow. In these simulations, the following conditions were assumed: the density increases linearly from the head (closed end) to the mouth (open end) $\Lambda = -0.00036$ kg/m^4; wind stress $\tau_s = 0.01$ N/m^2 (1 dyne/cm^2); river flow $u_o = -0.1$ m/s; depth $h = 10$ m; vertical viscosity $A_v = 10$ cm^2/s; and linearized bottom friction $k = 0.05$ cm/s. Depending on the case the appropriate forcing parameters were used. Testing was performed using five, 10, and 20 vertical levels. The model was started with zero velocities and elevation. The density gradient was applied gradually until a steady state was achieved.

Density Gradient Forcing

Fig. 1(a) shows a comparison of the model prediction to analytic solution for the bottom stress formulation under density gradient forcing. Model predictions approach the analytic solution as the grid resolution is increased. The model overpredicts the currents near the bottom and surface at low grid resolution. The maximum errors are about 7% for five levels, 2% for 10 levels, and less than 1% for 20 levels. The model was also run with a no-slip bottom boundary condition, as shown in Fig. 1(b). When the surface boundary condition was specified using a second-order accurate representation, the model never reached steady state even with 80 levels. This problem may be caused by an underestimate of the bottom friction, which is only first-order accurate. The model, however, reached steady state when the surface boundary was reduced to first order. For this approximation the model overpredicted the velocity near the surface by 20% [Fig. 1(b)] independent of the number of the vertical levels.

Wind Forcing

Comparison of model predictions with the analytic solution under constant wind forcing with a bottom stress condition is

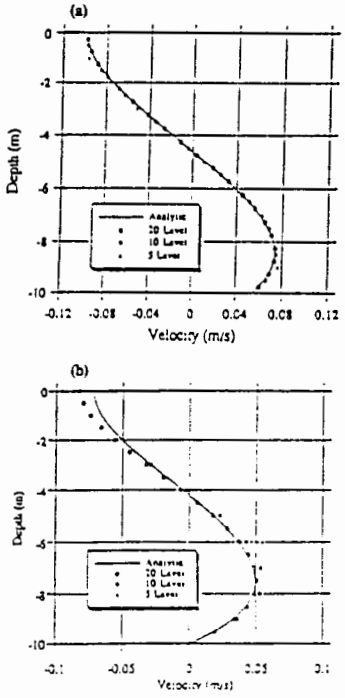

FIG. 1. Comparison of Model Predicted Vertical Structure of Velocity with Analytic Solution for Density-Induced Forcing (A_v = 10 cm^2/s, $\Lambda = -0.00036$ kg/m^4, $k = 0.05$ cm/s) for: (a) Bottom Stress; and (b) No-Slip Bottom Boundary Condition (Model Results Are Presented for 5, 10, and 20 Vertical Levels)

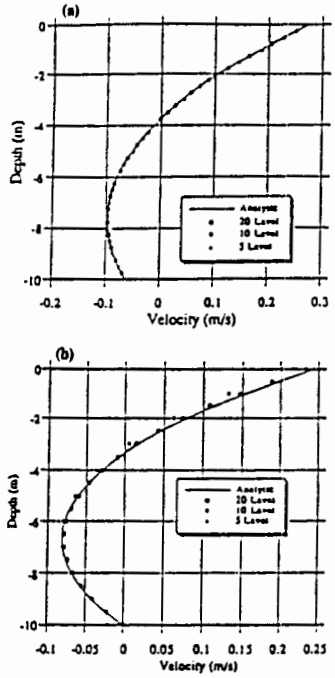

FIG. 2. Comparison of Model Predicted Vertical Structure of Velocity with Analytic Solution for Wind Driven Flow (A_v = 10 cm²/s, τ_s = 0.1 N/m² (1 dyne/cm²), k = 0.05 cm/s) for: (a) Bottom Stress; and (b) No-Slip Bottom Boundary Condition (Model Results Are Presented for 5, 10, and 20 Vertical Levels)

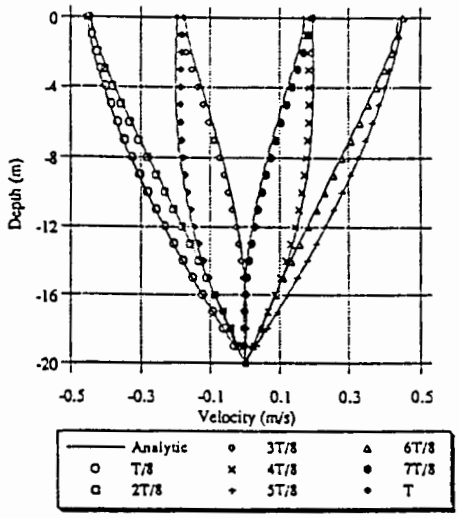

FIG. 3. Comparison of Model Predicted Velocity Structure with Analytic Solution for Tidally Driven Flow (Imposed Pressure Gradient of 0.058 N/m³) with Constant Vertical Viscosity, A_v = 0.011 m²/s at 1/8 Time Intervals Through One Tidal Cycle (Time Step, Δt = 279.45 s)

shown in Fig. 2(a). It can be seen that as the resolution increases the model predictions approach the analytic solution, especially near the bottom. The model represents the vertical velocity structure more accurately than for the density induced flow problem. The maximum errors are about 2% for five levels, 0.6% for 10 levels, and 0.2% for 20 levels. A similar problem, as in the density-induced flow, was found for the no-slip condition at the bottom and the boundary condition at the surface was modified to first order. The results are shown in Fig. 2(b). Again model prediction for this case is more accurate than in the baroclinic forcing problem.

Density Gradient Wind and River Forcing

The last test case considered flow driven by a combination of density gradient, wind, and river flow. The model was run using 20 levels. The results, not shown here, were simulated for bottom stress and no-slip bottom specifications, respectively. The agreement is excellent (<0.5%) for the bottom stress bottom boundary condition. The model underpredicts the velocity by about 5% in the mid-depth region for the no-slip bottom boundary condition.

Tidal Driven Flow

Two tests were employed to check the model's ability to simulate the vertical structure of tidal flow. The first test case is a point model in which the bottom boundary is specified using a no-slip condition, and the water slope is assumed known. The model was tested against constant and linearly varying vertical eddy viscosities. In the second test a bottom stress condition was employed at the sea bed. The bottom friction was linearized and related to the vertically averaged velocity.

Point Model Test

Constant Viscosity

The analytic solution for this problem was given in article 347 in Lamb (1945). The following data are used in model testing. The imposed pressure gradient was 0.058 N/m³; period T = 12.42 h; depth h = 20 m; vertical viscosity A_v = 0.011 m²/s; and time step Δt = 279.45 s (160 steps per cycle). The test was performed using 20 levels. The model was started with zero velocities. The water slope was applied gradually (linear ramp over 4 cycles) until a steady state was achieved. Comparison between the analytic solution and the model prediction is shown in Fig. 3. The agreement is excellent throughout the water column.

Viscosity Varying Linearly with Height

Two simulations were studied with viscosity; one increasing and one decreasing linearly from the sea bed to the sea surface. The analytic solution is presented in Prandle (1982). Simulations were performed using the same depth, grid size, period, time step, sea surface slope, and initial condition as the constant viscosity test case.

In the case of viscosity increasing linearly from the bottom (sea surface), the viscosity at the sea bed (surface) is set at A_v = 0.001 m²/s; and the viscosity at the sea surface (bed) A_v = 0.021 m²/s. The results of these simulations are in excellent agreement with the analytic solutions. The boundary layer in the linearly increasing case is (referenced from the sea bed) thinner than the constant viscosity case due to the lower viscosity near the bottom. The boundary layer for the linearly decreasing case is thicker than for the constant viscosity case and occupies the whole water column due to the fact that the vertical viscosity at the bottom is higher than in the two previous cases.

3D Testing

Lynch and Officer (1985) derived an analytic solution for the 3D flow driven by periodic forcing, with linearized bottom stress (ku_b, kv_b) and linked to the vertically averaged solution for an annular channel. The solutions were assembled from one-dimensional (1D) vertical diffusion and 2D vertically averaged solutions of the governing equations.

Consider the quarter-circle geometry with quadratically varying bathymetry $h = h_o r^2$. Note r refers to the radius of the annual channel. The sketch of geometry, bathymetry, and grid configuration are shown in Fig. 4. The viscosity is constant throughout the depth. The analytic solution, however, requires that $A_v/(\Omega h^2)$ and kh/A_v be constant, and hence A_v and k must

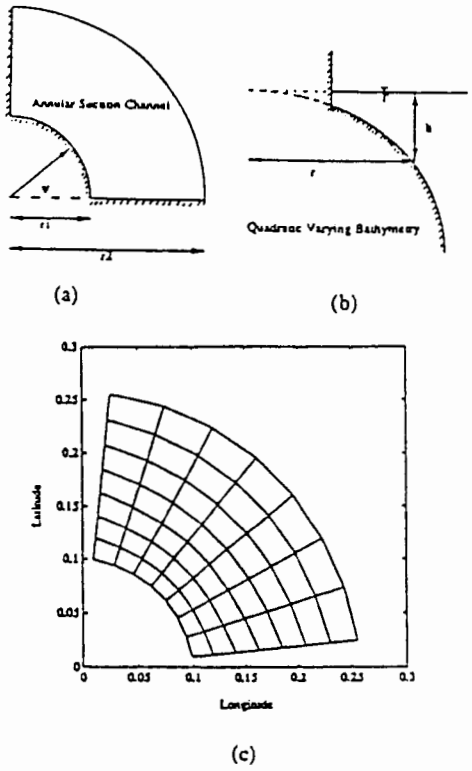

FIG. 4. Three-Dimensional Tidally Driven Model Test for: (a) Geometry; (b) Bathymetry; and (c) Grid Configuration [r_1 = 9,950 m; r_2 = 31,250 m; $h = 5\,(r/r_1)^2$]

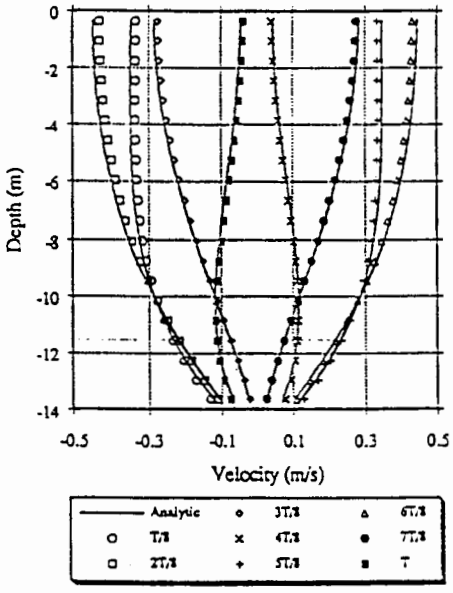

FIG. 5. Vertical Structure of Velocity at Increments of 1/8 of M_2 Tidal Period at r = 16,660 m and Ψ = 39.4° for Three-Dimensional Model Test in Annular Section Channel, r_1 = 9,950 m; r_2 = 31,250 m; $A_v/(\Omega h^2) = 0.1$; $kh/A_v = 10$; Δt = 558.9 s

vary horizontally. Model tests were performed using a coarse, slightly nonorthogonal 7 × 7 grid system. The following parameters were used: inner radius r_1 = 9,950 m; outer radius r_2 = 31,250 m; $\Omega = 1.4 \times 10^{-4}$ s^{-1}; $kh/A_v = 10$; $A_v/(\Omega h^2) = 0.1$; and $h_o = 5/r_1^2$ m^{-1}. The open boundary was specified by varying the tidal amplitude $\zeta_o = 0.1 \cos(2\psi)$ m, where ψ = rotation angle. The model was run using eight and 20 levels in the vertical and time steps of 279.45, 558.9, and 1117.8 s.

Comparison of the model and analytical solution at point (5, 5) or at radius 16,660 m and ψ = 39.375° for 20 levels with a time step of 558.9 s at one-eighth period increment is shown in Fig. 5. The agreement is very good. The largest errors (<10%) are near the surface area.

Sensitivity of the model predicted near surface currents (at $T/8$, $T/4$, $3T/8$, $T/2$) to grid resolution and time step in the near surface region is shown in Table 1. The maximum errors occur at slack tide (at $T/2$). The model predicted errors decrease with decreasing time step. Model errors using eight vertical levels are approximately the same as those using 20 vertical levels.

A vector plot of the velocity field at the surface at $T/4$ (not presented) shows that the agreement between model predictions and analytic solution is excellent, even though the grid was relatively coarse and slightly nonorthogonal. The errors are less than 5%, except at the corner point of the inner radius $r = r_1$. Here they are about 10% due to the fact that the velocity is very small at this location. The errors become much smaller (<0.6%) at the outer radius near the open boundary. Comparison of the model-predicted velocity time series at a radius of 16,660 m, ψ = 39.375°, and for 0.35 m and 13.65 m below the sea surface with the analytic solution are shown in Fig. 6. The bottom velocity leads the surface velocity by 0.85 h. Predictions are again in excellent agreement with the analytic solution.

Turbulence Model Simulations

A simulation was performed in an open-closed, rectangular channel driven with tidal forcing, and a water depth of 10 m. The channel length is 51.34 km, and is represented by 20 horizontal grids. The tidal amplitude was 1.2 m, with a period of 12.42 h, γ = 0.4. A point 5.55 km from the open channel, where the pressure gradient has a magnitude that would give a current with amplitude 1.0 m/s in an inviscid calculation, was chosen to study the vertical structure of the velocity, eddy viscosity, and turbulent energy. The simulation assumed a ho-

TABLE 1. Model Prediction Errors (%) of Surface Velocity at r = 16,660 m and Ψ = 39.4° for Annular Section Channel with Quadratic Bathymetry Using 8 and 20 Vertical Levels with Time Steps of 279.45, 558.9, and 1117.8 s

	8 Level			20 Level		
t (1)	279.45 s (CFL = 0.5) (2)	558.9 s (CFL = 1.0) (3)	1117.8 s (CFL = 2.0) (4)	279.45 s (CFL = 3.1) (5)	558.9 s (CFL = 6.2) (6)	1117.8 s (CFL = 12.4) (7)
$T/8$	4.1	4.2	4.8	3.9	4.0	4.6
$T/4$	3.7	3.7	4.0	3.5	3.5	3.9
$3T/8$	3.1	3.0	3.0	3.1	3.0	3.0
$T/2$	8.7	10.0	12.6	7.6	8.8	11.6

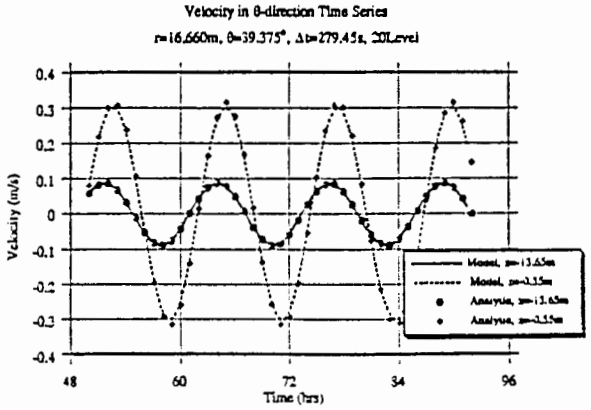

FIG. 6. Comparison of Model Predicted Velocity Time Series with Analytical Solution at r = 16,660 m and Ψ = 39.4° for Three-Dimensional Model Test in Annular Section Channel Driven by M_2 Tide at Open Boundary with Varying Amplitude of $\zeta_o = 0.1 \cos(2\psi)$ m; r_1 = 9,950 m; r_2 = 31,250 m; $A_v/(\Omega h^2) = 0.1$; $kh/A_v = 10$; Δt = 279.45 s; and 20 Vertical Levels

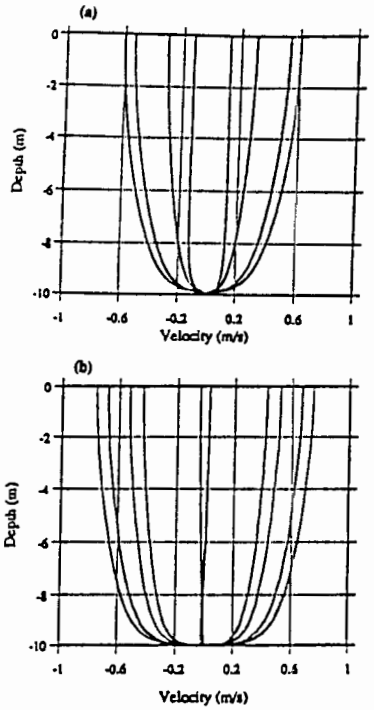

FIG. 7. Comparison of (a) Model Predicted Vertical Structure of Velocity with (b) Numerical Simulations of Davies and Jones (1990) for One-Dimensional Turbulence Model Test Driven by M_2 Tide with Imposed Pressure Gradient of 0.14 N/m^3; No-Slip Bottom Boundary Condition; $\gamma = 0.4$; $\Delta t = 558.9$ s; and 40 Vertical Levels

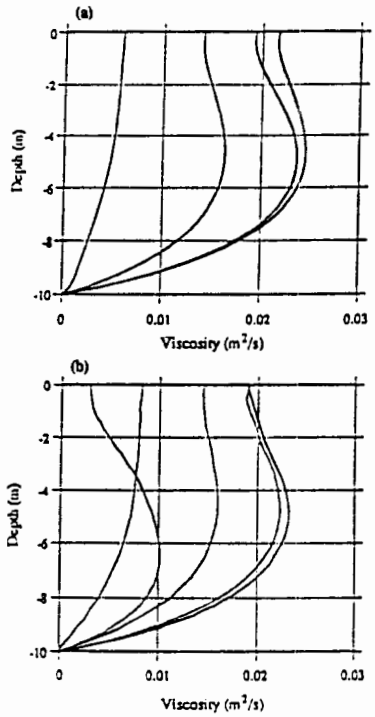

FIG. 8. Comparison of (a) Model Predicted Vertical Structure of Viscosity with (b) Numerical Simulations of Davies and Jones (1990) for One-Dimensional Turbulence Model Test Driven by M_2 Tide with Imposed Pressure Gradient of 0.14 N/m^3; No-Slip Bottom Boundary Condition; $\gamma = 0.4$; $\Delta t = 558.9$ s; and 40 Vertical Levels

mogeneous fluid. The Coriolis, baroclinic, and advective terms were neglected to compare the present results with the circulation and turbulence model developed by Davies and Jones (1990).

For a no-slip condition at the bottom boundary, simulations were conducted using 40 levels with a time step of 558.9 s. A comparison between the results of the present model (40 levels) and Davies and Jones' (1990) with 100 levels and a logarithmic transformation is shown in Figs. 7–10. Results are given at one-eighth intervals during the tidal cycle. The maximum surface velocity of the present model is about 20%

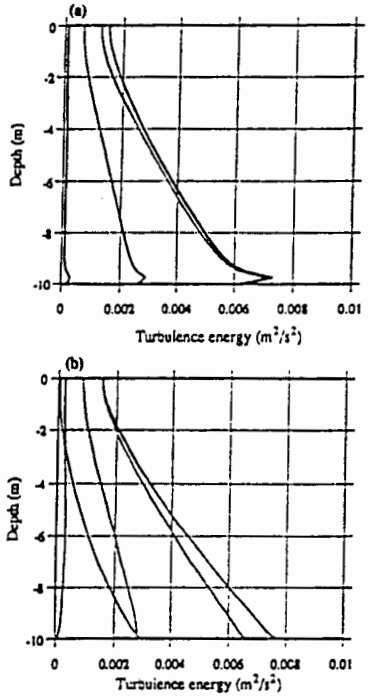

FIG. 9. Comparison of (a) Model Predicted Vertical Structure of Turbulence Energy with (b) Numerical Simulations of Davies and Jones (1990) for One-Dimensional Turbulence Model Test Driven by M_2 Tide with Imposed Pressure Gradient of 0.14 N/m^3; No-Slip Bottom Boundary Condition; $\gamma = 0.4$; $\Delta t = 558.9$ s; and 40 Vertical Levels

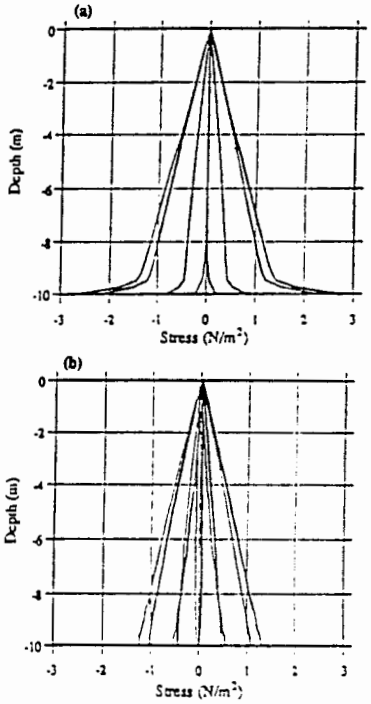

FIG. 10. Comparison of (a) Model Predicted Vertical Structure of Shear Stress with (b) Numerical Simulations of Davies and Jones (1990) for One-Dimensional Turbulence Model Test Driven by M_2 Tide with Imposed Pressure Gradient of 0.14 N/m^3; No-Slip Bottom Boundary Condition; $\gamma = 0.4$; $\Delta t = 558.9$ s; and 40 Vertical Levels

lower than their results. The structure of the eddy viscosity, turbulent energy, and shear stress are similar. However, the bottom shear stresses are twice as high in Davies and Jones (1990) than in the present simulation because the present grid structure does not provide sufficient resolution in the near-bed region. This problem is more severe at low grid resolution.

For the bottom stress specification, simulations were performed using 10 and 40 levels with a time step of 279.45 s. In these simulations the bottom drag coefficient was set at 0.0025, and $\gamma = 0.4$. A comparison between simulations using high (40 levels) and low vertical resolution (10 level) is shown in Fig. 11 for the velocity profile. The maximum viscosity, shear stress, and energy (not shown) computed using the low resolution grid are approximately 25% higher than simulations using the high resolution grid. The velocity structure (Fig. 11), however, is not significantly affected. Further tests showed that a stable and accurate velocity prediction can be obtained using

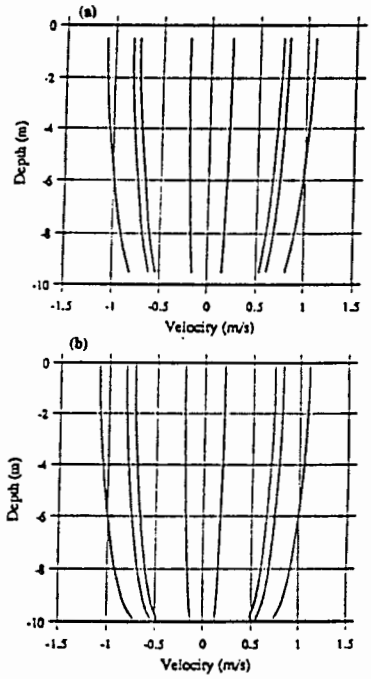

FIG. 11. Comparison of Model Predicted Vertical Structure of Velocity Using (a) 10 and (b) 40 Vertical Levels at Location 5.55 km from Open Boundary for Turbulence Model Test Driven by M_2 Tide; Bottom Stress Condition; $\gamma = 0.4$; $C_b = 0.0025$; $\Delta t = 558.9$ s

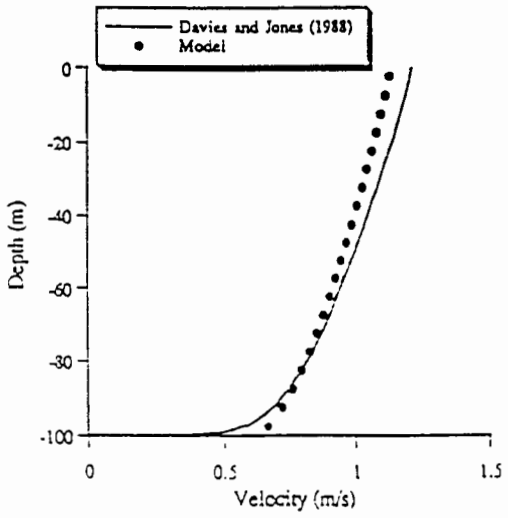

FIG. 12. Comparison of Model (Bottom Stress Condition) Predicted Vertical Structure of Velocity with Numerical Simulations of Davies and Jones (1988) Driven by Wind Stress; $\tau_s = 1.0$ N/m^2; $C_b = 0.0025$; and $\gamma = 0.2$

a time step of 1117.8 s (550 CFL, based on the diffusive time scale for 40 levels).

The model was also tested against steady wind-induced flow with a depth of 100 m, a wind stress of 1 N/m^2, a bottom stress specification; 20 levels, with a friction coefficient of, $C_b = 0.0025$, and $\gamma = 0.2$. A comparison of the velocity computed using the present model and similar results by Davies and Jones (1988) with 100 levels and a logarithmic transformation is presented in Fig. 12. The agreement is very good. A maximum difference of 5% is predicted near the surface and the sea bed. The model-predicted vertical structure of viscosity gives excellent agreement at middepth and near the surface, but slightly overpredicts at the bottom. The turbulent energy simulated by the present model is higher than Davies and Jones' (1988) model both at the surface and bottom. Differences that occur near the bottom are due to differences in the bottom boundary condition specification. The present simulations employ a bottom stress condition where the turbulent energy at the sea bed is specified while Davies and Jones (1988) use a no-slip bottom condition and specify no energy flux at the sea bed. In general the agreement is excellent although the present work uses relatively low grid resolution compared to Davies and Jones (1988).

Salinity Intrusion Simulations

Ippen and Harleman (1961) derived an analytical solution for salinity intrusion under the assumption that the salinity distribution can be represented by the equilibrium of the 1D convective-diffusion processes where the time and cross-sectionally averaged fresh water (seaward) flux of salt is balanced by the horizontal diffusive flux of salt (landward). The effect of gravitational convection by density differences (density included) is neglected. Consider a rectangular channel with a length of 105.5 km, a river flow velocity of 0.000714 m/s, and horizontal diffusion coefficients of 4, 6, 8, and 10 m^2/s. The advective term in the salt transport equation is solved by the Lax-Wendroff method. The open boundary is specified by a constant salinity of 30 ppt. Comparison between model predictions and the analytic solution for various values of the horizontal diffusion coefficient D_h is shown in Fig. 13. The agreement between the model and analytical solution is excellent.

Finally the model was used to predict the salinity intrusion in Rotterdam Waterway using identical conditions to those employed by Smith and Takhar (1981). The simulation was intended to evaluate the ability of the model to predict salinity intrusion. The waterway was represented by a rectangular channel with a length of 99 km. The width and depth were

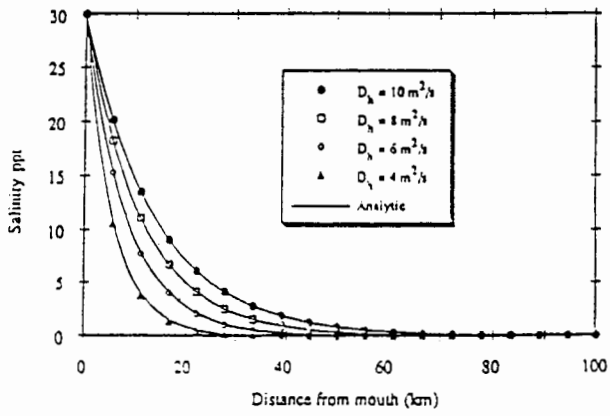

FIG. 13. Comparison of Model Predicted Salinity Distribution with Analytic Solution for One-Dimensional Salinity Intrusion Test (Transport Equation Is Solved by Lax-Wendroff Method; River Flow Velocity Is 0.000714 m/s; and Horizontal Diffusion Coefficients of 4, 6, 8, and 10 m^2/s Are Used)

kept constant with values of 400 and 13 m, respectively. The river inflow was 1,000 m^3/s. The model was run using 40 grids along the channel and 20 levels in the vertical. The initial conditions for velocity, elevation, and salinity were set to zero. Along the open boundary (mouth) the salinity distribution is assumed to vary from 30 ppt at the bottom to 20 ppt at the surface on inflow. The model was run with an M_2 tide. The time step was 558.9 s with a tidal amplitude at the open boundary of 0.9 m. The advective term in the salt transport equation was solved using the upwind method. The Lax-Wendroff method was not used because it required a large horizontal diffusivity (~5000 m^2/s) to maintain stability. The model was run for 66 d to achieve steady state.

A simulation was performed in which the vertical viscosity and diffusivity were calculated by the turbulence model. The bottom friction, C_b, was 0.0010. It was found that the model was very sensitive to the value of γ in the mixing length specification. Since the turbulent energy source is from the bottom boundary, the bottom drag coefficient, C_b, is also important in determining the vertical velocity structure. Fig. 14 shows the salinity distribution along the channel for $C_b = 0.0005$ and $\gamma = 0.03$ with the empirical formulation of (30), which was taken from Officer (1976), implemented to represent stratification effects. Smith and Takhar's (1981) model predictions and field observations are also shown [Fig. 14(a)]. The results show that the model-predicted high tide salinity distribution is in reasonable agreement with and an improvement over Smith and Takhar's results. Both the present and Smith and Takhar (1981) models do not accurately predict the low tide salinity distribution. As analyzed by Smith and Takhar (1981), the poor model performance for the low water salinity distribution is caused by the dock system in the waterway acting as a source and sink of salt on the ebb and flood tide, respectively.

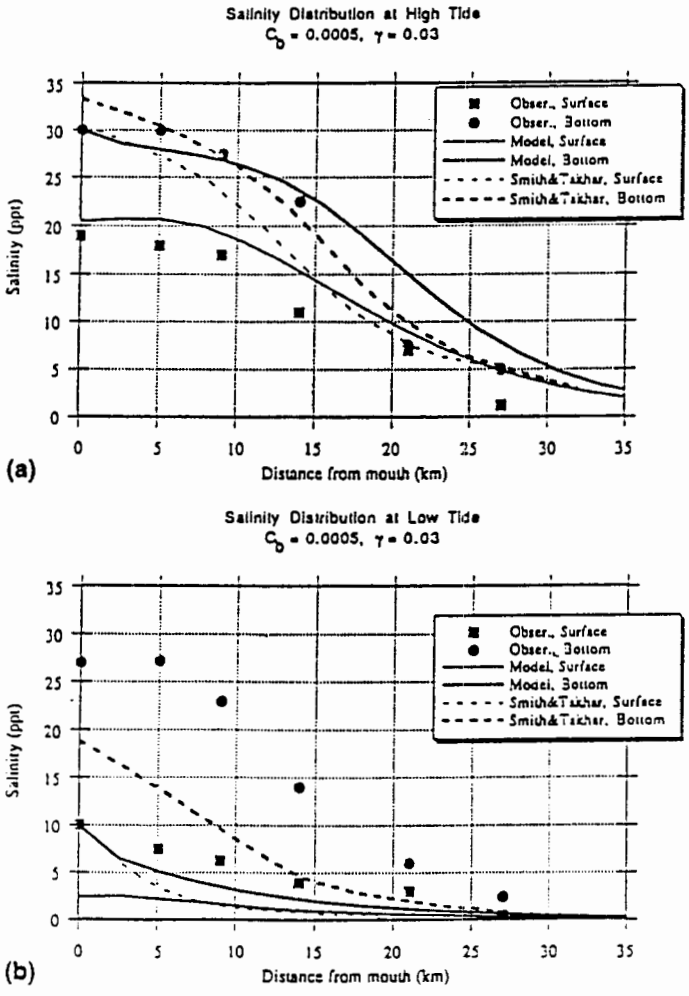

FIG. 14. Comparison of Model Predicted Salinity Distribution along Channel with Observations and Numerical Simulation of Smith and Takhar (1981) for Rotterdam Waterway at: (a) High Tide; and (b) Low Tide (Vertical Viscosity and Diffusivity Are Obtained from Turbulence Model Using Bottom Friction; C_b = 0.0005; and γ = 0.3)

CONCLUSION

A detailed description of the 3D boundary-fitted circulation model in spherical coordinates for coastal waters is presented. Both the dependent and independent horizontal variables are transformed to a boundary-fitted coordinate system. The equations are also transformed to σ-coordinates to resolve the variation in bathymetry. Both the exterior and interior mode are solved using the same time step. The numerical scheme is second order in time and space. The time step is not restricted by the shallow water gravity wave and vertical diffusion CFL criteria. The eddy viscosity/diffusivity can be specified or obtained from a one equation turbulence energy model.

A series of model tests to linear problems shows that the present model is fully capable of predicting the vertical structure of the flow in response to tidal, wind, river, and density forcing. The 3D model test in an annular section channel with quadratic bathymetry under tidal forcing has shown the model's ability to resolve a more complicated geometry and bathymetry.

The model, with a bottom stress condition, gives good predictions of the vertical structure of the velocity, shear stress, turbulence energy, and eddy viscosity even at modest vertical grid resolutions. No iteration or filtering is employed. The no-slip bottom boundary condition version of the present model fails to accurately predict the shear stress and energy distributions at the sea bed for 40 vertical levels because of the lack of vertical resolution near the sea bed.

Agreement between the model and analytic solution is excellent for the 1D salinity intrusion problem where the density gradient induced flow is neglected. The model accurately predicted the salinity distribution at high tide in the Rotterdam Waterway where the viscosity/diffusivity were obtained from a turbulence model. The poor results at low tide were probably caused by the lack of consideration of the effect of the dock system on the salinity field (Smith and Takhar 1981).

The CPU time of the internal mode with turbulence model for each water cell per computational step is 3.1×10^{-6} min on a 486/50 MHz personal computer system using a Lahey F7732 Version 5.1 Fortran compiler. The CPU time of the external mode is 2.9×10^{-6} min using the same machine and compiler.

APPENDIX I. REFERENCES

Abraham, G. (1988). "Turbulence and mixing in stratified tidal flows." *Physical processes in estuaries*, P. Dronkers and R. Leussen, eds., Springer-Verlag KG, Berlin, Germany.

ASCE Task Committee on Turbulence Models in Hydraulic Computations. (1988). "Turbulence modeling of surface water flow and transport: Part I." *J. Hydr. Engrg.*, ASCE, 114(9), 970–991.

Blackadar, A. K. (1962). "The vertical distribution of wind and turbulent exchange in a neutral atmosphere." *J. Geophys. Res.*, 67, 3095–3120.

Celik, I., and Rodi, W. (1985). "Calculation of wave-induced turbulent flows in estuaries." *Oc. Engrg.*, 12(6), 531–542.

Cheng, R. T., and Smith, P. E. (1990). "A survey of three-dimensional numerical estuarine models." *Estuarine and coastal modeling*, M. L. Spaulding, ed., ASCE, New York, N.Y., 1–15.

Davies, A. M., and Jones, J. E. (1988). "Modelling turbulence in shallow sea regions." *Small-scale turbulence and mixing in the ocean, Proc., 19 Liege Colloquium on Oc. Hydrodyn.*, J. C. Nihoul and B. M. Jamart, eds., Univ. of Liege, Liege, Belgium.

Davies, A. M., and Jones, J. E. (1990). "On the numerical solution of the turbulence energy equations for wave and tidal flows." *Int. J. for Numer. Meth. in Fluids*, 11, 1–25.

Fletcher, C. A. J. (1988). *Computational techniques for fluid dynamics, volume I, fundamental and general techniques*. Springer-Verlag New York, Inc., New York, N.Y.
Ippen, A. T., and Harleman, D. R. F. (1961). "One-dimensional analysis of salinity intrusion in estuaries." *Tech. Bull. No. 5*, Com. on Tidal Hydr., U.S. Army Corps of Engrs., Fort Belvoir, Va.
Johnson, B. H. (1980). "VAHM-A vertically averaged hydrodynamic model using boundary-fitted coordinates." *MP HL-80-3*, U.S. Army Corps of Engrs. Wtrwy. Experiment Station, Vicksburg, Miss.
Lamb, H. (1945). *Hydrodynamics*. Dover Publications, Inc., New York, N.Y.
Lynch, D. R., and Gray, W. G. (1978). "Analytic solutions for computer flow model testing." *J. Hydr. Div.*, ASCE, 104(00), 1409–1428.
Lynch, D. R., and Officer, C. B. (1985). "Analytic solutions for three-dimensional hydrodynamic model testing." *Int. J. for Numer. Meth. in Fluids*, 5, 529–543.
Lynch, D. R., and Werner, F. E. (1987). "Three-dimensional hydrodynamics on finite-element. Part I: Linearized harmonic model." *Int. J. for Numer. Meth. in Fluids*, 7, 871–909.
Mofjeld, H. O., and Lavelle, J. W. (1984). "Setting the length scale in a second-order closure model of the unstratified bottom boundary layer." *J. Phys. Oceanography*, 14, 833–839.
Muin, M. (1993). "A three-dimensional boundary-fitted circulation model in spherical coordinates," PhD dissertation, Univ. of Rhode Island, Narragansett Bay Campus, Narragansett, R.I.
Muin, M., and Spaulding, M. L. (1996). "Two-dimensional boundary-fitted circulation model in spherical coordinates." *J. Hydr. Engrg.*, ASCE, 122(9), 512–521.
Munk, W. H., and Anderson, E. R. (1948). "Notes on theory of thermocline." *J. Marine Res.*, 7, 276.
Officer, C. B. (1976). *Physical oceanography of estuaries*. John Wiley & Sons, Inc., New York, N.Y., 120.
Prandle, D. (1982). "The vertical structure of tidal currents." *Geophys. Astrophys. Fluid Dyn.*, 22, 29–49.
Sheng, Y. P. (1986). "A three-dimensional mathematical model of coastal, estuarine and lake currents using boundary-fitted grid." *Tech. Rep. No. 585*, Aeronautical Research Associates of Princeton, Princeton, N.J.
Smith, T. J., and Takhar, H. S. (1981). "A mathematical model for partially mixed estuaries using the turbulence energy equation." *Estuarine, Coast., and Shelf Sci.*, 13, 27–45.
Spaulding, M. L. (1984). "A vertically averaged circulation model using boundary-fitted coordinates." *J. Phys. Oceanography*, 14, 973–982.
Swanson, J. C. (1986). "A three-dimensional numerical model system of coastal circulation and water quality," PhD dissertation, Univ. of Rhode Island, Kingston, R.I.

APPENDIX II. NOTATION

The following symbols are used in this paper:

A_v = vertical eddy viscosity;
a = tidal wave amplitude;
b = turbulence kinetic energy;
C_μ = empirical constant in eddy viscosity relationship;
C_a = drag coefficient at surface;
C_b = drag coefficient at bottom;
C_d = empirical constant in energy dissipation relationship;
D = elevation + water depth;
D_h = horizontal eddy diffusivity;
D_v = vertical eddy diffusivity;
g = gravitation;
h = water depth;
J = Jacobian of curvilinear coordinate;
K = Von Karman constant;
k = linearized bottom friction;
L = wave length;
L_m = mixing length;
l = length of channel;
n = node number;
p = pressure;
q = concentration of substance;
R = radius of earth;
R_i = Richardson number;
S = salinity;
T = wave period;
t = time;
u_o = river flow;
U_{*_s} = friction velocity due to wind stress;
U_{*_b} = friction velocity due to bottom stress;
U, V = vertically averaged velocity in ϕ and θ direction;
U^c, V^c = vertically averaged velocity in curvilinear coordinate;
u, v, w = water velocity in ϕ, θ, r direction;
u^c, v^c = water velocity in curvilinear coordinate;
u_b = bottom velocity in ϕ direction;
v_b = bottom velocity in θ direction;
W_ϕ = wind speed in ϕ direction;
W_θ = wind speed in θ direction;
β = volumetric expansion coefficient;
γ = constant parameter in mixing length formulation;
ε = dissipation rate of energy;
ζ = water elevation;
ζ_o = water elevation amplitude at open boundary;
Θ = temperature °C;
ι = water surface slope;
κ = wave number;
Λ = horizontal density gradient;
ξ, η = generalized curvilinear coordinate system;
ρ = water density;
ρ_a = air density;
ρ_o = water density average;
$\bar{\rho}$ = vertically averaged of water density;
ρ' = vertically density difference;
σ = vertical coordinate transformation;
σ_b = empirical diffusion constant;
σ_t = Schmidt number;
τ_b = bottom shear stress;
τ_s = wind shear stress;
Φ = mean scalar quantity;
ϕ, θ, r = spherical coordinate system;
Ω = wave frequency; and
ω = vertical velocity in σ transform coordinate.